A theoretical analysis of Bose-Einstein condensate based beamsplitters, interferometers, and transistors

by

James A. Stickney

A Thesis

Submitted to the Faculty

of the

WORCESTER POLYTECHNIC INSTITUTE

In partial fulfillment of the requirements for the

Degree of Doctor of Philosophy

in

Physics

by

September 2007

APPROVED:

Professor Alex A. Zozulya, Major Thesis Advisor

Professor Padmanabhan K. Aravind, Comittee Member

Professor Courtney Lannert, Comittee Member

Abstract

Over the last several years considerable efforts have been made to develop Bose-Einstein condensate (BEC) based devices for a number of applications including fundamental research, precision measurements, and navgation systems. These devices, capable of complex functionality, can be built from simpler components which is currently done in both optics and microelectronics. These components include cold atom equivalents of beamsplitters, mirrors, waveguides, diodes, and transistors. The operation of the individual components must be fully understood before they can be assembled into a more complex device. The primary goal of this dissertation is to present a theoretical analysis of these components. It begins with a theoretical analysis of several different types of cold-atom beamsplitters in the context of BEC interferometry. Next, the dynamics of an interferometer that uses optical pulses to control the dynamics of the BEC will be presented. Finally, a proposal for a BEC based component that has behavior that is similar to an electronic transistor is introduced.

Contents

List of Figures

Chapter 1

Introduction

Since the first observation of Bose-Einstein condensation in dilute alkali gases [1, 2], there has been a great deal of interest in using a Bose-Einstein condensate (BEC) for precision measurements. This is because BEC based sensors (especially BEC interferometers) are extremely sensitive to many different phenomena including accelerations, rotations, electromagnetic fields, and gravitational fields. Once developed, BEC based sensors will be among the most accurate devices yet built [3, 4]. This dissertation presents a theoretical analysis of BEC beamsplitters, interferometers, and a BEC based transistor. The remainder of this chapter is a brief history of atom interferometry, history of Bose-Einstein condensation, an introduction to the methods used to make a BEC, and the current state of BEC based devices.

1.1 History of interferometry

Interference of light, first observed in 1801 by Thomas Young with his famous double-slit experiment, showed conclusively that light behaves as a wave. This discovery was as important to the physics of the nineteenth century as the quantum theory was to physics in the twentieth century. It revolutionized optics and provided the crucial clue that led to the discovery that light is an electromagnetic wave. It was soon realized that the interference of light could be used to make precision measurements. Due to the extraordinary efforts of experimentalists such as Fizeau, Michelson, Morley, Rayleigh, Mach, Zehnder, Fabry, and Perot, optical interferometry evolved into a mature field [5]. Interferometers of the nineteenth century, that could measure path differences with precision on the order of one wavelength of light, were the most precise measuring instruments of the period.

Optical interferometers can be divided into four basic types. They are Michelson interferometers, Mach-Zehnder interferometers, Sagnac interferometers, and Fabry-

Perot interferometers. All of these interferometers are very similar, and operate using the same physical principles. Only the Mach-Zehnder interferometer will be discussed in this section. A schematic of a Mach-Zehnder interferometer is shown in Fig 1.1. In this type of interferometer, a beam of light strikes a beamsplitter. Half of the light passes through the splitter and the other half is reflected off of the splitter. The two beams of light then strike mirrors that redirect them to the recombiner. The amount of light exiting each port of the recombiner depends on the optical path length difference between the two paths. For example, if the two paths are of equal length the light exits through the horizontal port and if the path length differs by half a wavelength the light exits through the vertical port.

In his 1924 doctoral dissertation, Louis de Broglie introduced the hypothesis that matter, like light, should behave as a wave. This hypothesis offers a simple explanation of the energy levels of the hydrogen atom. However, for this hypothesis to be true, matter must show interference phenomena. To test this hypothesis, physicists began to look for interference effects first using electrons and then using neutrons. It only took two years for the experimentalists G. P. Thomson, Clinton Davisson, and Lester Germer to demonstrate electron interference [6]. In the 1940s neutrons, produced in nuclear reactors, were also shown to interfere.

Because atoms are composite particles made of several electrons, protons, and neutrons, they offer several advantages over neutrons or electons in matter wave interferometry. Due to atoms larger mass, their de Broglie wavelength is much smaller than the wavelength of an electron or neutron with the same velocity. Atoms also have internal degrees of freedom that can be used to manipulate them. They interact with the environment in many different ways (ie. static and dynamic electromagnetic fields, gravity, and interatomic potentials). Atoms can be either bosons or fermions and because of their different statistics, they offer different advantages in

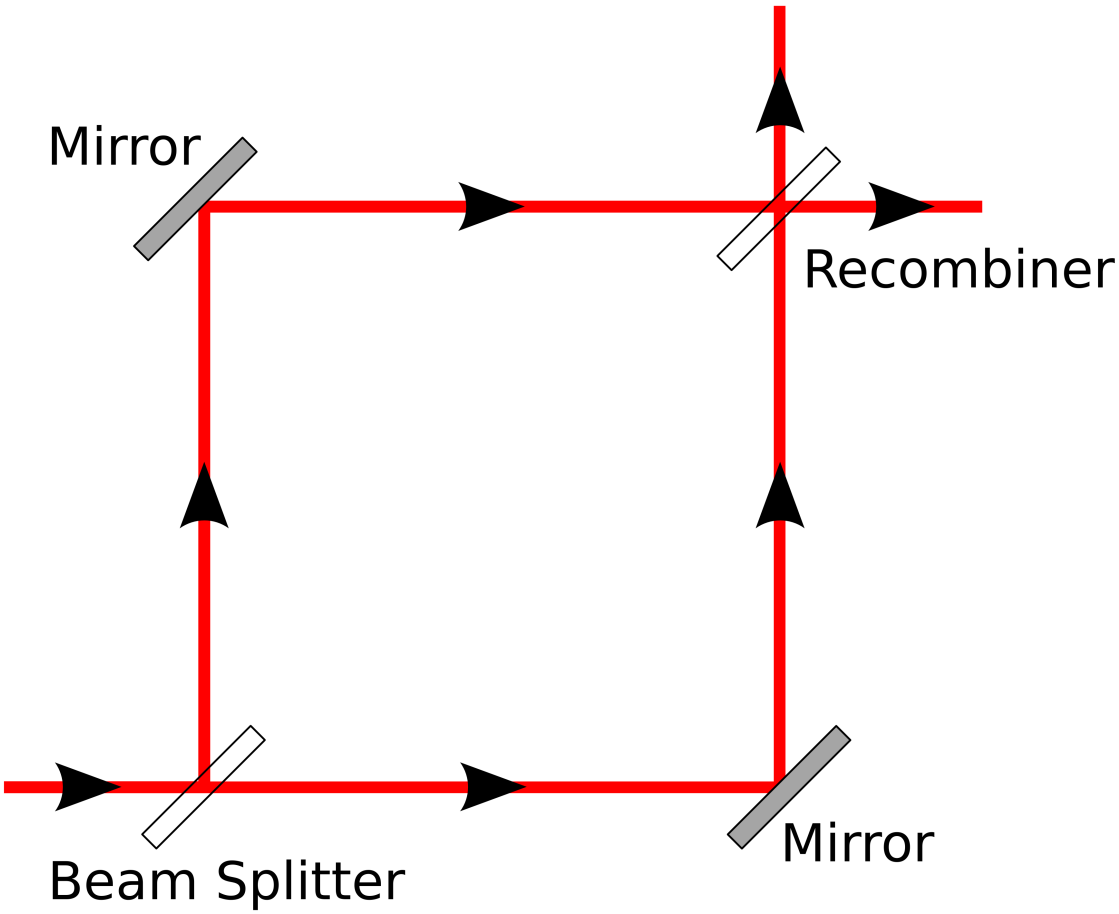

Figure 1.1: A schematic representation of an optical Mach-Zehnder interferometer.

interferometry [4].

The first atom interferometers were developed by Norman Ramsey [7]. His experiments used an atomic beam, which is a jet of atoms in a long vacuum chamber. At one end of the vacuum chamber there was an oven that heated the atoms to a high temperature, typically around 400 K. The atoms entered the vacuum chamber from the oven through a small hole. As they traveled down the vacuum chamber they passed through several different regions. In the first region, the atoms were prepared in a single hyperfine state. Then they entered a region that had an oscillatory radio-frequency (RF) electromagnetic field which coupled two hyperfine states. While in this region, the atoms experienced a $\pi/2$ pulse which placed them in an equal superposition of the two hyperfine states. This $\pi/2$ pulse was analogous to the beamsplitter in Fig. 1.1. Next they entered a region with no RF field. In this region the two hyperfine states evolved with different frequencies and, as a result, a phase difference between them accumulated. The atoms then entered another region that had an oscillating RF field and they experienced a second $\pi/2$-pulse, which was analogous to the recombiner in Fig. 1.1. After this second $\pi/2$ pulse, the population of the two hyperfine states was dependent on the phase shift that accumulated while the atoms were in the region with no RF field. Finally, a Stern-Gerlach magnet physically separated the two hyperfine states. By counting the number of atoms in each of the two states, the phase difference could be determined. Interferometers of this type have been used to precisely measure the magnetic moment of various atoms. However, since the atoms in each hyperfine state traveled along the same physical path, this type of interferometer could not measure accelerations or rotations [7].

Over the past three decades, atom interferometry using atomic beams has evolved into a mature field. During this time researchers have learned to build interferometers in which the atoms travel through different physical paths. These interferome-

ters have been used to measure rotations and accelerations [8]. In fact, it has been shown that an atom interferometer with an enclosed area can measure rotations with 10^{10} more sensitivity than a comparable optical interferometer [3, 4].

Two different methods were developed to make a beam interferometer with a physical separation between the two arms of the interferometer.

The first method used periodic potentials as diffraction gratings. These periodic potentials were created with either microfabricated transmission gratings [9] or with two counter-propagating laser beams [5]. This method used three identical gratings, in which the first grating acted as a beamsplitter, the second as a mirror, and the third as a second beamsplitter. At each grating the atomic beam was diffracted into many orders and, as a result, the atomic beam was split into many different paths. Since only two of these paths were used for the interferometer, the flux of atoms through the interferometer was greatly reduced and long integration times were required to obtain a low signal to noise ratio. These types of interferometers have provided some of the most accurate measurements of the fine structure constant [10] and the electric polarizability of alkali atoms [11, 12].

The second method was developed by Mark Kasevich's group [13]. This method used stimulated Raman scattering to control the dynamics of the atoms. As is shown in Fig. 1.2 (a), stimulated Raman scattering uses two counter-propagating laser beams that couple two ground states to one excited state. The first laser beam couples the first ground state $|1\rangle$ to the excited state $|3\rangle$ while the second laser beam couples the second ground state $|2\rangle$ to the excited state $|3\rangle$. If the laser beams are both detuned from the transition as shown in Fig. 1.2 (a), an atom can be transfered from state $|1\rangle$ to state $|2\rangle$ while keeping the probability of finding an atom in state $|3\rangle$ zero. During the scattering, an atom absorbs a photon from the first laser beam, and emits one into the second laser beam. Since the photons carry momentum, the

state $|1, p\rangle$ is scattered into the state $|2, p + 2\hbar k_l\rangle$, where p is the atom's momentum parallel to the direction of the laser beams and k_l is the wavevector of the two laser beams.

A schematic of an interferometers that uses stimulated Raman scattering is shown in Fig. 1.2 (b). An atomic beam is prepared so that all of the atoms are in the state $|\psi\rangle = |1, p = 0\rangle$ using an appropriately tuned pump laser. The atoms then pass through the first set of counter propagating Raman laser beams. As atoms pass through these laser beams, they experience a $\pi/2$ pulse which places them in the equal superposition state $|\psi\rangle = (|1, 0\rangle + |2, 2\hbar k_l\rangle)/\sqrt{2}$. The atomic beam is split into two parts that separate physically as they propagate down the vacuum chamber. Once the beams propagate down the chamber for a time T, a second pair of Raman lasers applies a π pulse, which sends $|1, 0\rangle \rightarrow |2, 2\hbar k_l\rangle$ and $|2, 2\hbar k_l\rangle \rightarrow |1, 0\rangle$. After the atoms have propagated for an additional time T, the two beams overlap and are in the state $|\psi\rangle = (e^{i\Delta\varphi/2}|1, 0\rangle + e^{-i\Delta\varphi/2}|2, 2\hbar k_l\rangle)/\sqrt{2}$, where $\Delta\varphi$ is the phase difference between the two paths of the interferometer. At this time a second $\pi/2$ pulse is applied and recombines the atoms. After the recombination, the atoms are in the state $|\psi\rangle = -i \sin\frac{\Delta\phi}{2}|1, 0\rangle + \cos\frac{\Delta\varphi}{2}|2, 2\hbar k_l\rangle$ and, by measuring the number of atoms in each of the two ground states, the phase $\Delta\varphi$ can be determined. Interferometers of this type have been used to precisely measure rotations [14], the earth's gravity gradient [15], and fundamental constants such as $\hbar/m$ [16].

Atom interferometers using thermal sources have provided measurements of unpresented accuracy since the 1960's. Interferometers using BEC have the potential to provide even greater accuracy.

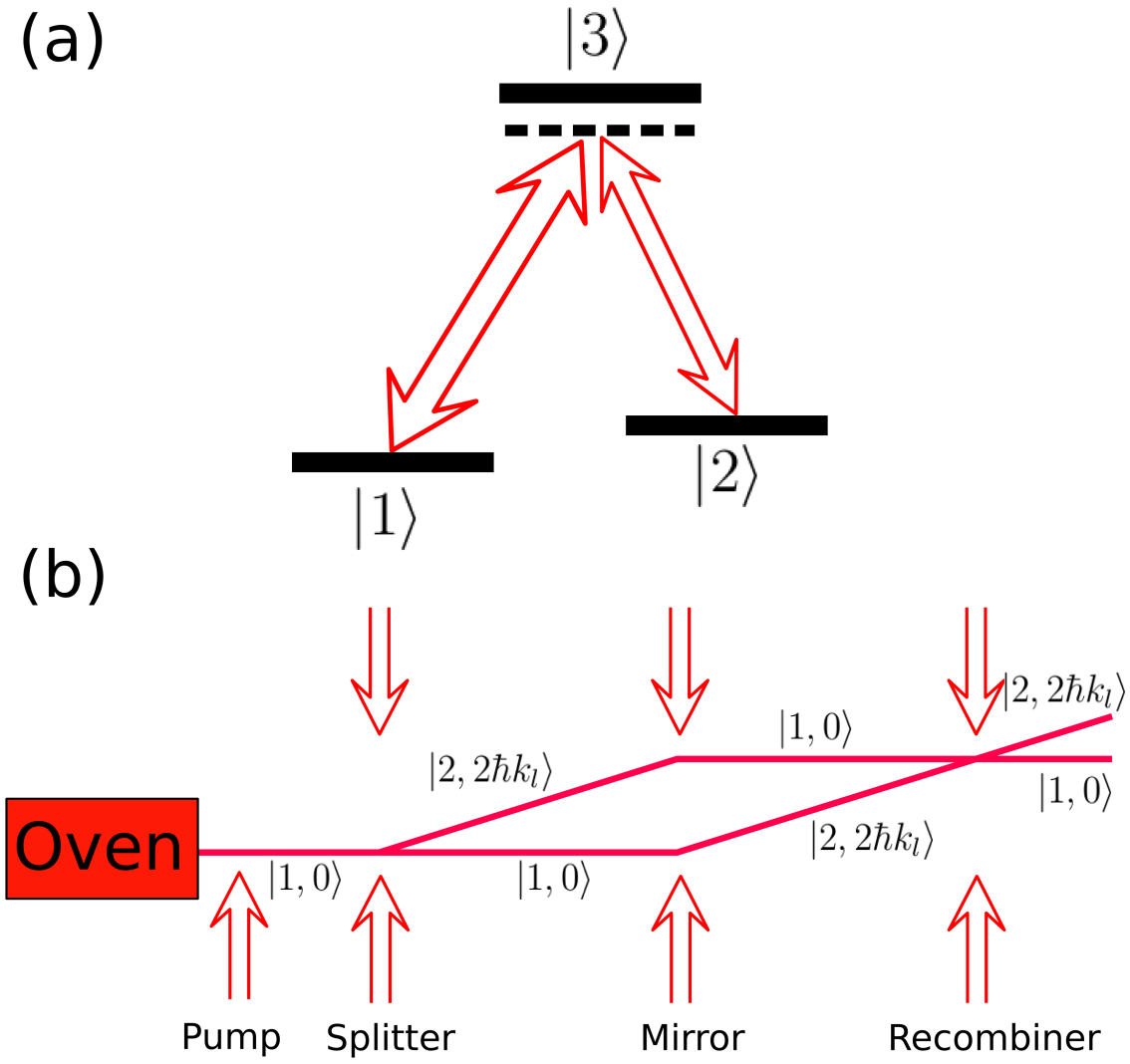

Figure 1.2: (a) The energy levels used in stimulated Raman scattering and (b) a schematic representation of a stimulated Raman scattering based atom interferometer.

1.2 History of Bose-Einstein condensation

Bose-Einstein condensation was the final and, perhaps, the most exciting result of the old quantum theory. This theory existed before the advent of Schroedinger's wave function formalism and Heisenberg's matrix method. The history of Bose-Einstein condensation began in 1859 when Gustav Kirchhoff stated that there must be a black-body radiation law that depends only on temperature and light frequency. However, there were insufficient experimental results to determine the formula for this law. Forty years later, experimental physicists finally probed the far infrared spectrum of black-body radiation.

In 1900, Max Planck was the first theorist to analyze this new data, and from this data he correctly guessed the functional form of the black-body radiation law. He spent the next few months deriving his formula from first principles. In order to get the correct form, he needed to count the number of states discretely rather than continuously. Interestingly, Max Planck felt that this "quantization" of states was merely a "trick" to make the math work.

In 1905, Albert Einstein published a paper that showed that Plank's quantization could be used to explain the photoelectric effect, which is when electrons are emitted from metal after it absorbs electromagnetic radiation. Because he showed that Plank's quantization was not merely a "trick", but could be used to explain a new phenomenon, he received the Nobel prize in 1921. Today we refer to these quantized electromagnetic states as photons.

In 1924, a young Indian physicist named Satyendra Nath Bose developed a new derivation of Planks law. His paper explaining this derivation was rejected for publication. Since this derivation used photons, he decided to send a copy of the paper to Einstein. This paper sparked Einstein's interest and he quickly translated

it into German. He submitted it for publication with the attached note, "In my opinion Bose's derivation of Planks formula constitutes an important advance [17]."

In 1925, Einstein published three papers using the new statistical methods proposed by Bose. He made a few minor modifications so that he could apply the new statistics to matter as well as light. Using these statistics he showed that below a certain temperature there was a new phase of matter, in which a macroscopic number of particles are in the lowest quantum state. This phase of matter has become known as a Bose-Einstein condensate, and was the first purely quantum mechanical phase transition to be predicted [17].

In 1928, Fritz London pointed out that superfluid helium might be a manifestation of Bose-Einstein condensation. The transition temperature that was predicted by the Bose-Einstein theory was close to the transition temperature of superfluid helium. It was assumed that interparticle interactions were the cause of the difference between the predicted and observed temperatures. It is now known that, because the interactions between the atoms in a liquid are strong, no more than about ten percent of the helium atoms in the superfluid phase occupy a single quantum state. Therefore, today, superfluid helium is not considered to be a true BEC [18].

1.3 Experimental realization of BEC

In 1995, a series of spectacular experimental developments changed the face of physics forever. In this year the first true BEC was created by Eric Cornell and Carl Wieman in Boulder, Colorado. Later that year Wolfgang Ketterle also created a BEC in Cambridge, Massachusetts. Two technical developments made this possible. The first was the advent of laser cooling and trapping in the mid 1980's. The second was the development of magnetic trapping and RF-forced evaporative

cooling. The combination of these two experimental techniques allowed physicists to cool a gas from hundreds of degrees Kelvin to a few nano Kelvin without using any conventional cryogenic techniques.

1.3.1 The magneto-optical trap

The understanding that light carries momentum, and therefore can exert a force on an object is as old as Maxwell's equations first published in 1861. However, the ability to actually trap an object with light forces alone is a recent achievement. Optical trapping did not exist until after lasers were developed. Arthur Ashkin, in the 1970's, developed the first optical traps for micron sized objects. These traps are called dipole force traps and the force is proportional to the gradient of the intensity of the laser light [19].

Dipole force traps can be used to trap micron sized particles easily because, at room temperature, the average velocity of the micron-sized particles is very small, on the order of several mm/s. On the other hand, atoms in a gas at room temperature have average velocities of several hundred km/s and cannot be held in a dipole force trap. Atoms were first trapped with a new kind of trap, called a Magneto Optical Trap (MOT). Note that, once a gas is cooled in a MOT, it can be transfered into a dipole force trap for later manipulation.

A 3-D MOT uses a combination of a laser field and a static magnetic field to trap atoms in a vacuum chamber. The magnetic field is usually produced by a pair of anti-Helmholtz coils. Anti-Helmholtz coils are a pair of Helmholtz coils with the current in one coil running in a clockwise direction and the current in the other coil running in a counter-clockwise direction. By symmetry, the magnetic field at the center of the space between the coils is zero and the magnitude of the field increases linearly away from that center. Six circularly polarized laser beams are directed at

the center point.

The basic physics of the operation of a 3-D MOT can be explained by considering a 1-D MOT that traps a 1-3 atom. A 1-3 atom has one ground state with azimuthal quantum number $m = 0$ and three excited states with azimuthal quantum numbers $m = -1, 0, +1$. The 1-D MOT uses two laser beams as shown in Fig. 1.3. The laser beam going from left to right has σ_- polarization, so that a photon in the beam that it carries angular momentum $-\hbar$ along the direction of propagation, and the laser beam going from right to left has σ_+ polarization so that a photon in the beam carries angular momentum $+\hbar$ along the direction of propagation. Both of these laser beams are red detuned from the atomic transition. In addition to the laser beams the MOT has a magnetic field which is zero in the trap center, negative to the left of the center, and positive to the right.

The laser beam with σ_- polarization couples the ground state to the $m = -1$ excited state and the laser beam with σ_+ polarization couples the ground state with the $m = +1$ excited state. Note that in this configuration, there is no coupling between the ground state and the $m = 0$ excited state.

Because the laser is detuned from the atomic transition, the probability of absorbing a photon is small when the atom is at the origin and stationary. As shown in Fig. 1.3 (a), if the atom is displaced to the left, the $m = -1$ level is Zeeman shifted to lower energy, which brings the σ_- laser beam into resonance with the atom. The atom then absorbs a photon from the σ_- beam and gives it a momentum kick to the right. Similarly if the atom is displaced to the right, it absorbs a photon from the σ_+ laser beam giving it a kick to the left. This position dependent absorption of photons acts as a restoring force for the atom and traps it near the zero in the magnetic field.

The laser field also acts like a viscous force on the atom. The mechanism for this

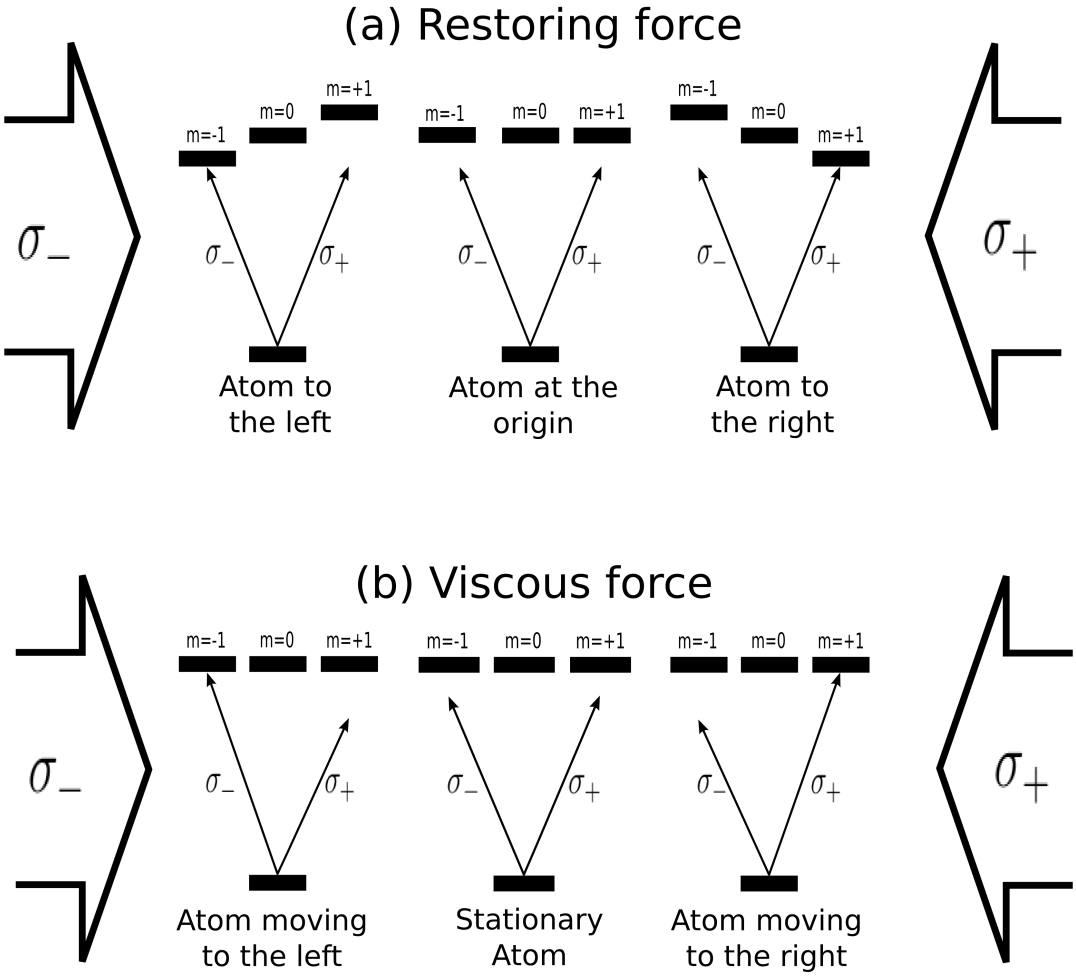

Figure 1.3: A schematic representation of the (a) trapping and (b) cooling mechanisms of a MOT.

force is shown in Fig. 1.3 (b). If the atom is moving to the left, the σ_- laser beam is Doppler shifted and appears bluer, bringing it into resonance with the atom. The atom will then absorb a photon from the σ_- beam. Similarly, if the atom is moving to the right, it absorbs photons from the σ_+ laser beam. Since the atom absorbs a photon from the laser beam that it is moving towards, its speed is reduced. The viscous force is large enough so that the atoms in a MOT are over-damped.

In experiments a dilute room temperature atomic gas is added into the vacuum chamber that contains a 3-D MOT. Some of the atoms in the gas are moving slowly enough that when they enter the MOT they are stopped by the viscous force and captured. As a result, the MOT fills with atoms.

When an atom spontaneously emits a photon it moves away from the atom in a completely random direction. As a result the atoms in a MOT receive random momentum kicks and undergo Brownian motion. The distribution of the momentum of the atoms as they undergo Brownian motion is Gaussian and it is possible to associate a temperature with the trapped atoms. For the simple case of a 1-3 atom, discussed above, it is possible to show that the minimum value of this temperature is the Doppler temperature $T_D = \hbar\Gamma/2k_B$, where Γ is the decay rate of the excited state and k_B is Boltzmann's constant.

By considering a more complex atom, it is possible to show that an atomic gas can be cooled below the Doppler limit, [20]. This is called polarization gradient cooling. The lowest possible temperature of an atom in a MOT is the the recoil temperature, which is $T_r = \hbar^2 k_l^2/mk_B$, where m is the atom's mass and k_l is the wavenumber of the lasers.

1.3.2 Magnetic trapping and evaporative cooling

A MOT is very useful for collecting atoms. However, it can only cool those atoms to the recoil temperature, which is not cold enough to make a BEC. A magnetic trap holds atoms while they are cooled to make a BEC. A magnetic trap confines a gas of atoms in a region of space using a nonhomogenious magnetic field. The atoms in this field experience potential energy $V = \mu_B g_F m B$ [21], where μ_B is the Bohr magneton, g_F is the Lande g-factor, m is the azimuthal quantum number, and B is the magnitude of the magnetic field. An example of a magnetic trap is shown in Fig. 1.4. The magnitude of the magnetic field is shown in the top of this figure as a blue curve. The potential energy of an atom, assumed to be in the $F = 2$ hyperfine state, is shown in the bottom of Fig. 1.4. The different states with azimuthal quantum numbers m are shown as different curves. For the states $m = 2$ and $m = 1$, the atoms are attracted to the region of lowest magnetic field. These atoms are trapped and referred to as low-field seeking atoms. The atoms in the $m = -1$ and $m = -2$ states are attracted to regions of highest magnetic field are ejected from the trap and are referred to as high-field seeking atoms. The $m = 0$ state is not affected by the magnetic field.

Once the atoms have been transferred from a MOT into a magnetic trap they are further cooled until they reach the BEC transition temperature. To cool the atoms, the method of RF-forced evaporate cooling was developed [1, 21]. During this evaporative cooling, the atoms with the most energy are selectively removed from the trap using an RF field cooling the atoms that remain trapped.

Once the gas is cooled below the BEC critical temperature T_c, a macroscopic number of atoms occupy the lowest quantum state. For a gas trapped in a harmonic potential with frequencies $(\omega_x, \omega_y, \omega_z)$, the critical temperature is $T_c = \hbar\bar{\omega}(N/\zeta(3))^{1/3}/k_B$, where $\bar{\omega} = (\omega_x\omega_y\omega_z)^{1/3}$ is the geometric average of the trapping frequencies, N is

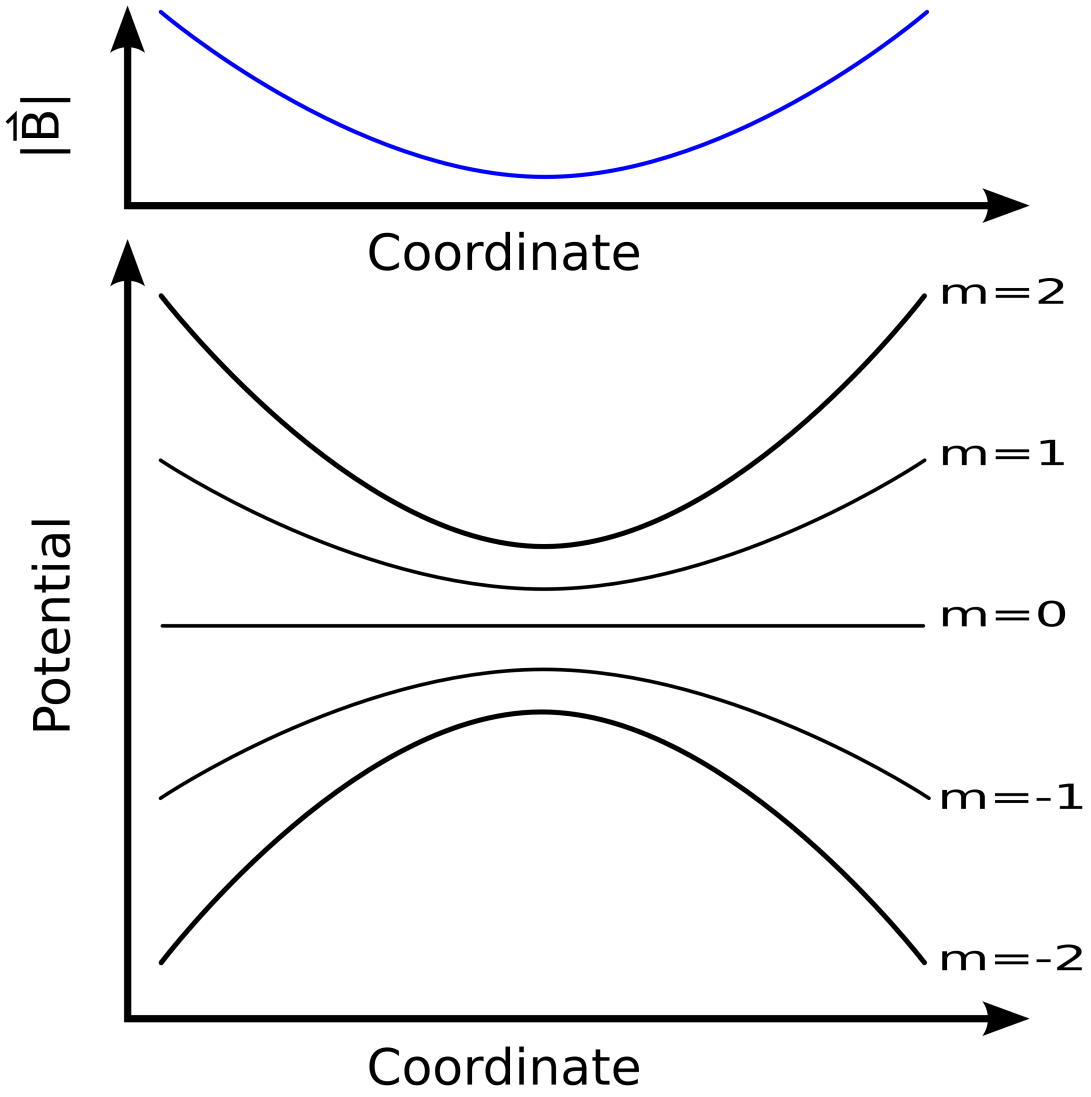

Figure 1.4: The top of this figure shows the magnitude of a trapping field as a blue curve. The potential energy of atoms in different states m as a function of coordinate is shown in the bottom of this figure.

the number of trapped atoms and $\zeta(3) \approx 1.202$ is the Riemann zeta function.

1.4 Atom Chips

The first BECs were made using machines that were relatively large and very complex. Before BECs can be used for practical applications the machines used to produce them must be both miniaturized and simplified. The most promising way to miniaturize a BEC machine to use atom chips [22]. An atom chip is a silicon wafer that has wires deposited on its surface. By passing a current through these wires a magnetic field is produced, which is used to create and manipulate the BEC. An example of an atom chip is shown if Fig. 1.5 (a).

The simplest example of a potential that can be produced with an atom chip is an atom waveguide. In a waveguide the atoms are held in two dimensions, but allowed to freely propagate in the third. An atom waveguide can be built using a single current carrying wire on a chip, plus an external uniform magnetic field. Consider a straight piece of wire. The magnetic field produced by this wire is shown in Fig. 1.5 (b) as a series of concentric blue circles. The current is running into the page and, as a result, the field points in the clockwise direction. In addition to the field produced by the wire, there is a uniform external field pointing from left to right that is shown by the red lines in Fig. 1.5 (c). The two fields will cancel each other above the wire. The magnitude of the magnetic field produced by the sum of the two fields contains a minimum that runs above the wire. This magnetic field can be used as an atom waveguide and is as shown as a countour plot in Fig. 1.5 (d).

The production and manipulation of BECs using an atom chip is appealing for many reasons. The trapping potentials created by atom chips, using the same

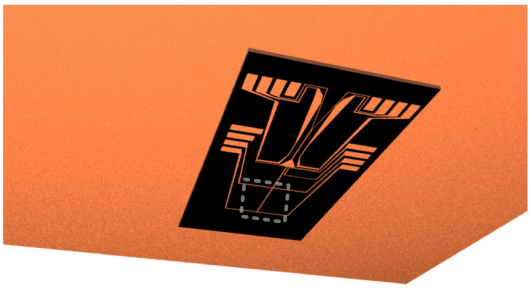

(a) An atom chip

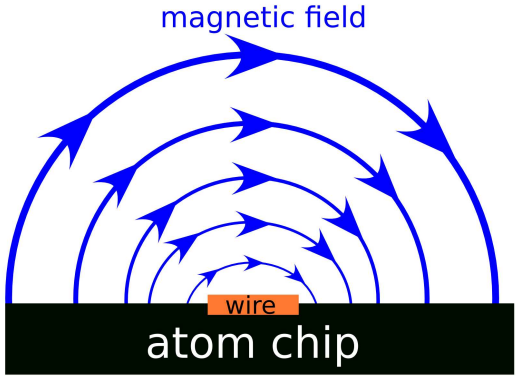

(b) The magnetic field due to a single wire

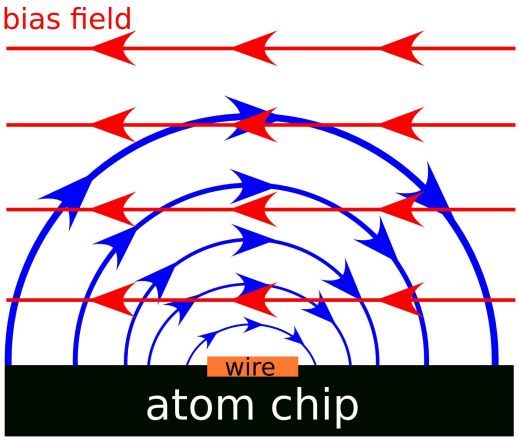

(c) The magnetic fields due to the wire and the external field

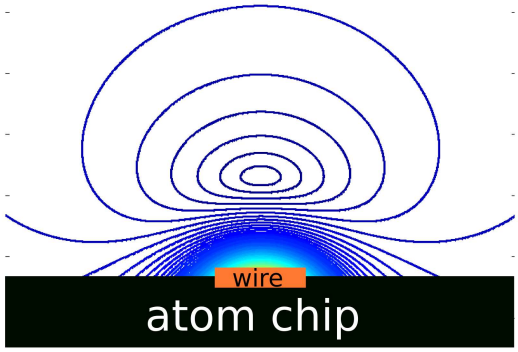

(d) The magnitude of the total magnetic field

Figure 1.5: (a) An example of an atom chip. (b) The magnetic field produced by a single wire on the atom chip. (c) The field produced by the wire (blue) and an external magnetic field (red). (d) The magnitude of the total magnetic field.

electrical current as a large scale machine, have much higher frequencies [23]. As a result, atom chips require less power. An atomic cloud confined in a trap using an atom chip can be cooled to ultra-cold temperatures more rapidly [24]. This makes the realization of a quasi-continuous source of BECs atoms more feasible. Atom chips also enable integration of several relatively simple components into devices with complex functionality [25, 26].

The magnetic fields produced by current in the wires of an atom chip can be used to create many different components. Examples of components that have been built using atom chips include beamsplitters [27], conveyor belts [28], and ring traps [29]. These relatively simple components can be integrated into larger more complex devices that are capable of much more complex functionality. The integration of many components on to a single chip is the most promising way to build practical BEC based devices.

1.5 BEC based atom interferometry

The development of a practical chip-based atom interferometer, using a BEC, would revolutionize internal navigation systems, precision measurements, and, perhaps, quantum information technology [22, 3, 4, 30]. The single most important element of any interferometer is the beamsplitter. Two alternative methods for splitting a BEC have been experimentally demonstrated [31, 32, 33, 34, 35]. The first method uses a potential that transforms from a single-well into a double-well potential. This method is discussed in Sec. 1.5.1 In the second method, the atoms are confined in a static waveguide, and the BEC is split using a standing optical wave that is produced by a pair of counter-propagating laser beams. This method is discussed in Sec. 1.5.2.

1.5.1 BEC interferometers with a double-well potential

An interferometer that uses a double-well potential has been demonstrated by several groups [36, 31]. These interferometers confine a BEC in all three dimensions and are called trapped double-well interferometers. The cycle for these interferometers is shown in Fig. 1.6 (I) and begins by loading a BEC into the lowest mode of a single well trap (Fig. 1.6 (Ia)). The trap is then transformed into a double-well so that half of the BEC is located in each well (Fig. 1.6 (Ib)). While the two wells are separated, a phase difference between the BEC in each well accumulates. If the phase difference is π the BEC wavefunction will be odd (Fig. 1.6 (Ic)). When the two wells are recombined the BEC wavefunction remains odd (Fig. 1.6 (Id)). If, on the other hand, the phase shift is 0 or 2π, the BEC wavefunction will be even (Fig. 1.6 (Ie)). When recombined the wavefunction will remain even (Fig. 1.6 (If)). By counting the number of atoms in the even or odd modes, the phase shift can be measured.

Similar interferometers, that have not yet been built, use a waveguide to confine a BEC and are called guided double-well interferomters. The primary advantage of these types of interferomters is that they can be operated continously. The cycle for a guided double-well interferometer is schematically shown in Fig. 1.6 (II). The cycle begins by launching a BEC so that while it moves down the guide it is in the lowest transverse mode [37]. As the BEC propagates down the guide, the guide splits into two parallel guides so that half of the BEC travels through one of the guides, and the other half travels through the other guide. The two guides run parallel for a distance L, after which they recombine into a single guide. While the BEC is separated, a phase difference between the two halves accumulates. The relative population of the symmetric and antisymmetric modes in the recombined BEC depends on this phase difference. By counting the number of atoms in each

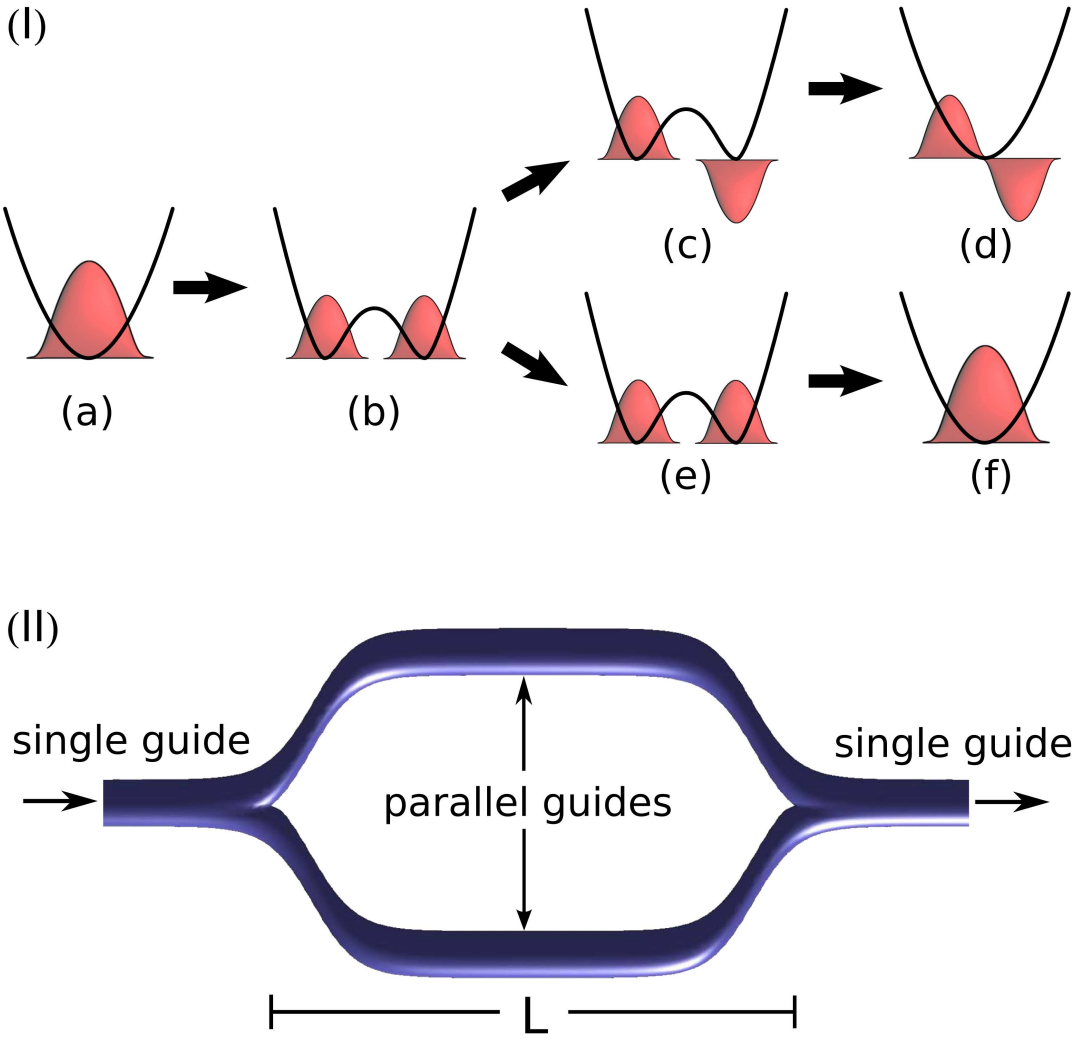

Figure 1.6: (I) A schematic of a trapped double-well interferometer. (II) A schematic of a guided double-well atom interferometer.

mode, the phase difference can be measured.

A trapped double-well interferometer was first demonstrated by the group of Wolfgang Ketterle and David Pritchard at MIT [36]. This interferometer used an optical dipole force potential to trap the BEC. The potential was created with detuned laser beams and the single-well was transformed into a double-well using an acousto-optic modulator. This interferometer achieved a separation of 13 μm between the wells and a coherence time of 5 ms. When the phase difference is close to π there is an instability during the recombination of the wells which causes exponential amplification of the initially unpopulated even mode (this instability is analyzed in Chapter 2 of this dissertation). To avoid the instability the MIT group did not recombine in the trap. Instead, they turned off the trap while the wells were separated. This caused the BEC to expand and when each half of the BEC wavefunction overlapped they interfered with each other. By imaging the interference pattern the phase shift was measured. Until recently, this was the only recombination method used with trapped double-well interferometers.

After the optical potential experiments were concluded, the group at MIT attempted to build an atom chip based trapped double-well interferometer using a two wire beamsplitter [38, 27]. This is the simplest way to create a double-well potential on an atom chip. This beamsplitter consisted of two parallel wires, each carrying the same current and an external magnetic field that was perpendicular to the wires. By varying the magnitude of the field, the potential could be transformed from a single-well to a double-well. Unfortunately, this type of a beamsplitter was difficult to build. This was because, as the potential was transformed from a single-well to a double-well, it passed through a region in which the trap became flat and small perturbations of the potential created excitations in the BEC that limited the phase coherence of the interferometer [38].

Another attempt to create a trapped double-well interferometer was made by the group of Jorg Schmiedmayer [31, 39]. This interferometer also used two parallel wires. The current in the first wire was held constant and the current in the second wire oscillated at radio-frequency. Atoms in combined static and oscillating magnetic fields were in a "dressed" state, which is a particular linear combination of the states m with the same quantum number F. This type of potential is called an adiabatic "dressed" state potential and can be changed from a single-well to a double-well by changing the amplitude and frequency of the oscillating current. The primary advantage of this trap is that for the same current in the wires it confines the atoms more than the two-wire beamsplitter. As a result, larger perturbations are required to create excitations in the BEC. The first experiments with this type of interferometer had a spacing between the wells of 80 μm and a coherence time of 2 ms [31].

Inspired by Schmiedmayer's success, the MIT group decided to build an interferometer that also used an adiabatic "dressed" state potential. This interferometer demonstrated a coherence time of 200 ms. This was 100 times longer than the previously demonstrated coherence time. The increased time was attributed to number squeezing of the BEC during the splitting process [32].

The MIT group discovered recently a new method for measuring the phase difference between the BEC in each well using a trapped double-well interferometer [40]. In this method, the BEC was recombined in the trap and held in the single-well long enough for the gas to reach thermodynamic equilibrium. The temperature of the gas was found to be dependent on the phase difference and when the temperature was measured, the phase difference was determined. If the BEC was split and recombined too quickly excitations were created [41]. This increased the temperature of the gas and reduced the visibility of the interference fringes. If the BEC was

recombined too slowly, the instability decreased the population of the odd mode [42] and reduced the visibility of the interference fringes. The optimal splitting and recombination time occurred between these two limits.

1.5.2 BEC interferometers with optical control of dynamics

An alternative method for building a BEC based atom interferometer uses a standing light wave to manipulate a BEC that is confined in a waveguide [33, 34, 43]. This standing light wave is created by two counter-propagating laser beams. The trajectory of the BEC during the interferometric cycle is shown in Fig. 1.7 (a). The cycle of duration T starts at $t = 0$ by illuminating the motionless BEC ψ_0 with a splitting pulse from the laser beams. This pulse acts like a diffraction grating splitting the BEC into two harmonics ψ_+ and ψ_-. The atoms diffracted into the $+1$ order absorb a photon from a laser beam with the momentum $\hbar k_l$ and re-emit it into the beam with the momentum $-\hbar k_l$ acquiring the net momentum of $2\hbar k_l$. The cloud ψ_+ starts moving with the velocity $v_0 = 2\hbar k_l/M$, where k_l is the wavenumber of the laser beams and M is the atomic mass. Similarly, the cloud ψ_- starts moving with the velocity $-v_0$. The two harmonics are allowed to propagate until the time $t = T/2$. At this time the harmonics are illuminated by a reflection optical pulse. The atoms in the harmonics ψ_+ change their velocity by $-2v_0$ and those in the harmonics ψ_- by $2v_0$. The harmonics propagate until the time $t = T$ and are subject to the action of the recombination optical pulse. After the recombination, the atoms in general populate all three harmonics ψ_0 and $\psi_\pm$. The degree of population depends on the phase difference between the harmonics $\psi_\pm$ acquired during the interferometric cycle. By counting the number of atoms in each harmonic the phase difference can be determined. Because the BEC is split and recombined in the same physical location, this type of interferometer is called a Michelson interferometer. A

detailed analysis of the optical pulses used in Michelson interferometers is presented in Appendix A.

The first experiment using a BEC Michelson interferometer was done by the group of Eric Cornell and Dana Z. Anderson at JILA [33]. This interferometer had a coherence time of 10 ms, which is short as compared to the double-well interferometers. The short coherence time was theoretically explained in a model by Maxim Olshanii and Vanja Dunjko [44]. They attributed this loss of coherence to a distortion of the phase across each harmonic. It was caused by both the atom-atom interactions and the residual potential along the waveguide.

A modification of the Michelson interferometer, shown in Fig. 1.7 (b), was built by Cass Sackett's group at the University of Virginia [34]. The interferometry cycle begins at $t = 0$ by illuminating the BEC with a splitting pulse. The two harmonics freely propagate until the time $t = T/4$ when they are illuminated by a reflection pulse. They continue to freely propagate until the time $t = 3T/4$ when a second reflection pulse is applied. The harmonics freely propagate until the time $t = T$ and are subject to the action of the recombination pulse. The phase difference is measured by counting the number of atoms in each harmonic after the recombination pulse. Because of the two reflections, this is called a double reflection Michelson interferometer. This cycle greatly reduces the phase distortion across the BEC increasing the coherence time to 44 ms.

A third interferometer, shown in Fig. 1.7 (c) was recently built by Munekazu Horikoshi and Nenichi Nakagawa [35]. This interferometer had a coherence time of 15 ms and used a different splitting technique. One of the counter-propagating laser beams was frequency-shifted with respect to the other laser beam, resulting in a traveling wave optical potential. The cycle begins at the time $t = 0$ by splitting the BEC. In the previous examples, both harmonics are moving after the BEC

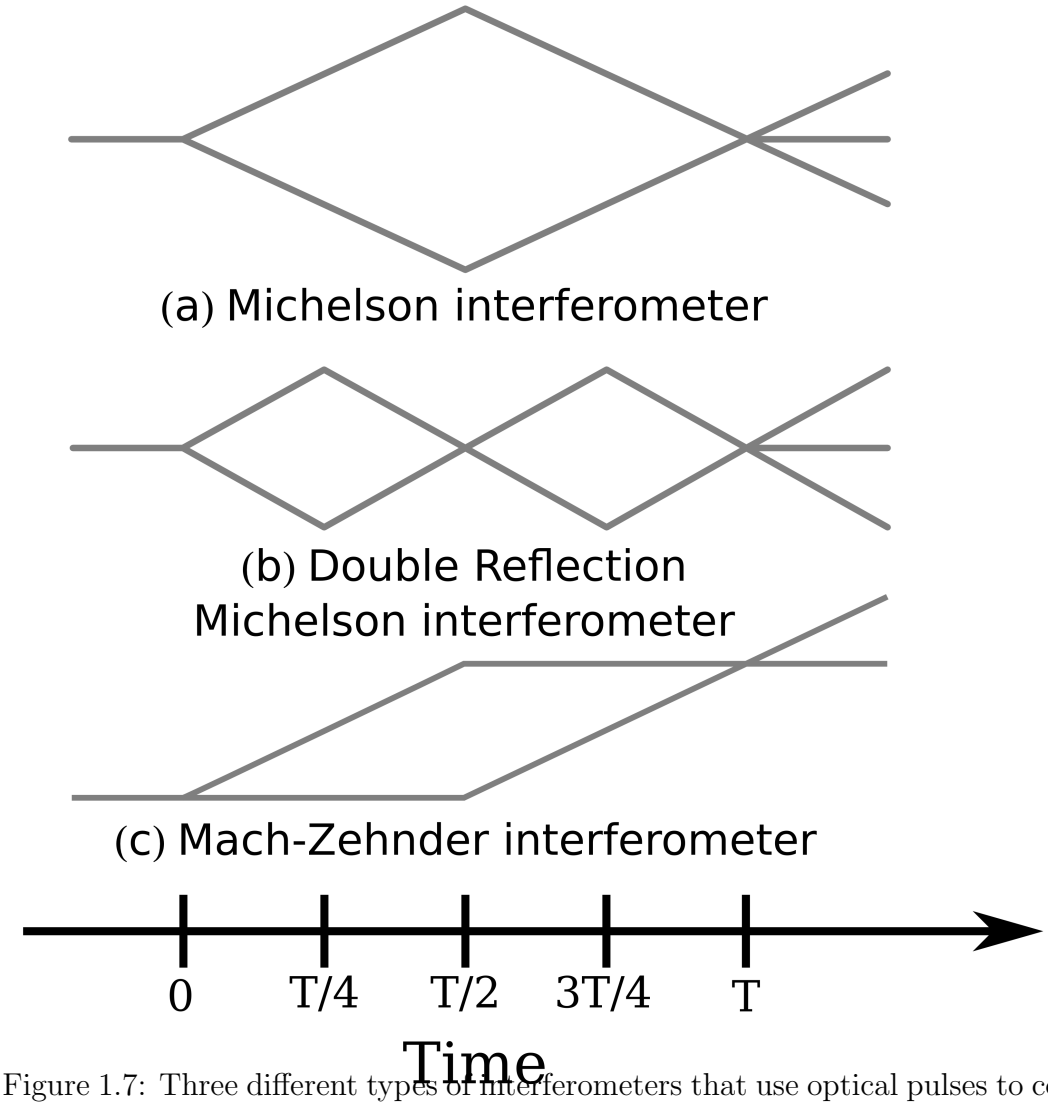

Figure 1.7: Three different types of interferometers that use optical pulses to control the dynamics of the BEC.

is split. In this example one of the harmonics remains at rest and the other one propagates with the momentum $2\hbar k_l$. The harmonics freely propagate until the time $t = T/2$ when they are subject to the action of a reflection pulse. At this time the harmonic that was moving stops and the harmonic that was stationary moves with the momentum $2\hbar k_l$. The harmonics freely propagate until the time $t = T$ when they are illuminated by a recombination pulse. After this recombination pulse, the population of the two harmonics depends on the phase difference that accumulated during the cycle. Because the BEC is not split and recombined in the same physical location, this type of interferometer is called a Mach-Zehnder interferometer.

1.6 Atomtronics

BEC based interferometers operate with similar physical principles as optical interferometers, which is why the study of BEC interferometers is called atom optics. Many different atom optical components have been recently developed using atom chips [22] including atomic waveguides and beamsplitters [45, 46, 47, 48]. These components can be integrated into more complex devices like interferometers [33, 36].

In atom optics, the nonlinearity of the BEC wavefunction, caused by atom-atom interactions, is a major obstacle slowing development. Researchers are now seeking ways to turn this "bug" into a feature. It may be possible to build devices using the BEC nonlinearity that are similar to electronic components. By combining several of these components, on-chip integrated cold atom circuits capable of complex functionality could be constructed.

This emerging field is called atomtronics [49]. Several atomtronic components have been proposed, including diodes [50, 49] and transistors [49, 51, 52]. Some of these proposals use periodic potentials to create a lattice for the BEC and operate

with similar physical principles as semiconductor devices. The transistor described in Chapter 7 of this dissertation has functionality similar to that of a transistor, but is described by completely different physics.

1.7 Organization of the dissertation

The remainder of this chapter contains a brief outline of the major results presented in this dissertation. The main focus of this dissertation is a theoretical analysis of BEC beamsplitters and interferometers with special emphasis on atom chip based devices. The majority of the analysis uses the mean field approximation. In the mean field limit, the dynamics of the BEC is governed by the Gross-Pitaevskii equation [53]. Some effects beyond the mean field which are described by the second-quantization formalism will be presented. Temperature dependent effects are not discussed, and the results presented are only valid when the temperature of the BEC is much less than the critical temperature.

The dissertation begins with a theoretical analysis of the splitting and recombination of a BEC using a double-well potential.

Chapter 2 presents an analysis of the splitting and recombination of a BEC in a symmetric double-well. It describes the two wire beamsplitter, but the results can be easily extended to any double-well interferometer. This chapter demonstrates that the BEC must be split and recombined sufficiently slowly to avoid collective excitations and that this is relatively insensitive to the nonlinearity of the BEC. It also shows that the recombination must be done sufficiently quickly to avoid a recombination instability. This instability is analyzed using both a two mode approximation and by numerically solving the Bogoliubov-de Gennes equations.

Chapter 3 presents an analysis of the double-well interferometer, with the par-

ticular emphasis on measuring accelerations. The acceleration of the interferometer breaks the symmetry of the double-well and the effect of this on the visibility of the interference fringes is analyzed. An analytic model of the interferometer is presented. It is used to place an upper limit on the acceleration that can be measured by a double-well interferometer.

A beamsplitter that uses a time dependent asymmetric double-well potential is proposed in Chapter 4. It is shown that it is possible to split a BEC using such a potential. The primary advantage of this type of splitter is that it can split the BEC into two unequal parts, which may be particularly useful in atomtronic devices.

Chapter 5 is the first of two chapters that analyzes the operation of a BEC Michelson interferometer that uses optical pulses to control the dynamics. A simple and accurate analytic model of this type of interferometer is introduced. This model is used to offer a simple physical explanation of the coherence time of the interferometer. When the potential along the guide is flat, the coherence time may be greatly increased by simply recombining the BEC at a shifted time.

Chapter 6 presents an analysis of a BEC Michelson interferometer, in which the BEC is confined by a weak trapping potential along the guide. The analytic model of Chapter 5 is extended to include both the single and double reflection Michelson interferometers that are shown in Fig. 1.7 (a) and (b). The model is used to place upperlimits on both coherence time and total number of atoms in the BEC.

A proposal for an atomtronic transistor is the subject of Chapter 7. This proposed transistor uses a nonsymmetric triple-well potential where the number of atoms in the middle well are used to control the number of atoms that tunnel from the left to the right well. A model for the dynamics of the atoms in this triple-well is used to demonstrate that this transistor has both absolute and differential gain. The model is also used to demonstrate that it is possible to build a BEC transistor

that is switched by placing a single atom in the middle well.

Chapter 2

Theoretical analysis of a double-well beamsplitter

2.1 Introduction

In this chapter, we analyze performance of double well atom beamsplitters. Section 2.2 formulates the theoretical background for analyzing evolution of the condensate in the splitting region in the framework of a mean-field approximation. Our model allows for nonlinearity, nonadiabaticity, and multimode propagation of an atomic cloud through the splitter. In Sec. 2.3 we specialize to a particular form of the guiding potential created by two parallel current carrying wires and a uniform external magnetic field (bias field) [27] and discuss two representative realizations of such a potential to be used in subsequent analysis. One of them essentially operates as a Y-junction and the other as a coherent optical coupler. Sections 2.4 and 2.5 analyze splitting and recombination of the condensate in the geometry of a Y-junction.

2.2 Formulation of the problem

The evolution of a Bose-Einstein condensate in a guiding potential $V(X,Y,Z) = V(\mathbf{R})$ in the mean-field approximation is described by time-dependent Gross-Pitaevskii equation

$$i\hbar\frac{\partial}{\partial T}\Psi(\mathbf{R},T) = \left[-\frac{\hbar^2}{2M}\nabla^2 + V(\mathbf{R}) + U_0|\Psi|^2\right]\Psi. \tag{2.1}$$

The condensate wave function Ψ is normalized to unity, $U_0 = 4\pi a_s\hbar^2 N/M$, where M is the atom mass, N is the total number of atoms, and a_s is the s-wave scattering length. The potential V contains a region that coherently splits or recombines the wave function of the condensate. In the splitting region, L is the characteristic length of change of the potential V along the Z axis and ω_0 is the characteristic guiding frequency in the transverse (XY) plane. In this section we will formulate the theoretical background for analyzing evolution of the condensate in the splitting

region.

We assume that the BEC is moving as a whole and represent the wave function as

$$\Psi(\mathbf{R},t) = \phi(\mathbf{R},t)\exp(ik_pZ - i\omega_pT), \tag{2.2}$$

where k_p and $\omega_p = \hbar k_p^2/2M$ are the carrier wave number and frequency, respectively, and ϕ is the wave function envelope. The equation for the envelope ϕ in the co-propagating frame $T' = T$, $Z' = Z - vT$ is of the form

$$i\hbar\frac{\partial}{\partial T}\phi = \left[-\frac{\hbar^2}{2M}\left(\frac{\partial^2}{\partial Z^2} + \nabla_\perp^2\right) + V(X,Y,Z+vT) + U_0\right]\phi, \tag{2.3}$$

where $v = \hbar k_p/M$ and the primes have been omitted.

Below we will formulate a set of inequalities that will allow us to neglect the dispersive ($\partial^2/\partial Z^2$) term in Eq. (2.3).

The energy associated with the longitudinal motion of the wavepacket as a whole is assumed to be much larger than the characteristic eigenenergies $\hbar\omega_0$ of transverse eigenmodes of the splitting region: $\hbar^2k_p^2/2M \gg \hbar\omega_0$, or

$$k_pa_0 \gg 1, \tag{2.4}$$

where $a_0 = (\hbar\omega_0/M)^{1/2}$ is the transverse oscillator length. This inequality ensures that small changes in the group velocity of the envelope when it moves through the splitter, can be neglected.

The splitting region will introduce spatial changes in the wave function with the characteristic spatial scale L. We assume that

$$k_pL \gg 1. \tag{2.5}$$

Equation (2.5) serves two purposes. First, it ensures that undesirable reflection of the wave function from the splitting region (generation of the wave function $\propto \exp(-ik_pZ - i\omega_pT)$) is exponentially small and can be neglected. Secondly, Eq. (2.5) means that contributions from the $\partial^2/\partial Z^2$ term in Eq. (2.3) with $|\partial/\partial Z| \approx 1/L$ are small. Note that the limit $k_pL \gg 1$ prevents reflection but allows for nonadiabaticity and multimode propagation of the atomic cloud through the splitting region. The degree of adiabaticity is governed by the parameter $\nu = L\omega_0/v = L/k_pa_0^2$ that can be both larger and smaller than unity in our analysis. The limit $k_pL \gg 1$ is opposite to that of Ref. [54], which studied reflections from discontinuities of a guiding potential in the adiabatic single-transverse-mode approximation and steady-state regime.

The expanding BEC entering the splitting region has the characteristic longitudinal size L_{BEC} and the longitudinal phase $\theta(Z)$. We assume that the kinetic energy associated with the expansion in the longitudinal direction is small in comparison with the characteristic eigenenergy $\hbar\omega_0$ associated with transverse eigenmodes of the splitter

$$\hbar\omega_0 \gg \frac{\hbar^2}{2ML_{BEC}^2},\ \frac{\hbar^2}{2M}\left|\frac{\partial^2}{\partial Z^2}\theta\right|. \tag{2.6}$$

Finally, we require that neither L_{BEC} nor $\theta(Z)$ change appreciably during the time interval L/v that it takes the packet to propagate through the splitter

$$\left|\frac{\partial}{\partial T}\ln L_{BEC}\right|,\ \left|\frac{\partial}{\partial T}\ln\theta\right| \ll \frac{v}{L}. \tag{2.7}$$

Simple estimates based on the BEC expansion of Ref. [42] translate Eqs. (2.6) and (2.7) into the requirements

$$\omega_0 T_{exp} \gg 1 \tag{2.8}$$

and

$$\frac{v}{L\omega_0} = \frac{k_p a_0^2}{L} \gg (\omega_0 T_{exp})^{-1}, \tag{2.9}$$

respectively. Here T_{exp} is the time it takes the BEC cloud to reach the splitting region after being released from the trap.

With Eqs. (2.4)-(2.7) fulfilled, the dispersive term in Eq. (2.3) can be neglected and the coordinate Z becomes a parameter. Propagation of different "slices" of the wavepacket (parametrized by the coordinate Z) through the splitting region can be analyzed independently. For each slice

$$\frac{\partial}{\partial T} \int dX dY |\phi(X, Y, Z, T)|^2 = 0 \tag{2.10}$$

during propagation through the splitting region.

Normalizing time to the characteristic frequency ω_0 ($t = \omega_0 T$), the coordinates to the oscillator length $a_0 = (\hbar/\omega_0 M)^{1/2}$ ($\mathbf{r} = \mathbf{R}/a_0$), and introducing the normalized wave function

$$\psi(x, y, t) = a_0 \frac{\phi(X, Y, Z, T)}{[\int dX dY |\phi|^2]^{1/2}} \tag{2.11}$$

(parametrically depending on Z), we can reduce Eq. (2.3) to the final dimensionless form

$$i\frac{\partial}{\partial t}\psi(x, y, t) = \left[-\frac{1}{2}\nabla_\perp^2 + U(x, y, t) + P|\psi|^2\right]\psi(x, y, t) \tag{2.12}$$

The wave function $\psi(x, y, t)$ is normalized to unity with respect to the dimensionless coordinates x and y:

$$\int dx dy |\psi(x, y, t)|^2 = 1, \tag{2.13}$$

$U = V/\hbar\omega_0$, and

$$P = 4\pi a_s N \int dX dY |\phi|^2 \tag{2.14}$$

is the nonlinearity parameter (parametrically depending on Z). Its order-of-magnitude value for the central part of the cloud is $P \approx 4\pi a_s N/L_{BEC}$.

2.3 Two-wire magnetic beamsplitter

In this section, we specialize to a particular form of the guiding potential V created by two parallel current carrying wires and a uniform external magnetic field (bias field). This two-wire magnetic guide and beamsplitter was previously analyzed in Ref. [27].

Consider two parallel wires separated by the distance $2d$ and carrying equal currents I in the positive Z-direction. Adding uniform bias magnetic field B_{bx} parallel to the X-axis to the magnetic field of the wires creates a configuration of the total magnetic field B with two zeros. This configuration serves as a guiding structure for low-field-seeking atoms. To avoid spin-flip losses in the vicinity of the zeros, a small uniform bias field B_{bz} parallel to the Z-axis is additionally applied so that components of the total magnetic field become

$$\begin{aligned} B_x &= \frac{\mu_0 I}{2\pi}\left[\frac{-Y}{(X-d)^2+Y^2}+\frac{-Y}{(X+d)^2+Y^2}\right]+B_{bx}, \\ B_y &= \frac{\mu_0 I}{2\pi}\left[\frac{X-d}{(X-d)^2+Y^2}+\frac{X+d}{(X+d)^2+Y^2}\right], \\ B_z &= B_{bz}. \end{aligned} \tag{2.15}$$

Energy of a low-field-seeking atom in the magnetic field of amplitude B is given by the relation

$$V = g_F \mu_B m_F B, \tag{2.16}$$

where μ_B is the Bohr magneton, m_F is the magnetic quantum number of the total

atomic angular momentum F, and g_F is the Lande factor.

We define the characteristic frequency ω_0 and the characteristic size a_0 by the relations

$$\omega_0 = \frac{1}{y_0}\left(\frac{g_F \mu_B m_F B_{bx}}{M}\right)^{1/2} \tag{2.17}$$

and

$$a_0 = \left(\frac{\hbar}{M\omega_0}\right)^{1/2}, \tag{2.18}$$

where $y_0 = \mu_0 I/(2\pi B_{bx})$ is the characteristic scale of change of the magnetic field.

Using these definitions and the expressions for the components of the magnetic field of the guiding structure Eq. (2.15), the potential energy of an atom can be expressed as

$$V = \hbar\omega_0 U(x,y) \tag{2.19}$$

where

$$U(x,y) = [b_x^2(x,y) + b_y^2(x,y) + b_z^2]^{1/2} \tag{2.20}$$

and

$$\begin{aligned} b_x &= \epsilon^{-2}\left[1 - \frac{(1+\epsilon y)}{(\beta_x - \epsilon x)^2 + (1+\epsilon y)^2} - \frac{(1+\epsilon y)}{(\beta_x + \epsilon x)^2 + (1+\epsilon y)^2}\right], \\ b_y &= \epsilon^{-2}\left[\frac{-\beta_x + \epsilon x}{(\beta_x - \epsilon x)^2 + (1+\epsilon y)^2} + \frac{\beta_x + \epsilon x}{(\beta_x + \epsilon x)^2 + (1+\epsilon y)^2}\right], \\ b_z &= \epsilon^{-2}\beta_z. \end{aligned} \tag{2.21}$$

Dimensionless coordinates x and y in Eq. (2.20) and (2.21) are normalized to a_0 and the coordinate y is measured from ϵ^{-1} (the dimensional Y is measured from $Y = y_0$). Control parameters β_x and β_z are determined by the relations $\beta_x = d/y_0$ and $\beta_z = B_{bz}/B_{bx}$. Finally, $\epsilon = a_0/y_0$ is the ratio of the characteristic size of the eigenmode to the characteristic size of change of the magnetic field. Typically, this

parameter is small as compared to one. For example, taking $B_{bx} = 20G$, $y_0 = 50\mu m$, $m_F = -1$, $g_F = -1/2$, and $M = 1.45 \times 10^{-25} kg$ (^{87}Rb) yields $\epsilon = 0.8 \times 10^{-2}$.

The potential Eq. (2.20) has two minima. The value $\beta_x = 1$ corresponds to the case when these minima coalesce and are located at the coordinate origin $(x, y) = (0, 0)$. For $\beta_x > 1$, the minima are aligned horizontally and located at the points with the coordinates

$$\begin{aligned} x &= \pm\epsilon^{-1}(\beta_x^2 - 1)^{1/2}, \\ y &= 0. \end{aligned} \tag{2.22}$$

For $\beta_x < 1$, the minima are aligned vertically and located at the points with the coordinates

$$\begin{aligned} x &= 0, \\ y &= \pm\epsilon^{-1}(1 - \beta_x^2)^{1/2}. \end{aligned} \tag{2.23}$$

The dependence of the guiding potential on the value of β_x allows one to use this configuration for splitting or recombination of the condensate. A change from $\beta_x < 1$ to $\beta_x > 1$ first merges two initially vertically separated guides and then separates them horizontally as shown in Fig. 2.1. This change can be effected by changing either the distance between the wires or the transverse bias field in some region in space. An atomic cloud launched in either of two vertically separated guides will be symmetrically split between the left and the right guide. We will refer to this as the Y-junction geometry.

Knowledge of local transverse eigenmodes of the splitter is essential for analyzing its performance. These eigenmodes $\phi_n(x, y, \beta_x)$ and their eigenfrequencies $\omega_n(\beta_x)$

Figure 2.1: Schematic view of the splitting region. Parameter β_x increases from the lower left to the upper right of the figure passing through $\beta_x = 1$ in the center when two guides merge into one.

are solutions of the boundary value problem

$$\omega_n \phi_n(x, y, \beta_x) = \left[-\frac{1}{2}\nabla^2 + U(x, y, \beta_x) \right] \phi_n(x, y, \beta_x) \tag{2.24}$$

and parametrically depend on the control parameter β_x.

Several lowest eigenfrequencies are shown in Fig. 2.2 versus transverse bias field $\Delta\beta_x = \beta_x - 1$ for $\epsilon = 0.01$ and $\beta_z = 0.1$. Due to the presence of the longitudinal bias field ($\beta_z \neq 0$), the potential U (2.20) is positive everywhere including its minimuma. In calculating Fig. 2.2, the potential was shifted down by a constant: $U(x, y, \beta_x) \to U(x, y, \beta_x) - U(0, 0, 1)$ so that its minimum value became zero. This shift removes an additive constant background frequency $U(0, 0, 1)$ that is the same for all eigenmodes. Negative values of $\Delta\beta_x$ in Fig. 2.2 correspond to the lower left part of Fig. 2.1 with two guides separated vertically. At large negative values of $\Delta\beta_x$ the guides are far away from each other and can be treated independently. We

Figure 2.2: Several lowest eigenfrequencies of the splitting region versus transverse bias field for $\epsilon = 0.01$ and $\beta_z = 0.1$.

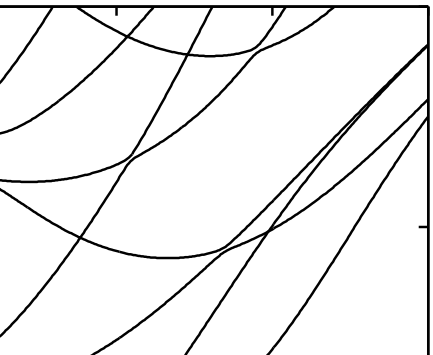

Table 2.1: The asymptotic arrangement of the first eight modes, from the lowest to the highest.

	Mode 1	Mode 2	Mode 3	Mode 4	Mode 5	Mode 6	Mode 7	Mode 8
$\Delta\beta_x < 0$	$(0,0)_u$	$(0,0)_l$	$(0,1)_u$	$(1,0)_u$	$(0,1)_l$	$(1,0)_l$	$(0,2)_u$	$(1,1)_u$
$\Delta\beta_x > 0$	$(0,0)_s$	$(0,0)_a$	$(1,0)_s$	$(1,0)_a$	$(0,1)_s$	$(0,1)_a$	$(2,0)_s$	$(2,0)_a$

Table 2.2: Modal mapping from $\Delta\beta_x < 0$ to $\Delta\beta_x > 0$.

	$1 \to 1$	$2 \to 3$	$3 \to 5$	$4 \to 2$	$5 \to 7$	$6 \to 4$
$\Delta\beta_x < 0$	$(0,0)_u$	$(0,0)_l$	$(0,1)_u$	$(1,0)_u$	$(0,1)_l$	$(1,0)_l$
$\Delta\beta_x > 0$	$(0,0)_s$	$(1,0)_s$	$(0,1)_s$	$(0,0)_a$	$(2,0)_s$	$(1,0)_a$

will specify eigenmodes of the splitter in this limit using the nomenclature $(n,m)_{u(l)}$, where the subscript "u(pper)" or "l(ower)" denotes whether an eigenmode is localized in the upper of the lower guide and n and m are integers denoting number of nodes of the wave function along the x and y axes, respectively.

Positive values of $\Delta\beta_x$ correspond to the the upper right part of Fig. 2.1 with two guides separated horizontally. For large positive values of $\Delta\beta_x$ all modes become pairwise-degenerate. This degeneracy is due to the fact that the potential U is symmetric in x and thus the left and the right guides are mirror reflections of each other. A member of a pair with slightly lower (higher) energy is the symmetric (antisymmetric) mode of the whole splitter. A sum or difference of these two modes in the limit $\Delta\beta_x \to \infty$ is an eigenmode of the left or the right guide. Eigenmodes of the splitter in the limit $\Delta\beta_x \to \infty$ will be specified as $(n,m)_{s(a)}$. The subscript "s(ymmetric)" or "a(ntisymmetric)" indicates whether an eigenmode is a symmetric or antisymmetric combination of eigenmodes of the left and the right guides. Integers n and m denote the number of nodes of the wave function in each individual guide along the x and y axes, respectively.

The asymptotic ($|\Delta\beta_x|/\epsilon^2 = 50$) arrangement of the lowest eight modes of the splitter for the parameters of Fig. 2.2, in order of increasing frequency, is shown in Table 2.1.

The mapping between these modes is shown in Table 2.2. The first row of the table shows the mapping in terms of modal numbers counted from the lowest frequency. The second two rows of the table show the input and the corresponding output mode, respectively. Table 2.2 can be summarized as follows: an input mode maps onto the lowest available output mode with the same parity along the x-axis. The parity along the y-axis in general is not preserved. Thus, the lowest symmetric mode $(0,0)_l$ maps onto the lowest symmetric mode $(0,0)_s$. Since the mode $(0,0)_s$ is already mapped onto, the next lowest symmetric mode $(0,0)_l$ maps onto the next lowest available symmetric mode $(1,0)_s$ and so on.

2.4 Analysis of splitting

In this section, we analyze splitting of the atomic cloud. Specifically, we are interested in the situation when the condensate is launched in the potential of Fig. 2.1 from the $\Delta\beta_x < 0$ side as the lowest mode of either the upper or the lower guide and is symmetrically split between the left and the right guides on the $\Delta\beta_x > 0$ side. The situation when the cloud is launched from the $\Delta\beta_x > 0$ side as a linear combination of the lowest modes of the right and the left guides will be referred to as recombination. Analysis of the recombination will be presented in the next section.

The modal mapping of the previous section giving the relation between the input and the output modes of the splitting region, is valid in the adiabatic limit. To determine the region of parameters corresponding to the adiabatic regime, we analyzed the propagation of the lowest eigenmodes through the splitting region for different values of the splitter length L, i.e., for different values of the adiabaticity parameter $\nu = L\omega/v$. After the propagation, the output wave function ψ_{out} was mapped onto

the output transverse eigenmodes of the splitter. The degree of population of these eigenmodes was quantified by calculating the output modal populations P_n

$$P_n = \left| \int dxdy \psi_{out}(x,y) \phi_n(x,y) \right|^2, \tag{2.25}$$

where ϕ_n are transverse eigenmodes of the splitter discussed in Sec. 2.3. Analysis of adiabaticity has been carried out for zero nonlinearity $P = 0$ in Eq. (2.12).

To quantify values of the adiabaticity parameter for a given rate of change of the magnetic field or the distance between the wires (i.e., rate of change of the control parameter $\Delta\beta_x$), we have to relate this rate of change with the characteristic splitter size L. To do this, we return to Eq. (2.21). In the limit $\epsilon \ll 1$, these equations simplify to

$$\begin{aligned} b_x &= \frac{1}{2}(y^2 - x^2) + \Delta\beta_x \epsilon^{-2}, \\ b_y &= x(y - \Delta\beta_x \epsilon^{-1} + \epsilon x^2/2), \\ b_z &= \beta_z \epsilon^{-2}. \end{aligned} \tag{2.26}$$

Assume that the control parameter $\Delta\beta_x$ linearly depends on the (dimensional) coordinate Z: $\Delta\beta_x(Z) = Z/L_0$. The zero value of Z corresponds to two guides merged into one. The characteristic size L of the splitting region can be specified by the condition that the change in $\Delta\beta_x$ corresponding to $Z = \pm L$ ($\Delta\beta_x = \pm L/L_0$) spatially separates eigenmodes of two guides by their characteristic size. Inspection of Eq. (2.26) shows that for $\beta_z = 0$, the characteristic size of an eigenmode d in dimensionless variables is one ($d \propto 1$) and the characteristic size of the splitter is given by the relation $L \propto L_0 \epsilon^2$. The characteristic frequency of an eigenmode ω is

about ω_0 and thus the adiabaticity parameter can be evaluated as

$$\nu = L_0 \epsilon^2 \omega_0 / v. \tag{2.27}$$

In the opposite limit of large values of the longitudinal bias $b_z \gg 1$, the characteristic size of an eigenmode can be evaluated as

$$d \propto (4\beta_z \epsilon^{-2})^{1/6} \tag{2.28}$$

and the splitter size as

$$L \propto L_0 \epsilon^2 (4\beta_z \epsilon^{-2})^{1/3}. \tag{2.29}$$

The characteristic frequency of an eigenmode is given by

$$\omega \propto \omega_0 (4\beta_x \epsilon^{-2})^{-1/3} \tag{2.30}$$

and the adiabaticity parameter can be introduced by the relation

$$\nu = L\omega/v = L_0 \epsilon^2 (4\beta_z \epsilon^{-2})^{1/3} \omega_0 (4\beta_x \epsilon^{-2})^{-1/3} = L_0 \epsilon^2 \omega_0 / v. \tag{2.31}$$

Nonzero values of the longitudinal bias β_z result in an increase of the characteristic modal size Eq. (2.28) and the corresponding increase in the splitter length Eq. (2.29). This increase is compensated by lower values of the modal frequency so that the product $L\omega/v$ remains the same. The fact that expressions (2.27) and (2.31) for the adiabaticity parameter have the same form in both limiting cases indicates that this form can be used for any intermediate value of the longitudinal bias field β_z.

In the co-propagating frame of Eq. (2.12), the rate of change of the control

parameter β_x can thus be expressed as

$$\Delta\beta_x(t)\epsilon^{-2} = t/\nu. \tag{2.32}$$

In our analysis, the splitting region was represented by the relation

$$\Delta\beta_x(t)\epsilon^{-2} = \beta_{max}\tanh(t/\beta_{max}\nu) \tag{2.33}$$

Equation (2.33) describes two vertically-displaced guides running parallel to each other at large negative values of t, merging at $t = 0$ and separating horizontally at large positive values of t as shown in Fig. 2.1. In all subsequent calculations $\beta_{max} = 50$ ensuring that the guides are well asymptotically separated.

We now discuss the criteria of adiabaticity for the case when the input wave function is the lowest transverse eigenmode of the splitter for $\beta_x < 0$, i.e., the $(0,0)_u$ eigenmode.

Figure 2.3 shows the modal decomposition coefficients P_n at the output of the splitter versus the adiabaticity parameter ν. All parameters are the same as for Fig. 2.2 and $\beta_{max} = 50$. In the adiabatic limit, the input wave function $(0,0)_u$ should become the $(0,0)_s$ at the output of the splitter (see Table 2.2). Figure 2.3 shows that the output wave function contains noticeable contributions of higher transverse eigenmodes, primarily the eigenmode $(1,0)_s$, even at the values of ν as high as $\nu = 10$.

Contour plots of the input eigenmode ($t \to -\infty$), and of the three first symmetric output ($t \to \infty$) eigenmodes of the splitter are shown in Fig. 2.4. Solid lines correspond to positive values of the eigenmode, and dashed ones to the negative values.

Surface plots of the modulus of the output wave function in the nonadiabatic

Figure 2.3: Modal decomposition coefficients versus adiabaticity parameter.

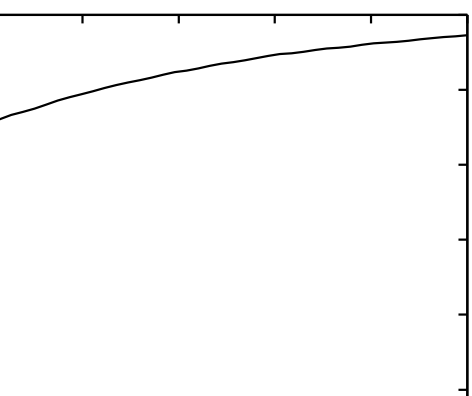

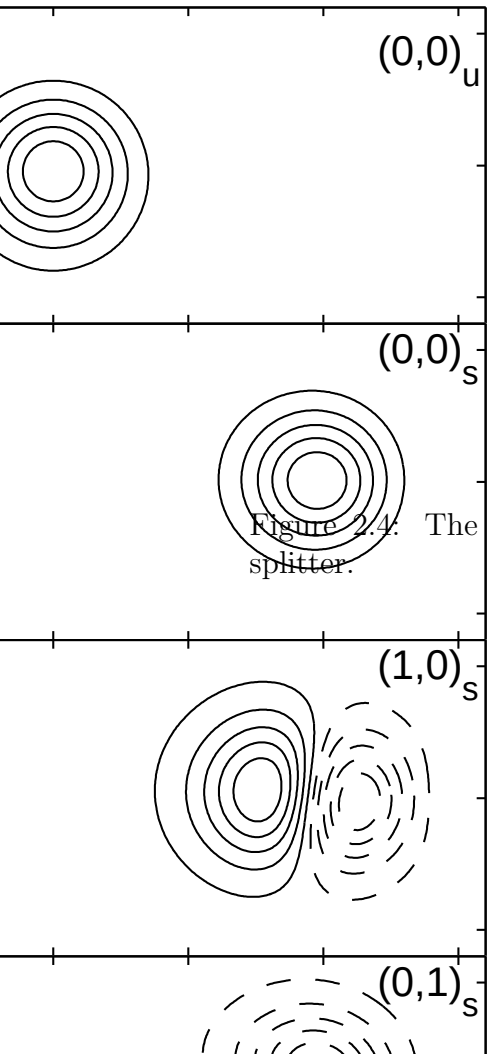

Figure 2.4: The input and the three first symmetric output eigenmodes of the splitter.

limit $\nu = 2$ are shown in Fig. 2.5. The output wave function is a superposition of several transverse modes and so its maximum value, characteristic diameter and shape change with time. The low-intensity protrusions in Fig. 2.5 move around the central part as the wave function propagates down the splitter.

2.5 Analysis of recombination

In this section we shall analyze recombination of the atomic cloud. Here the condensate is launched in the potential of Fig. 2.1 from the $\Delta\beta_x > 0$ side as a linear combination of the lowest modes of the right and the left guides ϕ_l and ϕ_r:

$$\psi_{in} = \frac{1}{\sqrt{2}}\left(\phi_l e^{-i\Delta\phi/2} + \phi_r e^{i\Delta\phi/2}\right), \tag{2.34}$$

where

$$\begin{aligned} \phi_l &= \frac{1}{\sqrt{2}}\left[(0,0)_s + (0,0)_a\right] = \frac{1}{\sqrt{2}}[\phi_1 + \phi_2], \\ \phi_r &= \frac{1}{\sqrt{2}}\left[(0,0)_s - (0,0)_a\right] = \frac{1}{\sqrt{2}}[\phi_1 - \phi_2]. \end{aligned} \tag{2.35}$$

We are allowing for an arbitrary phase shift $\Delta\phi$ between the wave functions of the left and the right guides. This shift is assumed to be caused by differences in local environments sampled by the guides.

Criteria of adiabaticity for recombination in the limit of zero nonlinearity $P = 0$ are about the same as for the above-discussed splitting case and require $\nu \propto 20$. In the adiabatic regime $\phi_1 = (0,0)_s \rightarrow (0,0)_u$ and $\phi_2 = (0,0)_a \rightarrow (1,0)_u$, i.e., both modes end up in the upper guide. The nonlinearity, on the other hand, affects recombination much more strongly than it affects splitting. Nonlinear recombination effects are especially pronounced in the adiabatic regime. The subsequent analysis

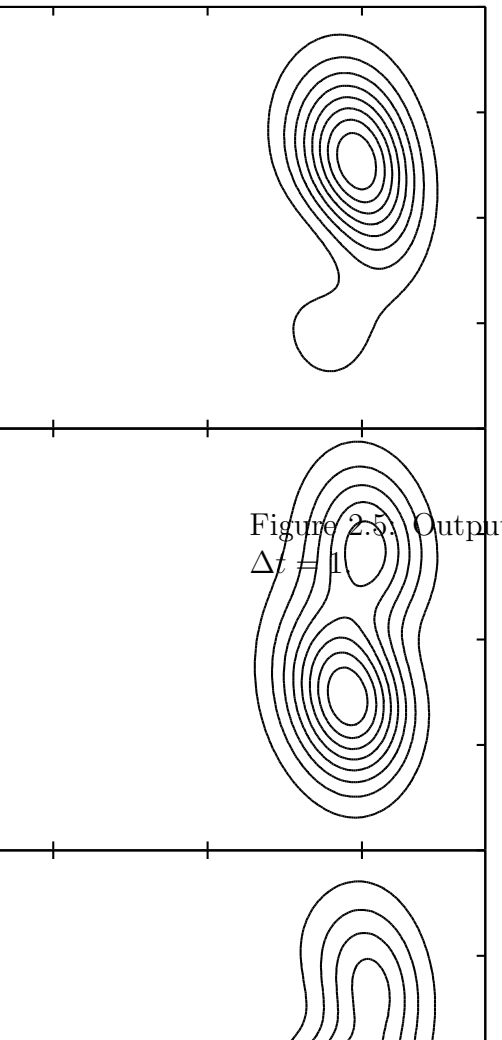

Figure 2.5: Output amplitude $|\psi|$ for $\nu = 2$ and three values of time separated by $\Delta t = 1$.

deals with the influence of the nonlinearity and will be carried out in the adiabatic regime $\nu \gg 1$.

Decomposing the wave function of the condensate into a complete set of local transverse eigenmodes $\phi_n(x, y, t)$ of the guiding potential

$$\begin{aligned} \psi(x, y, t) &= \sum_{n=0}^{\infty} A_n(t)\phi_n(x, y, t), \\ A_n(t) &= \int dxdy\psi(x, y, t)\phi_n(x, y, t), \end{aligned} \tag{2.36}$$

and substituting (2.36) into Eq. (2.12), results in a set of coupled equations for the modal amplitudes A_n

$$i\frac{d}{dt}A_n = \omega_n A_n + P\sum_{k,l,m}\kappa_{nklm}(t)A_k A_l^* A_m, \tag{2.37}$$

where

$$\kappa_{nklm}(t) = \int dxdy\phi_n\phi_k\phi_l\phi_m. \tag{2.38}$$

are the overlap integrals. Both the eigenfunctions ϕ_n and their eigenfrequencies ω_n parametrically depend on time through time dependence of the guiding potential.

For $\nu \gg 1$ and moderate values of P, the nonlinearity does not generate new modes and we can limit ourselves only to two modes ϕ_1 and ϕ_2 that are present at the input. Keeping only A_1 and A_2 in Eq. (2.37) results in a set of two coupled equations

$$\begin{aligned} i\frac{d}{dt}A_1 &= \omega_1(t)A_1 + P\left[\kappa_{11}(t)|A_1|^2A_1 + \kappa_{12}(t)\left(2|A_2|^2A_1 + A_2^2A_1^*\right)\right], \\ i\frac{d}{dt}A_2 &= \omega_2(t)A_2 + P\left[\kappa_{22}(t)|A_2|^2A_2 + \kappa_{12}(t)\left(2|A_1|^2A_2 + A_1^2A_2^*\right)\right], \end{aligned} \tag{2.39}$$

where $\kappa_{11} = \kappa_{1111}$, $\kappa_{12} = \kappa_{1122}$ and $\kappa_{22} = \kappa_{2222}$.

The input wave function ψ_{in} (2.34) in terms of ϕ_1 and ϕ_2 reads

$$\psi_{in} = \cos(\Delta\phi/2)\phi_1 - i\sin(\Delta\phi/2)\phi_2, \tag{2.40}$$

resulting in the initial conditions

$$\begin{aligned} A_1(-\infty) &= \cos(\Delta\phi/2), \\ A_2(-\infty) &= -i\sin(\Delta\phi/2). \end{aligned} \tag{2.41}$$

Representing complex amplitudes A_i $(i = 1, 2)$ in the form

$$A_i(t) = c_i(t)\exp\left[-i\int^t \omega_i(t')dt' + i\theta_i(t)\right], \tag{2.42}$$

where c_i and θ_i $(i = 1, 2)$ are real functions, transforms Eq. (2.39) to the form

$$\begin{aligned} \frac{d}{dt}c_1 &= P\kappa_{12}c_2^2 c_1 \sin\Theta, \\ \frac{d}{dt}c_2 &= -P\kappa_{12}c_1^2 c_2 \sin\Theta, \\ \frac{d}{dt}\theta_1 &= -P\left[\kappa_{11}c_1^2 + \kappa_{12}c_2^2(2 - \cos\Theta)\right], \\ \frac{d}{dt}\theta_2 &= -P\left[\kappa_{22}c_2^2 + \kappa_{12}c_1^2(2 - \cos\Theta)\right]. \end{aligned} \tag{2.43}$$

Here $\Theta = 2(\Omega + \theta_1 - \theta_2) - \pi$, $\Omega(t) = \int_{-\infty}^t dt'\Delta\omega(t')$, and $\Delta\omega(t) = \omega_2(t) - \omega_1(t)$. Note that $\Theta(-\infty) = 0$, since $\theta_1(-\infty) - \theta_2(-\infty) = \pi/2$ (see Eq. (2.41)).

Accounting for the integral of motion $c_1^2 + c_2^2 = 1$, reduces Eq. (2.43) to the set of equations for the function $\Theta(t)$ and the population difference $y = c_2^2 - c_1^2$

$$\frac{d}{dt}y = -P\kappa_{12}(t)(1 - y^2)\sin\Theta,$$

$$\begin{aligned}\frac{d}{dt}\Theta &= 2\Delta\omega + P\left[\kappa_{22}(1+y)\right. \\ &- \left.\kappa_{11}(1-y) - 2\kappa_{12}y(2-\cos\Theta)\right]. \end{aligned} \tag{2.44}$$

Solution of the equation for y with the initial condition $y(-\infty) = -\cos(\Delta\phi)$ can be written as

$$y(t) = \frac{-\tanh P\tau - \cos(\Delta\phi)}{1 + \cos(\Delta\phi)\tanh P\tau} \tag{2.45}$$

where

$$\tau(t) = \int_{-\infty}^{t} \kappa_{12}(t')\sin\Theta(t')dt'. \tag{2.46}$$

Typical values of the overlap integrals κ_{ij} are of the order of d^{-2}, where d is the characteristic size of an eigenmode, and are rather small for our parameters (about 10^{-2}). Thus, for moderate nonlinearity $P \leq 1$, the evolution of the phase angle $\Theta(t)$ is primarily determined by the frequency difference $\Delta\omega(t)$:

$$\Theta(t) = 2\Omega(t) = 2\int^{t} dt'\Delta\omega'(t'). \tag{2.47}$$

In this regime the function $\tau(t)$ (2.46) is independent of either the nonlinearity parameter P or the phase shift $\Delta\phi$ and becomes "universal" (has to be calculated only once):

$$\tau(t) = \int_{-\infty}^{t} dt'\kappa_{12}(t')\sin 2\Omega(t'). \tag{2.48}$$

Function $\tau(t)$ (2.48) is plotted in Fig. (2.6) for the potential given by Eq. (2.20) and (2.21) and the adiabaticity parameter $\nu = 20$. All other parameters are the same as for previous figures. The output modal population of the lowest mode calculated with the help of Eq. (2.45) and Eq. (2.48) is presented in Fig. 2.7. The dotted line corresponds to the linear recombination $c_1^2 = cos^2\Delta\phi/2$. Figure 2.7 demonstrates that, as compared with the linear case, the nonlinearity always increases population

Figure 2.6: Function $\tau(t)$ Eq. (2.48).

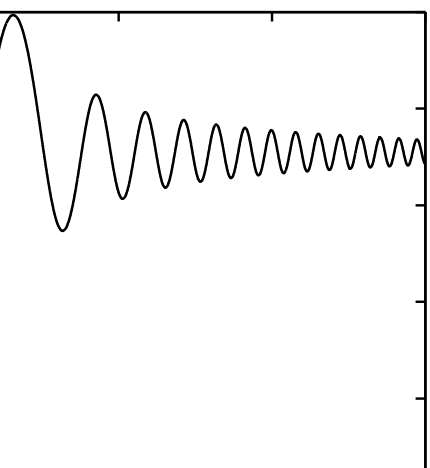

Figure 2.7: Output population of the lowest mode $(0,0)_u$ as a function of the relative phase shift for several values of the nonlinearity parameter P.

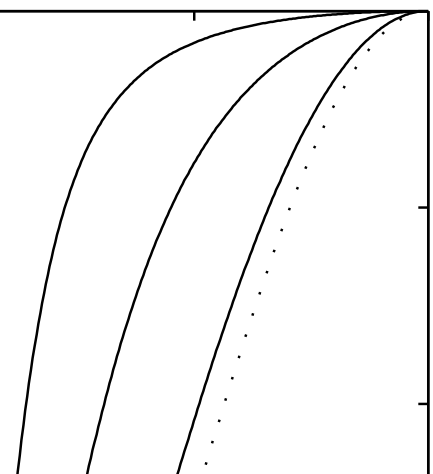

of the lowest mode $(0,0)_u$ at the expense of the higher mode $(1,0)_u$. For a given value of the nonlinearity parameter P, the effect becomes larger with an increase in the splitting region length ,i.e., the adiabaticity parameter ν.

Indeed, the frequency difference $\Delta\omega = \omega_2 - \omega_1$ in Eq. (2.47) can be approximated by the relation

$$\Delta\omega \approx \omega(t/\nu), \tag{2.49}$$

where ω is the characteristic intermodal spacing at the end of the recombination given by Eq. (2.30) (or equal to one for $\beta_z = 1$). Therefore,

$$\Theta(t) = 2\int^t dt' \Delta\omega \approx \frac{t^2}{\nu} \tag{2.50}$$

and

$$\tau_\infty = \int_0^\infty dt' \kappa_{12} \sin\Theta \approx \kappa\omega\nu^{1/2} \tag{2.51}$$

where κ is the average value of the overlap integral. The magnitude of nonlinear effects is governed by the parameter

$$P\tau_\infty \approx \frac{4\pi a_s N}{L_{BEC}} \kappa\omega\nu^{1/2}. \tag{2.52}$$

The condition $P\tau_\infty << 1$, allowing neglect of nonlinear effects, imposes restrictions on the total number of atoms in the condensate or the maximum value of adiabaticity.

Nonlinear recombination of two modes for the case when the phase shift $\Delta\phi \approx \pi$, has been previously discussed in [42] for arbitrary values of the effective nonlinearity $P\tau_\infty$. In the limit $\Delta\phi \approx \pi$ and $P\tau_\infty > 1$, the nonlinear recombination can be characterized as an instability resulting in an exponential amplification of the weak ground state mode $(0,0)_s \rightarrow (0,0)_u$ by the strong higher-frequency mode $(0,0)_a \rightarrow$

$(1,0)_u$. The instability growth rate γ was found to be given by the relation

$$\gamma^2 = \left[-\Delta\omega + P(\kappa_{12} - \kappa_{22})\right]\left[\Delta\omega + P(\kappa_{22} - 3\kappa_{12})\right]. \tag{2.53}$$

It implicitly depends on the control parameter $\Delta\beta_x$ which determines the shape of the guiding potential and, consequently, both the frequency difference $\Delta\omega$ and the overlap integrals κ_{ij}.

The growth rate γ is plotted in Fig. (2.8) versus the control parameter $\Delta\beta_x$ for the potential (2.20) with $\epsilon = 10^{-2}$ and $\beta_z = 10^{-1}$. The solid curves correspond to the above-discussed case when the recombined condensate is localized in the upper guide, i.e., the output wave function is a linear combination of the ground and excited state of the upper guide. This situation may be realized in an interferometric configuration where the cloud is initially launched into the lowest mode of the upper guide, split into the left and the right guides, acquires relative phase shift and again recombines in the upper guide. The dashed curve corresponds to the situation when the cloud is initially launched into the lowest mode of the lower guide. Results for both cases are quite similar.

To gain further insight into the nature of this instability, we have analyzed the excitation spectrum of the condensate in the framework of the full Gross-Pitaevskii equation. The analysis has been carried out for a one-transverse-dimensional problem

$$i\frac{\partial}{\partial t}\psi(x,t) = \left[-\frac{1}{2}\frac{\partial^2}{\partial x^2} + U(x,\beta) + P|\psi|^2\right]\psi(x,t), \tag{2.54}$$

that is computationally simpler, but exhibits the same physics.

The model potential U was specified as

$$U(x) = \sqrt{1 + (\beta - x^2/2)^2}. \tag{2.55}$$

Figure 2.8: The growth rate as a function of $\Delta\beta_x$ for $P = 0.1$ and 0.5.

The steady-state ground state ψ_0 is given by the relation

$$\mu\psi_0 = \left[-\frac{1}{2}\frac{\partial^2}{\partial x^2} + U(x) + P|\psi_0|^2\right]\psi_0. \tag{2.56}$$

For $\Delta\phi \approx \pi$, ψ_o is the lowest weakly nonlinear antisymmetric mode of the potential (2.55).

Representing $\psi(x,t)$ in the form

$$\psi(x,t) = \exp(-i\mu t)[\psi_0(x) + \delta(x,t)] \tag{2.57}$$

and linearizing Eq. (2.55) with respect to $\delta(x,t)$, yields the set of equations for the real functions $u = \mathrm{Re}(\delta)$ and $v = \mathrm{Im}(\delta)$:

$$\begin{aligned} \frac{\partial}{\partial t}u &= -\left[\frac{1}{2}\frac{d}{dx^2} + W^+\right]v, \\ \frac{\partial}{\partial t}v &= -\left[\frac{1}{2}\frac{d}{dx^2} + W^-\right]u, \end{aligned} \tag{2.58}$$

where

$$W^{\pm} = \mu - U - P\psi_0^2(2 \pm 1). \tag{2.59}$$

Since the coefficients in Eq. (2.58) are time-independent, one can use the anzatz $u, v \propto \exp(-i\lambda t)$, resulting in closed-form equations for u and v:

$$\left[\frac{1}{2}\frac{d}{dx^2} + W^+\right]\left[\frac{1}{2}\frac{d}{dx^2} + W^-\right]u = \lambda^2 u, \tag{2.60}$$

and

$$\left[\frac{1}{2}\frac{d}{dx^2} + W^-\right]\left[\frac{1}{2}\frac{d}{dx^2} + W^+\right]v = \lambda^2 v. \tag{2.61}$$

Solution of Eqs. (2.56), (2.60), and (2.61) yields the excitation spectrum of the condensate, i.e., the set of eigenfrequencies λ. Imaginary values of λ correspond to exponentially growing perturbations.

Figure 2.9 shows λ as a function of the control parameter β. The dotted lines correspond to the real part of λ, and the solid line is the imaginary part of λ. Figure 2.9 demonstrates that one of the excitation modes of the condensate becomes unstable in accordance with the results of the previous analysis summarized by Fig. 2.8. The most interesting feature in Fig.2.9 is the behavior of the lowest eigenfrequency as a function of the control parameter β. The eigenmode corresponding to this frequency is the lowest-lying symmetric perturbation of the antisymmetric ground state. As β increases, the eigenfrequency decreases and eventually reaches zero, i.e., the mode becomes soft. Further increase in β makes this mode unstable. The physics of the instability is therefore associated with the excitation of a soft mode.

Figure 2.9: Excitation spectrum of the condensate versus control parameter β for $P = 0.1$

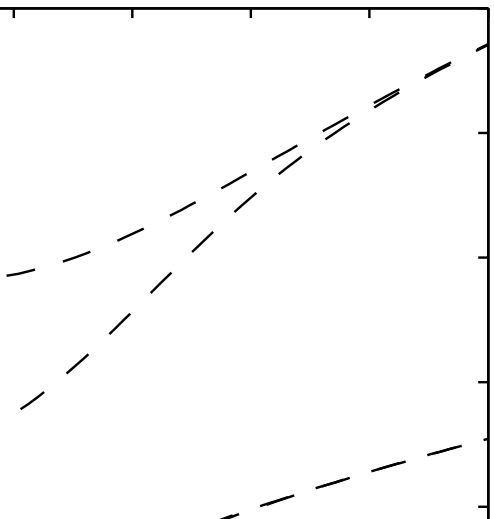

Chapter 3

Analysis of the BEC accelerometer

The primary use of a BEC-based trapped atom interferometer is to measure differences in local potential energy. Differences in local potential can have many causes including differences in gravity, or motion (accelerations and rotations) of the device. The interferometer cycle starts with a condensate initially held in the lowest mode of a single-well atomic trap. By external means, the single-well trap is split symmetrically into a double-well trap thus splitting the condensate into two. Differences in local potential energy between two separated wells introduce an accumulated phase shift between the wave functions of the two condensates. After this evolution, the two wells are recombined into a single well, thus recombining the two condensates. The populations of the two lowest energy eigenmodes of the trapping potential are measured. Assuming that the phase shift is accumulated only when the two potential wells are far apart, the populations of the two lowest modes of the recombined single-well trap are given by the expressions $P_1 = \cos^2\varphi$ and $P_2 = \sin^2\varphi$ [55, 56]. Here P_1 is the population of the first mode (the lowest mode of the recombined trap), P_2 is the population of the second mode (the first excited mode of the trap) and φ is the accumulated phase shift.

In this chapter, we analyze the operation of a trapped-atom accelerometer. Acceleration of this device is responsible for the differences in local potential between the arms of the interferometer. We introduce an analytic model to describe the dynamics of the splitting and recombination of the atomic cloud which is more realistic as compared to previous treatments. Namely, we explicitly account for the fact that acceleration is present not only when the two potential wells are far apart so that the tunneling between them is suppressed, but during the whole operation cycle including the separation and the recombination stages. The populations of the lowest two modes after the recombination are found as functions of the accumulated phase shift and the separation and recombination rates. A decrease in the visibility

of the interference fringes is shown to occur when the potential wells are separated or recombined too slowly or, equivalently, the acceleration is too large. Estimates are given for the operation range of the accelerometer.

3.1 Formulation

Influence of nonlinearity on the dynamics of splitting and recombination of the condensate was analyzed in [42, 41]. To simplify further analysis and to concentrate on effects due to the acceleration alone, we will assume that the nonlinearity is small enough to be neglected and describe the evolution of the atomic cloud by the equation

$$i\hbar\frac{\partial}{\partial x}\psi(x,t) = \left[-\frac{\hbar^2}{2m}\frac{\partial^2}{\partial x^2} + V(x,t) + mxa\right]\psi, \tag{3.1}$$

where a is the acceleration of the interferometer. Conditions that are necessary for this approximation were discussed in [41].

Solution of Eq. (3.1) can be sought as a linear superposition of eigenmodes $\phi_n(x,t)$ of the Hamiltonian of Eq. (3.1) with $a = 0$

$$\psi(x,t) = \sum_n A_n\phi_n(x,t), \tag{3.2}$$

where the eigenmodes ϕ_n and their eigenfrequencies ω_n are solutions of the eigenvalue problem

$$\hbar\omega_n\phi_n = \left[-\frac{\hbar^2}{2m}\frac{\partial^2}{\partial x^2} + V(x,t)\right]\phi_n \tag{3.3}$$

(time enters Eq. (3.3) as a parameter). When the potential $V(x,t)$ is a double-well potential with two wells far apart, all eigenmodes become pairwise-degenerate. This degeneracy is due to the fact that the potential V is symmetric in x and thus the left and the right potential wells are mirror reflections of each other. A member of a

pair with slightly lower (higher) energy is the symmetric (antisymmetric) eigenmode of the whole potential V. A sum or difference of these two modes is an eigenmode of the left or the right potential well.

Substituting Eq. (3.2) into Eq. (3.1) results in a set of coupled equations for the modal decomposition coefficients A_n of the form

$$i\frac{d}{dt}A_n = \omega_n A_n + \sum_m f_{nm}A_m - i\sum_m A_m g_{nm}, \tag{3.4}$$

where the overlap integrals f_{nm} and g_{nm} are given by the relations

$$f_{nm} = \frac{ma}{\hbar}\int \phi_n x \phi_m dx \tag{3.5}$$

and

$$g_{nm} = \int \phi_n \frac{\partial}{\partial t}\phi_m. \tag{3.6}$$

In the following we will assume that the characteristic time of change of the potential T_0 defined as the time it takes to split a single wave function into two separated by their characteristic size, is much larger than the inverse of the characteristic frequency difference ω_0 between the eigenmodes of a single-well trap

$$\omega_0 T_0 \gg 1. \tag{3.7}$$

Condition (3.7) allows one to neglect the overlap integrals g_{mn} in Eq. (3.1). In practice the product $\omega_0 T_0$ should be larger than about ten [56, 41].

Additionally we will assume that

$$\hbar\omega_0 \gg ma(\hbar/m\omega_0)^{1/2}. \tag{3.8}$$

Inequality (3.8) means that coupling between the eigenmodes of a single-well trap due to the acceleration can be neglected. Since the condensate starts in the lowest mode ϕ_1 of the single-well trap, we can limit ourselves to a two-mode approximation and keep only ϕ_1 and ϕ_2 in Eq. (3.2).

Redefining amplitudes $A_{1,2}$ as

$$A_{1,2} \to A_{1,2} \exp\left[-(i/2)\int^t dt'(\omega_1+\omega_2)\right], \tag{3.9}$$

we reduce the system of coupled equations Eq. (3.4) to the form

$$\begin{aligned} i\frac{d}{dt}A_1 &= -\frac{\Delta\omega(t)}{2}A_1 + f(t)A_2, \\ i\frac{d}{dt}A_2 &= \frac{\Delta\omega(t)}{2}A_2 + f(t)A_1, \end{aligned} \tag{3.10}$$

where $f = f_{12}$ and $\Delta\omega = \omega_2 - \omega_1$.

Equations (3.10) can be rewritten as a single equation for either A_1 or A_2 of the form

$$\ddot{A}_{1,2} - \frac{\dot{f}}{f}\dot{A}_{1,2} + \left[\left(\frac{\Delta\omega}{2}\right)^2 + f^2 - i\frac{\pm\dot{\Delta\omega}}{2} + i\frac{\dot{f}}{f} \pm \frac{\Delta\omega}{2}\right] A_{1,2} = 0, \tag{3.11}$$

where the plus (minus) is for A_1 (A_2) and the dots denote time derivatives.

Local spatial eigenmodes $\phi_\pm$ of Eq. (3.10) calculated taking time as a parameter in $\Delta\omega(t)$ and $f(t)$, are given by the expressions

$$\begin{aligned} \phi_- &= \cos\frac{\Theta}{2}\phi_1 - \sin\frac{\Theta}{2}\phi_2, \\ \phi_+ &= \sin\frac{\Theta}{2}\phi_1 + \cos\frac{\Theta}{2}\phi_2, \end{aligned} \tag{3.12}$$

where $\tan\Theta = 2f/\Delta\omega$. The corresponding eigenfrequencies are

$$\omega_{\mp} = \mp\sqrt{(\Delta\omega)^2/4 + f^2}. \tag{3.13}$$

For a single-well trap $\Delta\omega >> f$ and $\Theta \to 0$, so the eigenmodes are $\phi_- = \phi_1$ and $\phi_+ = \phi_2$, the lowest symmetric and antisymmetric modes of the trapping potential. For a double-well trap with two potential wells far apart, $\Delta\omega \to 0$ and $\Theta \to \pi/2$ and the eigenmodes (3.12) become $\phi_- = (\phi_1 - \phi_2)/\sqrt{2}$ and $\phi_+ = (\phi_1 + \phi_2)/\sqrt{2}$. The eigenmodes $\phi_{\mp}$ in this limiting case correspond to the condensate being completely localized in either the lower-energy (left) or the higher-energy (right) potential wells, respectively. A schematic plot of the eigenfrequencies Eq. (3.13) versus the distance between the wells and the shape of local eigenmodes Eq. (3.12) in two limiting cases are shown in Fig. 3.1.

If the potential wells are split and recombined completely adiabatically, eigenmodes (3.12) become solutions of Eqs. (3.10). A typical cycle starts with the BEC in the lowest mode of a single-well trap corresponding to the leftmost part of the lower curve in Fig. 3.1. If the condensate is split adiabatically slowly, it will follow the lower curve and therefore will end up completely localized in the left (lower-energy) potential well. To complete the interferometer cycle, the two wells are brought slowly back and recombined. The condensate follows the lower curve back and ends up in the lowest mode of the single-well recombined trap. Since there was no condensate in the higher-energy well, no interference fringes will be observed.

If, however, the wells are separated and recombined relatively fast, not giving the condensate time to follow the lower curve in Fig. 3.1, half of the condensate will pass through the avoided crossing (the region inside the dashed box). Now when the wells are far apart, half of the condensate will be in the left well and half in the

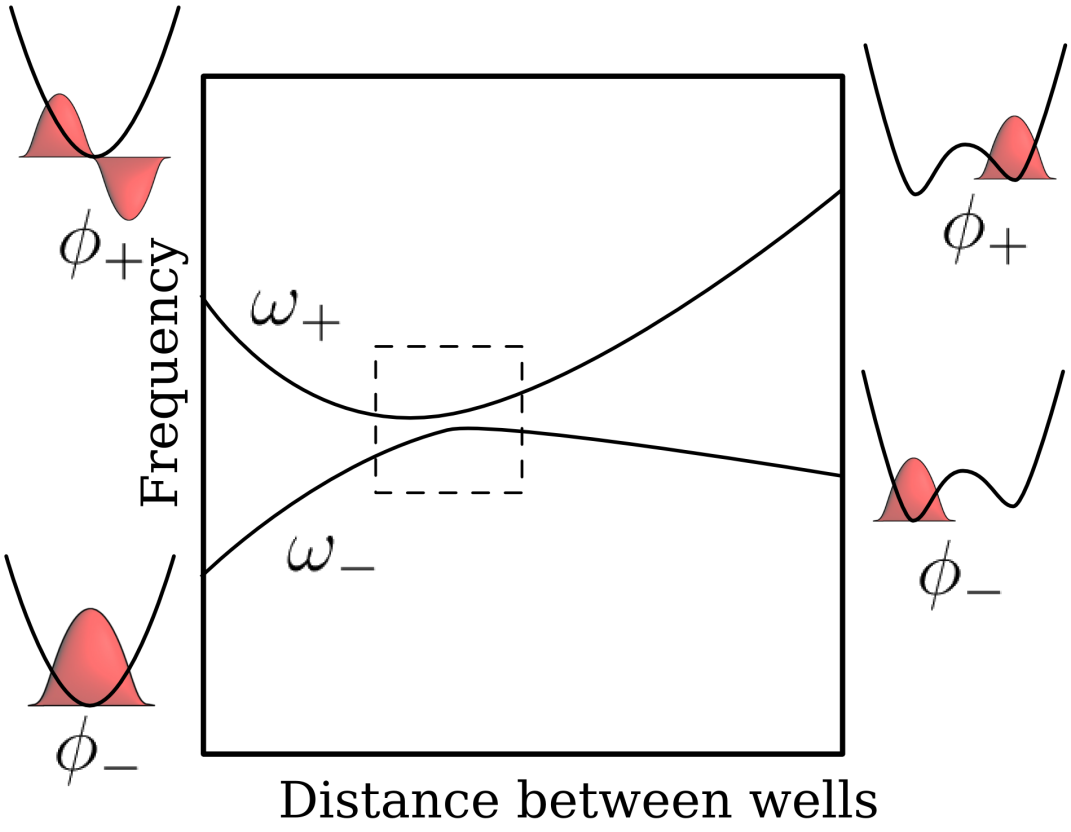

Figure 3.1: The eigenfrequencies of the local modes as functions of the distance between the two wells of a double-well trap. An avoided crossing is shown inside the dashed box. Two corresponding eigenmodes of a single-well potential are shown on the left. The eigenmodes in the limit when the wells are far apart, are shown on the right. These eigenmodes are localized in either the left or right potential wells.

right well. The potential energies of the two wells are different and, therefore, the two parts of the condensate will acquire a relative phase shift. If the recombination stage is also relatively fast, interference fringes will be observed after recombination.

The physics of traversing the avoided crossing of Fig. 3.1 is very similar to the Landau-Zener effect [57, 58, 59].

3.2 Analytic model

For a single-well potential, $\Delta\omega >> f$ in Eq. (3.10), modes A_1 and A_2 are decoupled and evolve independently without energy exchange. When the two wells are far apart, $\Delta\omega$ becomes exponentially small and f grows as a linear function of the distance between the wells. In this case $\Delta\omega << f$, and solution of Eq. (3.10) is again trivial. Nontrivial evolution of the modal amplitudes A_1 and A_2 takes place in the vicinity of the avoided crossing (the region inside the dashed box in Fig. 3.1), when f and $\Delta\omega$ are of the same order of magnitude: $\Delta\omega \approx f$. To analyze this evolution in the framework of an analytically-solvable model, the frequency difference $\Delta\omega$ near the avoided crossing will be approximated by a linear function of time and f will be held constant since it changes much slower than $\Delta\omega$.

Specifically, we assume that in the vicinity of the avoided crossing

$$\Delta\omega(t) = \begin{cases} -(t/T_s)f, & t < 0 \\ 0, & t > 0 \end{cases} \tag{3.14}$$

at the separation stage and

$$\Delta\omega(t) = \begin{cases} 0, & t < 0, \\ (t/T_r)f, & t > 0 \end{cases} \tag{3.15}$$

at the recombination stage.

Using Eq. (3.14) in Eq. (3.11), we get

$$\frac{d^2}{dz^2}A_1 + \left[-ip + \frac{1}{2} - \frac{z^2}{4}\right] A_1 = 0, \tag{3.16}$$

where $z = (f/T_s)^{1/2} e^{i\pi/4} t$ and $p = fT_s$.

Using Eq. (3.4) to find A_2 yields

$$A_2 = \frac{e^{i3\pi/4}}{\sqrt{p}} \left[\frac{d}{dz}A_1 + \frac{z}{2}A_1\right]. \tag{3.17}$$

Solutions of Eq. (3.16) and (3.17) can be found in terms of parabolic cylinder functions [60] and are of the form

$$\begin{aligned} A_1 &= \alpha D_{-ip}(z) + \beta D_{-ip}(-z), \\ A_2 &= \frac{e^{i3\pi/4}}{\sqrt{p}} \left\{\alpha \left[z D_{-ip}(z) - D_{-ip+1}(z)\right] + \beta \left[z D_{-ip}(-z) + D_{-ip+1}(-z)\right]\right\}, \end{aligned} \tag{3.18}$$

where α and β are arbitrary constants.

Imposing asymptotic boundary conditions $|A_1|^2 \to 1$ and $|A_2|^2 \to 0$ as $t \to -\infty$ yields $\alpha = 0$ and $\beta = \exp(-\pi p/4)$. Modal amplitudes at the end of the splitting stage ($t = 0 \to z = 0$) are given by the relations

$$\begin{aligned} A_1(0) &= 2^{-ip/2} e^{-\pi p/4} \frac{\sqrt{\pi}}{\Gamma\left(\frac{1}{2} + \frac{ip}{2}\right)}, \\ A_2(0) &= \sqrt{\frac{2}{p}} 2^{-ip/2} e^{-\pi p/4 + i3\pi/4} \frac{\sqrt{\pi}}{\Gamma\left(\frac{ip}{2}\right)}, \end{aligned} \tag{3.19}$$

where Γ is the gamma function.

After splitting the $\Delta\omega$ in Eq. (3.10) is negligible and can be discarded. The parameter f, on the other hand, increases with an increase in the separation between

the wells. Equation (3.10) now reduces to the form

$$\begin{aligned} \frac{d}{dt}A_1 &= -if(t)A_2, \\ \frac{d}{dt}A_2 &= -if(t)A_1, \end{aligned} \tag{3.20}$$

and yield

$$\begin{aligned} A_1(t) &= A_1(0)\cos\varphi - iA_2(0)\sin\varphi, \\ A_2(t) &= A_2(0)\cos\varphi - iA_1(0)\sin\varphi, \end{aligned} \tag{3.21}$$

where $\varphi = \int^t f(t')dt'$ is the accumulated phase shift between the left and the right wells.

Substituting Eq. (3.19) into Eq. (3.21) yields the modal amplitudes immediately before the recombination stage

$$\begin{aligned} A_1 &= \sqrt{\pi}e^{-ip/2-\pi p/4}\left[\frac{\cos\varphi}{\Gamma\left(\frac{1}{2}+\frac{ip}{2}\right)} + e^{i\pi/4}\sqrt{\frac{2}{p}}\frac{\sin\varphi}{\Gamma\left(\frac{ip}{2}\right)}\right], \\ A_2 &= \sqrt{\pi}e^{-ip/2-\pi p/4}\left[-e^{-i\pi/4}\sqrt{\frac{2}{p}}\frac{\cos\varphi}{\Gamma\left(\frac{ip}{2}\right)} - i\frac{\sin\varphi}{\Gamma\left(\frac{1}{2}+\frac{ip}{2}\right)}\right]. \end{aligned} \tag{3.22}$$

At the recombination stage it is more convenient to work with the equation for A_2

$$\frac{d^2}{dz}A_2 + \left[-ip' + \frac{1}{2} - \frac{z^2}{4}\right]A_2 = 0, \tag{3.23}$$

where $z = (f/T_r)^{1/2}e^{i\pi/4}t$ and $p' = fT_r$ (see Eq. (3.15)). Once again, the solutions can be written in terms of parabolic cylinder functions as

$$A_1(z) = \frac{e^{i3\pi/4}}{\sqrt{p'}}\left\{\alpha'\left[zD_{-ip'}(z) - D_{-ip'+1}(z)\right] + \beta'\left[zD_{-ip'}(-z) + D_{-ip'+1}(-z)\right]\right\},$$

$$A_2(z) \;=\; \alpha' D_{-ip'}(z) + \beta' D_{-ip'}(-z). \tag{3.24}$$

Coefficients α' and β' are found by matching Eq. (3.24) at $z = 0$ with Eq. (3.22) and turn out to be

$$\begin{aligned}
\alpha' &= \frac{1}{2} 2^{i\frac{p-p'}{2}} e^{-\pi p/4} \left[\cos\varphi \left(\sqrt{\frac{p'}{2}} e^{i\pi/4} \frac{\Gamma\left(\frac{ip'}{2}\right)}{\Gamma\left(\frac{1}{2}+\frac{ip}{2}\right)} - \sqrt{\frac{2}{p}} e^{-i\pi/4} \frac{\Gamma\left(\frac{1}{2}+\frac{ip'}{2}\right)}{\Gamma\left(\frac{ip}{2}\right)} \right), \right. \\
&+ \left. \sin\varphi \left(i\sqrt{\frac{p'}{p}} \frac{\Gamma\left(\frac{ip'}{2}\right)}{\Gamma\left(\frac{ip}{2}\right)} - i \frac{\Gamma\left(\frac{1}{2}+\frac{ip'}{2}\right)}{\Gamma\left(\frac{1}{2}+\frac{ip}{2}\right)} \right) \right], \\
\beta' &= \frac{1}{2} 2^{i\frac{p-p'}{2}} e^{-\pi p/4} \left[\cos\varphi \left(-\sqrt{\frac{p'}{2}} e^{i\pi/4} \frac{\Gamma\left(\frac{ip'}{2}\right)}{\Gamma\left(\frac{1}{2}+\frac{ip}{2}\right)} - \sqrt{\frac{2}{p}} e^{-i\pi/4} \frac{\Gamma\left(\frac{1}{2}+\frac{ip'}{2}\right)}{\Gamma\left(\frac{ip}{2}\right)} \right) \right. \\
&+ \left. \sin\varphi \left(-i\sqrt{\frac{p'}{p}} \frac{\Gamma\left(\frac{ip'}{2}\right)}{\Gamma\left(\frac{ip}{2}\right)} - i \frac{\Gamma\left(\frac{1}{2}+\frac{ip'}{2}\right)}{\Gamma\left(\frac{1}{2}+\frac{ip}{2}\right)} \right) \right].
\end{aligned} \tag{3.25}$$

Modal amplitudes after the completion of the recombination stage are obtained by taking the limit $t \to \infty$ in Eq. (3.24) resulting in

$$\begin{aligned}
A_{1,fin} &= \beta' \sqrt{\frac{2\pi}{p'}} \frac{1}{\Gamma(ip')} e^{-\pi p'/4}, \\
A_{2,fin} &= e^{-\pi p'/4} \left(\alpha' e^{\pi p'/2} + \beta' e^{-\pi p'/2} \right).
\end{aligned} \tag{3.26}$$

3.3 Discussion

Equations (3.25) and (3.26) contain all the information necessary to calculate the populations $P_{1(2)} = |A_{1(2),fin}|^2$ of the two lowest modes of the condensate after the recombination as functions of the separation time T_s ($p = fT_s$), recombination time T_r ($p' = fT_r$), and the accumulated phase shift φ. To gain insight into the general solution given by Eqs. (3.25) and (3.26), let us first discuss the modal amplitudes of the condensate after the separation stage, which are given by Eq. (3.19). Once the

potential wells are far apart, it is more convenient to work not with the eigenmodes ϕ_1 and ϕ_2 of the whole potential V, but with the eigenmodes ϕ_l and ϕ_r of the left and right potential wells

$$\begin{aligned} \phi_l &= \frac{1}{\sqrt{2}}(\phi_1 - \phi_2), \\ \phi_r &= \frac{1}{\sqrt{2}}(\phi_1 + \phi_2). \end{aligned} \tag{3.27}$$

Populations of the left and the right wells are given by the relations

$$\begin{aligned} P_l &= (1/2)|A_1(0) - A_2(0)|^2, \\ P_r &= (1/2)|A_1(0) + A_2(0)|^2. \end{aligned} \tag{3.28}$$

In the limit of slow separation or large acceleration, $p \gg 1$, Eqs. (3.28) and (3.19) yield

$$\begin{aligned} P_l &= 1 - \frac{1}{64p^2}, \\ P_r &= \frac{1}{64p^2}. \end{aligned} \tag{3.29}$$

Almost all the condensate ends up in the lower-energy (left) potential well after splitting. One should expect a considerable reduction in the fringe visibility after recombination in this limit.

In the opposite limit of fast separation or small acceleration, $p \ll 1$, the populations of the left and the right wells are given by the expressions

$$\begin{aligned} P_l &= \frac{1}{2}(1 + \sqrt{\pi p}), \\ P_r &= \frac{1}{2}(1 - \sqrt{\pi p}). \end{aligned} \tag{3.30}$$

The condensate in this limit is split almost equally between the left and right potential wells with only slightly larger population in the lower-energy well. If the recombination is also fast ($p' \ll 1$), one should expect populations of the ground and the first excited modes of the trap after the recombination to be given by the standard expressions $P_1 = \cos^2\varphi$ and $P_2 = \sin^2\varphi$.

Taking the limit $p \ll 1$ and $p' \ll 1$ in Eqs. (3.25) and (3.26) (fast separation and recombination or small acceleration), we get for the populations of the two lowest modes of the trap after the recombination:

$$\begin{aligned} P_1 &= \cos^2\varphi - \cos\varphi \sin\varphi(\sqrt{\pi p} + \sqrt{\pi p'}), \\ P_2 &= \sin^2\varphi + \cos\varphi \sin\varphi(\sqrt{\pi p} + \sqrt{\pi p'}). \end{aligned} \tag{3.31}$$

Equations (3.31) demonstrate that the populations of the ground and the first excited states of the recombined trap are indeed given by $\cos^2\varphi$ and $\sin^2\varphi$, respectively, with power-law corrections. In this limit, the visibility of the interference fringes remains close to unity. The corrections shift the interference pattern. The shift is due to the phase accumulated during the separation and recombination process.

Taking the opposite limit $p \gg 1$ and $p' \gg 1$ in Eqs. (3.25) and (3.26) (slow splitting and recombination or large acceleration) results in the expressions

$$\begin{aligned} P_1 &= 1 - \frac{1}{64}\left[\cos^2\varphi\left(\frac{1}{p} + \frac{1}{p'}\right) - \sin^2\varphi\left(\frac{1}{p} - \frac{1}{p'}\right)\right], \\ P_2 &= \frac{1}{64}\left[\cos^2\varphi\left(\frac{1}{p} + \frac{1}{p'}\right) - \sin^2\varphi\left(\frac{1}{p} - \frac{1}{p'}\right)\right]. \end{aligned} \tag{3.32}$$

Equations (3.32) show that $P_1 \approx 1$ and $P_2 \ll 1$, i.e., the recombined condensate predominantly populates the lowest mode of the trap independently of the accumulated phase shift. The visibility in the interference fringes is decreased, thus decreasing

the sensitivity of the interferometer.

The limit of fast separation and slow recombination, $p \ll 1$ and $p' \gg 1$ in Eqs. (3.25) and (3.26), results in the expressions

$$P_1 = \frac{1}{2}\left[1 - \frac{1}{2p'}\sin\varphi\cos\varphi\right],$$
$$P_2 = \frac{1}{2}\left[1 + \frac{1}{2p'}\sin\varphi\cos\varphi\right]. \tag{3.33}$$

The recombined condensate is almost equally split between the two modes with low sensitivity to the accumulated phase shift. Since $p \ll 1$, the condensate after the separation is equally split between the left and the right potential wells (cf. Eq. (3.30)) corresponding to two dispersion curves of Fig. 3.1. During the slow recombination stage, both parts of the atomic cloud follow the dispersion curves, resulting in equal populations of the ground and the first excited modes of the recombined trap.

The opposite limit of slow separation and fast recombination, $p \gg 1$ and $p' \ll 1$ in Eqs. (3.25) and (3.26), yields

$$P_1 = \frac{1}{2}\left[1 - \frac{1}{2p}\sin\varphi\cos\varphi\right],$$
$$P_2 = \frac{1}{2}\left[1 + \frac{1}{2p}\sin\varphi\cos\varphi\right]. \tag{3.34}$$

The recombined condensate is again almost equally split between the two modes independently of the accumulated phase shift. In this case, almost all the condensate after the separation is in the lower potential well (cf. Eq. (3.29)). During the fast recombination stage, the condensate does not have time to adjust to changes in the potential and remains in the lower half of the recombining well, resulting in an equal-weight superposition of the ground and the first excited modes of the recombined

single-well trap. .

To analyze the operation of the accelerometer for intermediate values of the splitting and recombination rates, we will specialize to the case when the splitting and the recombination rates are equal so that $T_s = T_r$ and $p = p'$. Equations (3.25) and (3.26) in this case can be considerably simplified and result in compact expressions

$$\begin{aligned} P_1 &= \cos^2\varphi(\cos^2\theta + e^{-2\pi p}\sin^2\theta) + \sin^2\varphi(1 - e^{-2\pi p}) \\ &+ 2\cos\varphi\sin\varphi e^{-\pi p}\sqrt{1 - e^{2\pi p}}, \\ P_2 &= \cos^2\varphi\sin^2\theta(1 - e^{-2\pi p}) + \sin^2\varphi e^{-2\pi p} \\ &- 2\sin\varphi\cos\varphi e^{-\pi p}\sqrt{1 - e^{-2\pi p}}, \end{aligned} \tag{3.35}$$

where the angle θ is determined by the equation

$$\theta = \frac{\pi}{4} + \arg\left[\Gamma\left(\frac{ip}{2}\right)\Gamma^{-1}\left(\frac{1}{2} + \frac{ip}{2}\right)\right]. \tag{3.36}$$

The population of the first excited mode P_2 evaluated using Eq. (3.35) and (3.36), is plotted in Fig. 3.2 versus the phase shift φ for several representative values of p. Figure 3.2 demonstrates that for small values of p, the population of the first excited mode as a function of the phase shift, changes from zero to one, i.e., the interference fringes have high visibility. As p becomes larger, the fringe visibility becomes smaller. This effect is due to the fact that the populations of the left and the right wells after the splitting are no longer equal; a larger and larger percentage of the condensate is localized in the lower-energy potential well. Additionally, the interference fringes shift. This shift is caused by the phase accumulated during the separation and recombination stages.

Figure 3.2: Population of the first excited mode $P_2 = |A_{2,fin}|^2$ after recombination as a function of the accumulated phase shift φ for several values of p.

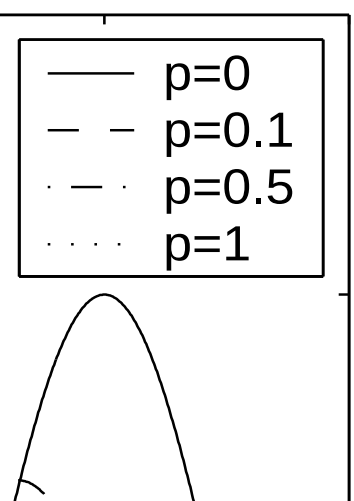

3.4 Estimates

Analysis of Sec. 3.3 shows that the preferable operation range of the accelerometer corresponds to $p = fT \ll 1$ assuming that the separation and recombination rates are of the same order of magnitude: $T_s \approx T_r \approx T$. To express this requirement in terms of physical parameters, we have to evaluate f and T in the vicinity of the avoided crossing.

The frequency difference between the ground and the first excited modes of a double-well trap $\Delta\omega$ as a function of separation l between the wells can be approximated by the expression

$$\Delta\omega = \omega_0 \exp(-\gamma l^2/d^2), \tag{3.37}$$

where ω_0 is the characteristic frequency of a single-well trap, $d = (\hbar\omega_0/m)^{1/2}$ is the characteristic size of the wave function of a single-well trap and γ is a dimensionless parameter of the order of one. The approximation (3.37) assumes that the height of the potential barrier between the wells is proportional to the interwell separation l.

The overlap integral f Eq. (3.5) in the limit $l \gg d$ can be approximated by the expression

$$f \approx \frac{am}{\hbar} l. \tag{3.38}$$

The avoided crossing corresponds to $\Delta\omega = f$ and, with logarithmic accuracy, one gets

$$\gamma \left(\frac{l}{d}\right)^2 \approx \ln \frac{\hbar\omega_0}{amd}. \tag{3.39}$$

The characteristic width of the avoided crossing region Δl, estimated by requiring that the relative change of $\Delta\omega$ be of the order of one, is given by the relation

$$\frac{\Delta l}{d} \approx \frac{1}{\gamma}\frac{d}{l}. \tag{3.40}$$

Since $\hbar\omega_0/amd \gg 1$ (see Eq. (3.8)), $l/d \gg 1$ and, consequently, $\Delta l/l \ll 1$. The approximation $f = \text{const}$ in the avoided crossing region is thus well justified.

The characteristic splitting or recombination time can be evaluated as $T = (\Delta l/d)T_0$, where T_0 is the characteristic time of change of the potential (see Eq. (3.7)). Using Eq. (3.40), one gets

$$T \approx \frac{1}{\gamma}\frac{d}{l}T_0. \tag{3.41}$$

The condition $fT \ll 1$, using Eqs. (3.38) and (3.41), can thus be expressed as

$$\frac{amd}{\gamma\hbar\omega_0}\omega_0 T_0 \ll 1. \tag{3.42}$$

For example, taking $\omega_0 T_0 = 10$, $\omega_0 = 2\pi \times 200\,\text{Hz}$, $m = 1.44 \times 10^{-25}\text{kg}$ (^{87}Rb), and $d = 0.7\mu\text{m}$, yields the upper limit on the acceleration $a \ll 10^{-2}\text{m/s}^2$.

In conclusion, we briefly discuss to which degree results of the preceding analysis depend on assumptions adopted in developing the analytic model of Sec. 3.2 ($\Delta\omega \propto t$, $f = \text{const}$). The main result of the paper predicting decrease in the visibility of the interference fringes and their shift caused by the acceleration, will remain valid for any other functional dependence of $\Delta\omega$ and f on time. Estimates of this section will also hold. Details of functional dependence of the population on the separation and recombination rates are model-dependent. For example, the populations of the wells after the separation in the limit $p \gg 1$ (Eq. (3.29)) in the framework of our model ($\Delta\omega \propto t$) are described by power-law corrections ($P_l \propto p^{-2}$). An exponential dependence of $\Delta\omega$ on time ($\Delta\omega \propto \exp(-t/T)$), according to our estimates, gives exponentially-small corrections ($P_l \propto \exp(-p)$).

Chapter 4

Cold atom splitter based on an asymmetric double-well potential

4.1 Introduction

In this chapter, we propose a new type of beam splitter. It uses quantum tunneling of atoms between two separated potential wells, reminiscent of an optical fiber splitter. To overcome self-trapping and increase the number of atoms that can be split, a time dependent anti-symmetric potential is introduced that breaks the symmetry of the potential wells and lowers the energy of one well with respect to the other. The condensate is prepared when the anti-symmetric potential is large such that all atoms are initially in the lower of the two wells. Then as a function of time, the anti-symmetric potential is turned off in such a way that the number of atoms found in each well is equal when the anti-symmetric potential is zero.

There are two physically different methods that can be used to increase the number of atoms that can be split. Both of these methods utilize the addition of an anti-symmetric potential to break the symmetry of the double well potential. In the first, the energy difference between the two wells is chosen to "cancel" the energy due to atom-atom interactions. The second method to split the atoms is to turn the anti-symmetric potential off more slowly so that the atoms remain in the lowest energy state of the asymmetric potential structure. We develop a theoretical model that describes the splitting of a condensate in the non-symmetric potential. We show that the first method of splitting is very fast but implies prior knowledge about the number of atoms to be split. The second method is slower but robust to variations in the number of atoms.

4.2 The Model (Second Quantization)

To describe the dynamics of the beamsplitter, we will make use of a two-mode model. Some aspects of the quantum dynamics of a Bose-Einstein condensate in

the framework of a two-mode model in both a symmetric and asymmetric double well potential have been previously discussed in [61] and [62]. A two-mode model has also been used to discuss the quantum noise limits of a atom interferometer [30]. Mean-field models employing a two-mode approximation have been used to describe the dynamics of atom interferometer [41].

For completeness and clarity, below we will briefly re-derive the Hamiltonian and equations of motion for the special case of a two-mode Bose-Einstein condensate in a symmetric double-well potential plus an anti-symmetric potential. In the second-quantization formalism, the Hamiltonian governing the dynamics of bosons interacting only by s-wave collisions is of the form [53]

$$\hat{H} = \int d^3r \hat{\Psi}^\dagger(\vec{r}) \left(-\frac{\hbar^2}{2m}\nabla^2 + V \right) \hat{\Psi}(\vec{r}) + \frac{U_0}{2} \int d^3r \hat{\Psi}^\dagger \hat{\Psi}^\dagger \hat{\Psi} \hat{\Psi} \tag{4.1}$$

where $\hat{\Psi}(\vec{r})$ is the field operator that obeys the usual Boson commutation relations $[\hat{\Psi}^\dagger(\vec{r}), \hat{\Psi}(\vec{r}')] = \delta(\vec{r} - \vec{r}')$, $U_0 = 4\pi\hbar^2 a_s/m$ characterizes the strength of interatomic interactions, a_s is the s-wave scattering length, and m is the atomic mass. The confining potential V is an asymmetric double well potential. It is assumed to be the sum of a static double well potential V_{DW}, that is symmetric about the y-z plane, and an explicitly time dependent controlling potential $V_C(t)$, that is anti-symmetric about the y-z plane.

The field operator will be decomposed into the eigenmodes of the symmetric double well potential

$$\hat{\Psi}(\vec{r}) = \sum_i \phi_i(\vec{r}) a_i, \tag{4.2}$$

where the operators a_i ($a_i^\dagger$) obey the usual bosonic commutation relations and remove (add) atoms to the ith mode ϕ_i. These modes are the solution to the eigenvalue

problem

$$\left(-\frac{\hbar^2}{2m}\nabla^2 + V_{DW}\right)\phi_i = \hbar\omega_i\phi_i, \tag{4.3}$$

with the energy eigenvalues $\hbar\omega_i$.

For simplicity, we assume that the confinement in the y-z plane sufficiently tight so that the atoms are in the lowest transverse mode. As a result, the modes of the double well potential have definite parity. The ground state ϕ_1 is an even function and the first excited state ϕ_2 is an odd function about the x axis. The modes localized in the left or right well with respect to the y-z plane are $\phi_L = (\phi_1 + \phi_2)/\sqrt{2}$ and $\phi_R = (\phi_1 - \phi_2)/\sqrt{2}$, respectively. According to our sigh convention both the ϕ_1 and ϕ_2 are positive in the left well. Associated with the modes that are localized in each well are the operators $a_R = (a_1 + a_2)/\sqrt{2}$ and $a_L = (a_1 - a_2)/\sqrt{2}$ that remove atoms from the respective well.

In the two-mode approximation, the atoms occupy only the lowest two modes of the double well potential. The field operator $\hat{\Psi}$ can be represented as

$$\hat{\Psi} = \phi_1 a_1 + \phi_2 a_2, \tag{4.4}$$

and, using this approximation, the Hamiltonian Eq. (4.1) reads

$$\hat{H} = -\frac{\hbar\Delta\omega}{2}(a_1^\dagger a_1 - a_2^\dagger a_2) + \frac{\hbar\eta}{2}(a_1^\dagger a_2 + a_2^\dagger a_1) + \frac{U_0\kappa}{2}(a_1^\dagger a_2 + a_2^\dagger a_1)^2, \tag{4.5}$$

where the tunneling frequency $\Delta\omega = \omega_2 - \omega_1$ is the difference in the frequency of the ground and the first excited state. The parameter $\eta = 2\hbar^{-1}\int d^3x \phi_1 V_C \phi_2$ determines the strength of the anti-symmetric potential and, because of our sign convention, is positive when the energy of the atoms in the right well is lower than those in the left. Finally, the two body interaction parameter $\kappa \approx \kappa_{1111} = \kappa_{1122} = \kappa_{2222}$, where

$\kappa_{ijkl} = \int d^3x \phi_i \phi_j \phi_k \phi_l$, determines the strength of the nonlinearity. Terms in the Hamiltonian that are functions of only the number operator $\hat{N} = a_1^\dagger a_1 + a_2^\dagger a_2$ have been dropped, since they commute with the Hamiltonian and have no effect on the dynamics.

The two-mode approximation is valid when both the nonlinearity and anti-symmetric contribution to the Hamiltonian are sufficiently weak, $U_0 \kappa N \ll \hbar\omega_{1,2}$ and $\eta \ll \omega_{1,2}$, where N is the total number of atoms in the condensate. The different overlap integrals κ are equal when $\omega_{1,2} \gg \Delta\omega$.

For the case of parabolic wells the overlap κ may be evaluated explicitly as

$$\kappa \approx \frac{1}{2} \frac{1}{(2\pi)^{3/2}} \frac{m\bar{\omega}}{\hbar} \frac{1}{\bar{a}}, \tag{4.6}$$

where $\bar{\omega} = (\omega_x \omega_y \omega_z)^{1/3}$ is the geometric average of the trap frequencies and $\bar{a} = \sqrt{\hbar/m\bar{\omega}}$ is the geometric average of the harmonic oscillator lengths .

The Hamiltonian given in Eq (4.5) may be recast in terms of the operators [61]

$$\begin{aligned} J_x &= -\frac{1}{2}(a_1^\dagger a_2 + a_1 a_2^\dagger), \\ J_y &= \frac{i}{2}(a_1^\dagger a_2 - a_1 a_2^\dagger), \\ J_z &= \frac{1}{2}(a_1^\dagger a_1 - a_2^\dagger a_2), \end{aligned}$$

that obey the usual angular momentum commutation relations. In the following, we will work in the basis of J_z, with the eigenvectors labeled $|j, m\rangle$ with $j = N/2$, where N the total number of atoms in the condensate.

In terms of the modes that are localized in the left and right wells, the angular

momentum operators are

$$\begin{aligned} J_x &= \frac{1}{2}(a_R^\dagger a_R - a_L^\dagger a_L), \\ J_y &= \frac{i}{2}(a_R^\dagger a_L - a_L^\dagger a_R), \\ J_z &= \frac{1}{2}(a_L^\dagger a_R + a_R^\dagger a_L). \end{aligned}$$

From the above relations it is clear that J_x is the operator that measures half the difference in the number of atoms in the right and left wells, J_z measures half the difference in the number of atoms in the ground and first excited state, and J_y is associated with the momentum of the atoms in each of the wells [61]. Finally following [62], the average phase shift between the atoms in the left and right wells may be defined as $\tan(\phi) = \langle J_y \rangle / \langle J_z \rangle$.

In terms of the angular momentum operators, the Hamiltonian Eq. (4.5) can be written in the dimensionless form

$$\hat{H} = -J_z - \chi(t) J_x + \frac{P}{N} J_x^2, \tag{4.7}$$

where the energy is measured in units of $\hbar\Delta\omega$ and time in units of $1/\Delta\omega$. The nonlinearity parameter P is defined by the relation

$$P = 2\frac{U_0 \kappa N}{\hbar \Delta\omega} \approx \sqrt{\frac{2}{\pi}} \frac{a_s}{\bar{a}} \frac{\bar{\omega}}{\Delta\omega} N, \tag{4.8}$$

and the anti-symmetric part of the potential enters as $\chi(t) = \eta(t)/\Delta\omega$. Hamiltonian (4.7) has been previously used in [62] to discuss interference effects in a stationary asymmetric double well potential. The conditions of applicability of the Hamiltonian (4.7) are $P \ll \omega_{1,2}/\Delta\omega$ and $\chi \ll \omega_{1,2}/\Delta\omega$.

The Heisenberg equations of motion for the angular momentum operators J_i are

$$\begin{aligned}
\frac{d}{dt}J_x &= J_y, \\
\frac{d}{dt}J_y &= -J_x + \chi J_z - \frac{P}{N}(J_x J_z + J_z J_x), \\
\frac{d}{dt}J_z &= -\chi J_y + \frac{P}{N}(J_x J_y + J_y J_x).
\end{aligned} \tag{4.9}$$

In the limit of large number of atoms $N \gg 1$, we may make the mean-field approximation $\langle J_i J_j \rangle \approx \langle J_i \rangle \langle J_j \rangle$ for any i,j. The equations of motion for the expectation values of the angular momentum operators, in the mean-field limit, become

$$\begin{aligned}
\frac{d}{dt}S_x &= S_y, \\
\frac{d}{dt}S_y &= -S_x + (\chi - 2PS_x)S_z, \\
\frac{d}{dt}S_z &= -(\chi - 2PS_x)S_y,
\end{aligned} \tag{4.10}$$

where $S_i = \langle J_i \rangle / N$, $i = \mathrm{x}, \mathrm{y}, \mathrm{z}$.

4.3 The Model (Mean-Field)

To describe the dynamics of the beamsplitter, we will make use of a two-mode model. Some aspects of the dynamics of a Bose-Einstein condensate in the framework of a two-mode model in both a symmetric and asymmetric double well potential have been previously discussed in [61] and [62]. A two-mode model has also been used to discuss the quantum noise limits of a atom interferometer [30]. Mean-field models employing a two-mode approximation have been used to describe the dynamics of atom interferometer [41].

For completeness and clarity, below we will briefly re-derive the equations of

motion for the special case of a two-mode Bose-Einstein condensate in a symmetric double-well potential plus an anti-symmetric potential. In the mean-field limit, the dynamics of a Bose-Einstein condensate is governed by the Gross-Pitaveskii equation [53]

$$i\hbar\frac{\partial}{\partial t}\Psi = \left(-\frac{\hbar^2}{2m}\nabla^2 + V + U_0 N|\Psi|^2\right)\Psi \tag{4.11}$$

where $\Psi(\vec{r})$ is the wave-function of the condensate that is normalized to unity, N is the total number of atoms in the condensate, $U_0 = 4\pi\hbar^2 a_s/m$ characterizes the strength of interatomic interactions, a_s is the s-wave scattering length, and m is the atomic mass. The confining potential V is an asymmetric double well potential. It is assumed to be the sum of a static double well potential V_{DW}, that is symmetric about the y-z plane, and an explicitly time dependent controlling potential $V_C(t)$, that is anti-symmetric about the y-z plane.

The wave function will be decomposed into the eigenmodes of the static symmetric double well potential

$$\Psi(\vec{r}) = \sum_i \phi_i(\vec{r})a_i, \tag{4.12}$$

where the complex function a_i is the amplitude of the atoms in the ith mode ϕ_i. These modes are the solution to the eigenvalue problem

$$\left(-\frac{\hbar^2}{2m}\nabla^2 + V_{DW}\right)\phi_i = \hbar\omega_i\phi_i, \tag{4.13}$$

with the energy eigenvalues $\hbar\omega_i$.

For simplicity, we assume that the confinement in the y-z plane sufficiently tight so that the atoms are in the lowest transverse mode. As a result, the modes of the double well potential have definite parity. The ground state ϕ_1 is an even function

and the first excited state ϕ_2 is an odd function about the x axis. The modes localized in the left or right well with respect to the y-z plane are $\phi_L = (\phi_1 + \phi_2)/\sqrt{2}$ and $\phi_R = (\phi_1 - \phi_2)/\sqrt{2}$, respectively. According to our sigh convention both the ϕ_1 and ϕ_2 are positive in the left well. Associated with the modes that are localized in each well are the amplitudes $a_R = (a_1 + a_2)/\sqrt{2}$ and $a_L = (a_1 - a_2)/\sqrt{2}$.

In the two-mode approximation, the atoms occupy only the lowest two modes of the double well potential. The wave function Ψ can be represented as

$$\Psi = (\phi_1 a_1 + \phi_2 a_2) e^{-i(\omega_1+\omega_2)t/2}, \tag{4.14}$$

and, using this approximation, the equations of motion for the modal amplitudes are

$$\begin{aligned} i\frac{d}{dt}a_1 &= -\frac{\Delta\omega}{2}a_1 + \frac{\eta}{2}a_2 \\ &+ \frac{U_0 N\kappa}{\hbar}\left(|a_1|^2 a_1 + 2|a_2|^2 a_1 + a_1^* a_2^2\right) \qquad (4.15) \\ i\frac{d}{dt}a_2 &= \frac{\Delta\omega}{2}a_2 + \frac{\eta}{2}a_1 \\ &+ \frac{U_0 N\kappa}{\hbar}\left(|a_2|^2 a_2 + 2|a_1|^2 a_2 + a_1^2 a_2^*\right), \qquad (4.16) \end{aligned}$$

where the tunneling frequency $\Delta\omega = \omega_2 - \omega_1$ is the difference in the frequency of the ground and the first excited state. The parameter $\eta = 2\hbar^{-1}\int d^3x \phi_1 V_C \phi_2$ determines the strength of the anti-symmetric potential and, because of our sign convention, is positive when the energy of the atoms in the right well is lower than those in the left. Finally, the two body interaction parameter $\kappa \approx \kappa_{1111} = \kappa_{1122} = \kappa_{2222}$, where $\kappa_{ijkl} = \int d^3x \phi_i \phi_j \phi_k \phi_l$, determines the strength of the nonlinearity.

The two-mode approximation is valid when both the nonlinearity and anti-symmetric contribution to the Hamiltonian are sufficiently weak, $U_0\kappa N \ll \hbar\omega_{1,2}$

and $\eta \ll \omega_{1,2}$, where N is the total number of atoms in the condensate. The different overlap integrals κ are equal when $\omega_{1,2} \gg \Delta\omega$.

For the case of parabolic wells the overlap κ may be evaluated explicitly as

$$\kappa \approx \frac{1}{2}\frac{1}{(2\pi)^{3/2}}\frac{m\bar{\omega}}{\hbar}\frac{1}{\bar{a}}, \tag{4.17}$$

where $\bar{\omega} = (\omega_x\omega_y\omega_z)^{1/3}$ is the geometric average of the trap frequencies and $\bar{a} = \sqrt{\hbar/m\bar{\omega}}$ is the geometric average of the harmonic oscillator lengths .

The equations of motion given in Eq. (4.15) may be recast in terms of the real functions [61]

$$\begin{aligned} S_x &= -\frac{1}{2}(a_1^* a_2 + a_1 a_2^*), \\ S_y &= \frac{i}{2}(a_1^* a_2 - a_1 a_2^*), \\ S_z &= \frac{1}{2}(|a_1|^2 - |a_2|^2). \end{aligned}$$

In terms of the modes that are localized in the left and right wells, the real functions are

$$\begin{aligned} S_x &= \frac{1}{2}(|a_R|^2 - |a_L|^2), \\ S_y &= \frac{i}{2}(a_R^* a_L - a_L^* a_R), \\ S_z &= \frac{1}{2}(a_L^* a_R + a_R^* a_L). \end{aligned}$$

From the above relations it is clear that NS_x is half the difference in the number of atoms in the right and left wells, NS_z is half the difference in the number of atoms in the ground and first excited state, and NS_y is associated with the momentum of the atoms in each of the wells [61]. Finally following [62], the average phase shift

between the atoms in the left and right wells may be defined as $\tan(\phi) = S_y/S_z$.

The equations of motion Eq. (4.15) can be rewritten as the set of real equations, in dimensionless form as

$$\begin{aligned} \frac{d}{dt}S_x &= S_y, \\ \frac{d}{dt}S_y &= -S_x + (\chi - 2PS_x)S_z, \\ \frac{d}{dt}S_z &= -(\chi - 2PS_x)S_y, \end{aligned} \tag{4.18}$$

where the normalized time is $t' = t/\Delta\omega$, and the primes have been dropped. The nonlinearity parameter P is defined by the relation

$$P = 2\frac{U_0\kappa N}{\hbar\Delta\omega} \approx \sqrt{\frac{2}{\pi}}\frac{a_s}{\bar{a}}\frac{\bar{\omega}}{\Delta\omega}N, \tag{4.19}$$

and the anti-symmetric part of the potential enters as $\chi(t) = \eta(t)/\Delta\omega$. The conditions of applicability of the equation of motion Eq. (4.18) are $P \ll \omega_{1,2}/\Delta\omega$ and $\chi \ll \omega_{1,2}/\Delta\omega$.

4.4 Results

In this section, the splitting of a Bose-Einstein condensate in a time-dependent asymmetric double well potential will be discussed by analyzing the equations of motion Eq. (4.18). We begin by briefly reanalyzing the relatively simple case of splitting a condensate using static double well potential and place an upper limit on the number of atoms that can be split using a static potential. Then we discuss how the addition of a time dependent potential can increase the number of atoms that can be split. There are two different mechanisms that can be used to the increase in the number of atoms that can be split. The first of these, uses the anti-

symmetric potential to "cancel" the nonlinearity, thus redcuing the equations of motion to a set of linear equations that can be solve analytically. In the second the anti-symmetric potential changes sufficiently slowly that atoms adiabatically follow the lowest eigenmode of the asymmetric potential.

All of the splitting methods that are discussed in this paper, use tunneling of atoms between two potentail wells. Thus, we assume that the atoms are initially prepared in a state that is localized in the one of the two wells when the condensate is formed and the barrier between the two wells is large enough that the coupling of the occupied and unoccupied wells is negligible. Initially the atoms can be described by the state

$$\begin{aligned} S_x(t=0) &= 1/2, \\ S_y(t=0) &= S_z(t=0) = 0. \end{aligned} \tag{4.20}$$

After the condensate is prepared, the barrier between the two wells is lowered enabling tunneling between the wells. For brevity, we specialize to the case of equal splitting, but one of the advantages of these types of splitters is that any splitting ratio may be realized by varying the splitting time. When the atoms are split into two equal parts, the state of the atoms, at the end of the splitting time, reads

$$\begin{aligned} S_x &= 0, \\ S_y &= \frac{1}{2}\sin\phi_{split} \\ S_z &= \frac{1}{2}\cos\phi_{split}, \end{aligned} \tag{4.21}$$

where ϕ_{split} is the phase difference between the atoms in each well that is introduced by the splitter.

Once the condensate has been split, the barrier between the two wells is once again increased so that the atoms in each well become decoupled. If the local environment in each well is different an additional phase shift ϕ_{signal} will accumulate between the atoms in each well. After a predetermined interaction time, the atoms are recombined and the accumulated phase is measured. Usually the atoms are recombined by suddenly switching off the potential allowing the atoms in each well to expand and overlap. By measuring the interference fringes in the optical density of the overlapping atomic clouds, the total phase shift $\phi = \phi_{split} + \phi_{signal}$ can be determined.

The whole interferometer sequence is then repeated many times. Thus sampling the local environment as it changes in time. Fluctuations of the initial number of atoms prepared in the condensate are unavoidable. In modern experiments, fluctuations are usually on the order of $\Delta N/N \approx \pm 10\%$. To avoid noise in the phase due to the fluctuations of the number of atoms, the splitting process must impart the nearly the same phase shift ϕ_{split} as the number of atoms initially in the condensate fluctuates from shot to shot.

We now briefly repeat the analysis of the splitter using a static double well potential [61, 41, 63, 64]. Since the addition of a static asymmetry does not increase the number of atoms that can be split [64], we may safely set $\chi = 0$ in the following analysis. The normalized population difference between the two wells S_x is shown as a function of normalized time in Fig. 4.1, for two different values of the nonlinearity parameters. These curves were obtained by numerically solving Eq. (4.10). The solid line shows S_x as a function of time where the nonlinearity parameter is $P = 1$. Here, the atomic population oscillate between the two wells and by varying the amount of time that the two wells remain coupled, any splitting ratio may be realized. When the nonlinearity parameter is increased to $P = 3$, as shown as a dashed line if Fig. 4.1,

only a small number of atoms are able to tunnel into the initially unoccupied well and the atoms become "self trapped." The double well can no longer be used to split the condensate in half.

To determine the maximum value of the nonlinearity parameter, where the static double well potential can be used as a beamsplitter, the equations of motion Eq. (4.18) were solved for many different values of the nonlinearity parameter. Since the initial conditions correspond the the larges possible value of the normalized population imbalance, the smaller that S_x becomes, the larger the number of atoms that are able to tunnel into the initially unoccupied well. Figure 4.2 shows the minimum value of of the normalized population imbalance S_x, as a function of the nonlinearity P. For $P > 2$, the minimum value of $S_x = -0.5$, thus any splitting ration may be realized. However, for $P < 2$ the minimum value of S_x rapidly increases and the atoms become "self trapped."

We can use this result and Eq. (4.19) to estimate the maximum number of atoms, that can be split using a static double well potential, to be

$$N < \sqrt{2\pi}\frac{\bar{a}}{a_s}\frac{\Delta\omega}{\bar{\omega}} \tag{4.22}$$

When manipulating ^{87}Rb atoms on an atom chip, the geometric average of oscillator frequencies is typically $\bar{\omega} \approx 2\pi \times 300\ (1/s)$, the average harmonic oscillator length is $\bar{a} \approx 6 \times 10^{-}7$ m, the scattering length is $a_s \approx 5 \times 10^{-9}$ m, and we assume that the tunneling frequency is $\Delta\omega \approx 10^{-1}\bar{\omega}$. Using these numbers, the upper limit on the number of atoms is $N < 30$ atoms. This number can be increased by using potential that has lower trap frequencies, at the cost of a it taking longer to split the atoms.

We now introduce the first method to increase the number of atoms that can be split, using a double well potential, with addition a time dependent antisymmetric

Figure 4.1: The normalized population difference S_x as a function of time t, in a static double well potential. The solid line corresponds to a nonlinearity parameter of $P = 1$ and the dashed line corresponds to a nonlinearity of $P = 3$

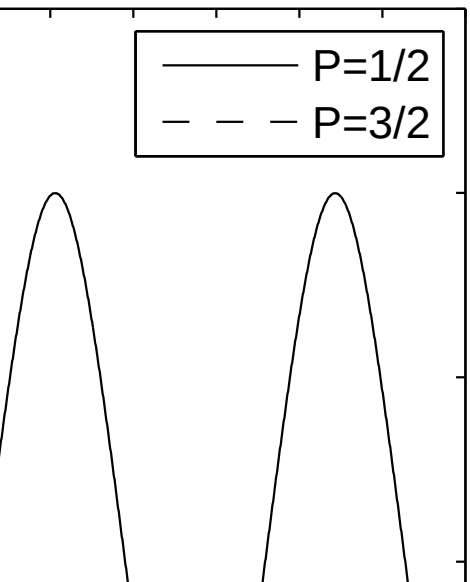

Figure 4.2: The minimum value of the normalized population difference S_x as a function of nonlinearity P, in a static double well potential. When the minimum is $\min(S_x) = -1/2$, when $P < 2$ any splitting ratio may be realized.

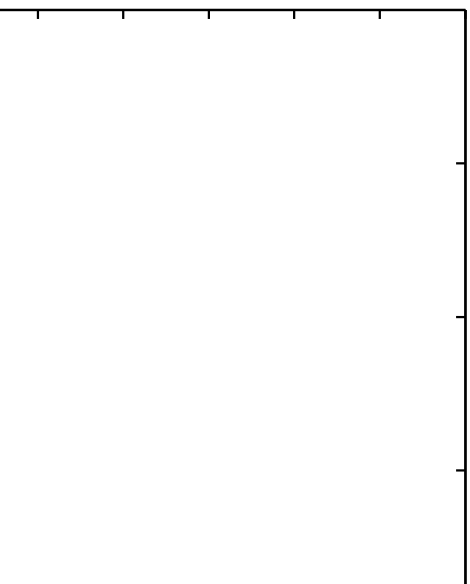

potential. This method used the asymmetry to cancel the nonlinearity. It is clear from the equations of motion Eq. (4.18) that setting

$$\chi(t) = 2PS_x, \tag{4.23}$$

"cancels" the nonlinearity reducing the equations of motion, to a coupled set of linear equations and can be solved exactly. Using the initial conditions Eq. (4.20), the solutions are

$$\begin{aligned} S_x &= \frac{1}{2}\cos t, \\ S_y &= -\frac{1}{2}\sin t, \\ S_z &= 0. \end{aligned} \tag{4.24}$$

Using these solutions in Eq. (4.23), we get

$$\chi(t) = P\cos t. \tag{4.25}$$

To split the atoms equally $\chi(t)$ is given by Eq. (4.25) until the normalized time is $t = \pi/2$, after which $\chi = 0$. After the splitting the state of the condensate can be written as $S_x = 0$, $S_y = -1/2$ and $S_z = 0$. By comparing this with Eq. (4.21) the phase shift introduced by the beamsplitter $\phi_{split} = -90°$.

In order to realize this type of splitter, the nonlinearity parameter must be known *a priori*. To analyze the effects of deviations from the expected nonlinearity (or equivalently variations in the initial number of atoms), we solved the mean-field equations numerically for several different values of the nonlinearity parameter P. The parameter $\chi(t) = P_0\cos t$ with $P_0 = 10$. The results of this calculation is shown in Figs. 4.3 and 4.4. Figure 4.3 shows the normalized population difference S_x, after

the splitting time, as a function of the nonlinearity parameter P. Since the device is tuned to nonlinearity of P_0, the difference in the number of atoms is $S_x = 0$ when $P = P_0$. As the nonlinearity deviates from P_0 by about 10%, the difference between the population difference varies by about the same percentage.

The phase difference between the atoms left and right wells after the splitting ϕ_{split} is considerably more sensitive to the nonlinearity . This is shown in Fig. 4.4, which plots the phase difference acquired during the splitting as a function of the nonlinearity parameter P. As expected when $P = P_0$, the phase shift is $-90°$. However, if the nonlinearity varies by $\pm 10\%$, the phase shift fluctuations between $\phi_{spit} = -80°$ and $\phi_{spit} = -150°$.

The primary advantage of splitting the condensate by using the asymmetry of the potential to "cancel" the nonlinearity is that the condensate may be split rapidly. The sensitivity of the splitting phase to the nonlinearity can be compensated for in two different ways. Fist, the fluctuations in the initial number of atoms could potentially be reduced. Second, the total number of atoms in the interferometer could be measured determined after the interference sequence and the splitting phase can be determined from this number.

We now discuss the second type of splitter, that uses a time dependent potential is used to increase the number of atoms that can be split. In this case the potential changes sufficiently slowly that the atoms remain the lowest eigenmode of the total potential. When the condensate is prepared when the asymmetry is large, $|\chi| \gg P$ so that the lowest eigenmode corresponds to the atomic population localized in one of the potential wells. When the anti-symmetric part of the potential is turned off $\chi = 0$ and the lowest eigenmode corresponds the population begin equal. If the potential is turned off adiabatically slowly the population will remain in the lowest eigenmode.

Figure 4.3: The normalized population difference S_x of total the nonlinearity. The splitter is tuned to $P = P_0$.

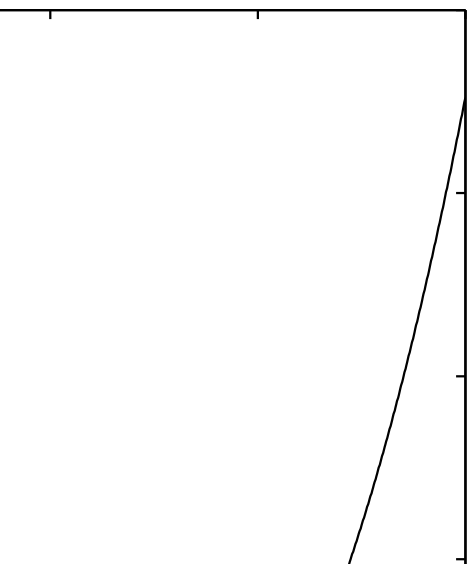

Figure 4.4: The phase difference imparted by the splitter ϕ_{split} as a function of the nonlinearity. The splitter is tuned to $P = P_0$.

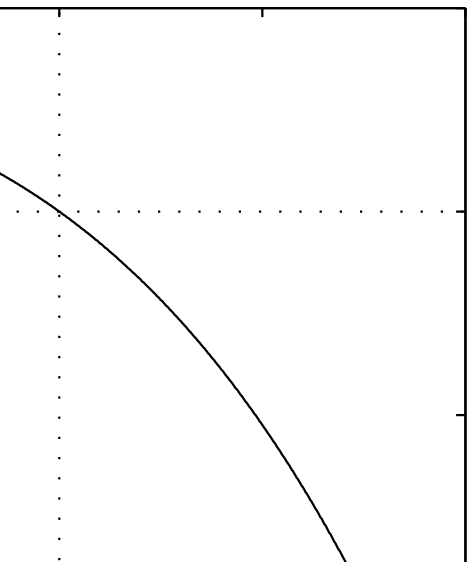

Inorder for us to determine how slowly the anti-symmetric potential must be turned off, we solved the equations of motion Eq. (4.18) numerically, with the initial conditions Eq. (4.20). In what follows, the parameter χ is a linear function of time, given by

$$\chi(t) = \chi_0(1 - t/\tau), \tag{4.26}$$

where χ_0 is the initial value of the control parameter, and τ is the splitting time.

Figure 4.5 shows the normalized population difference S_x as a function of time for a typical numerical calculation. In this figure, the nonlinearity parameter is $P = 10$, the initial value of the control parameter is $\chi_0 = 20$, and the splitting time is $\tau = 10$. At the initial time, all of the atoms are found in the right well. When the parameter χ becomes nearly equal to the nonlinearity $\chi \approx P$ at the time $t = 5$, the atoms begin tunneling into the left well. At the end to the splitting time $t = \tau$, $\chi = 0$, and half of the atoms have tunneled from the right into the left well, $S_x = 0$.

To determine the lower limit on the splitting time that will result in an equal number of atoms in each well, we solved the equations of motion for several different values of the splitting time τ. The normalized population difference S_x as a function of splitting time τ at the end of the splitting $t = \tau$ is shown in Fig. 4.6. In the figure we take the nonlinearity to be $P = 10$ and $\chi_0 = 20$. In the limit $\tau \ll 1$, the atoms simply do not have time to tunnel from the right to the left well and remain in the right. However, when $\tau > 10$, the population of each well becomes nearly equal.

In Fig. 4.7, the phase difference caused by the splitting ϕ_{split} after the splitting $t = \tau$, is shown as a function of τ and the same parameters as Fig. 4.6. For fast splitting, $\tau < 10$, the phase changes rapidly as a function of splitting time. For larger time, $\tau > 10$, the phase shift become a slowly varying function of τ, and approaches zero in the limit $\tau \to \infty$.

Figure 4.5: The normalized population difference S_x as a function of time.

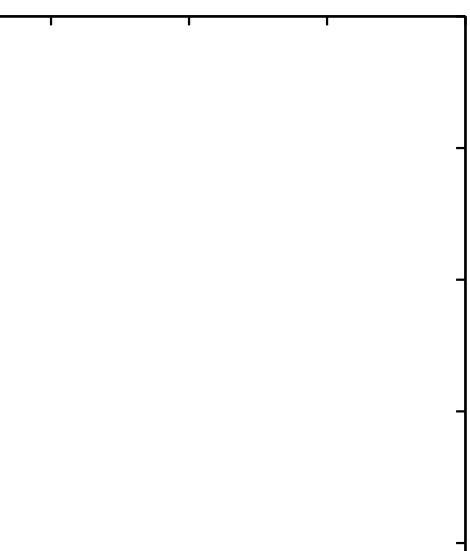

Figure 4.6: The normalized population difference S_x as a function of splitting time τ.

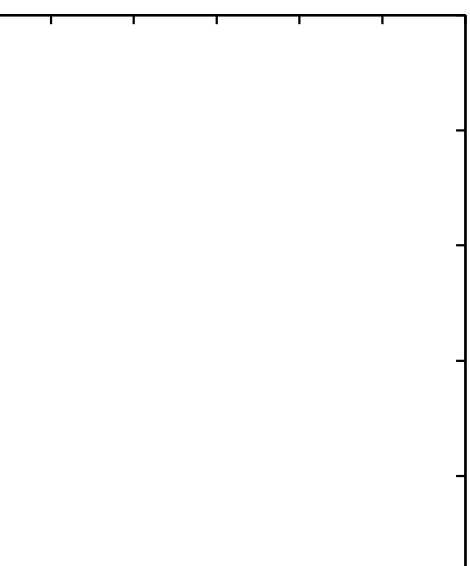

Figure 4.7: The phase difference imparted by the splitter ϕ_{split} as a function of splitting time τ.

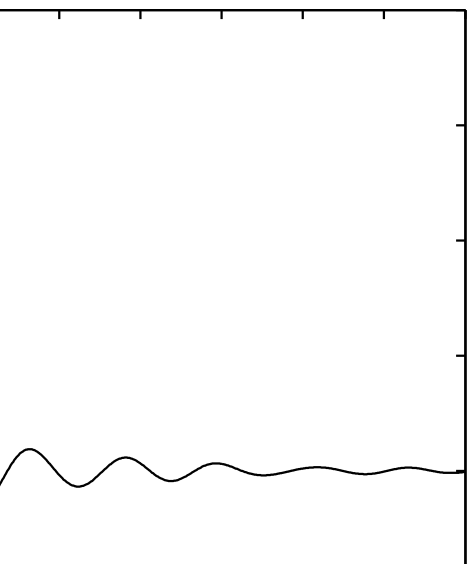

The fact that the final phase of the atoms does not approach zero quickly as τ becomes larger would seem like a potential problem. Since an interferometer measures only differences in phase, as long as the magnitude phase shift that is introduced during the splitting process is always the same, its magnitude of it is does not cause problems in the operator of the interferometer. To verify that the phase shift introduced during the splitting ϕ_{split} is insensitive to the total number of atoms, we solved the mean-field equations for many different values of the nonlinearity. We use the parameters $\tau = 10$ and $\chi_0 = 20$. Figure 4.8 shows the variation in population imbalance S_x as a function of the nonlinearity parameter P. Variations in the nonlinearity parameter from $P = 5$ to $P = 15$, result in variations in the splitting ratio of as little as 5%. The phase that accumulated during the splitting is somewhat more sensitive to the number, as shown in Fig. 4.9, where variations in the nonlinearity between $P = 5$ and $P = 15$ results in a variation of the phase between $\phi_{split} = -20^\circ$ and $\phi_{split} = -5^\circ$.

To split a condensate by changing the anti-symmetric potential adiabatically slowly, the anti-symmetric potential must be turned off in a dimensionless time $\tau \approx P$. As a result, the larger the nonlinearity, the longer it takes to split. However, this method is insensitive to changes in the number of atoms and make for a very robust beamsplitter.

4.5 Conclusions

We have presented a theoretical analysis of a new methods to split Bose-Einstein condensate, using a time dependent asymmetric double well potential. The mechanism for the splitting is quantum tunneling between the two wells. First, the analysis of splitting in a static double well potential was repeated, and we placed an upper

Figure 4.8: The normalized population difference S_x as a function of total number of atoms as a function of the nonlinearity P.

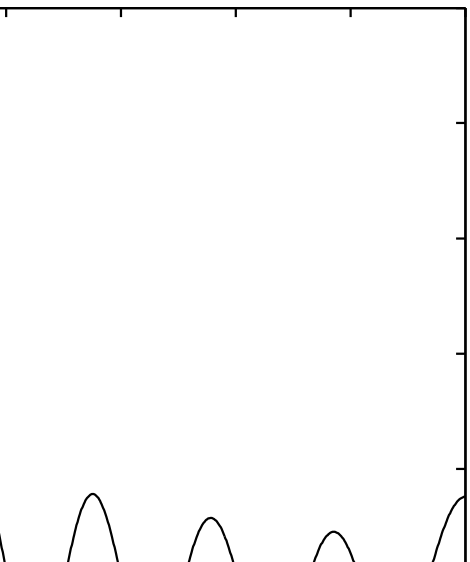

Figure 4.9: The phase difference imparted by the splitter ϕ_{split} as a function of the nonlinearity P.

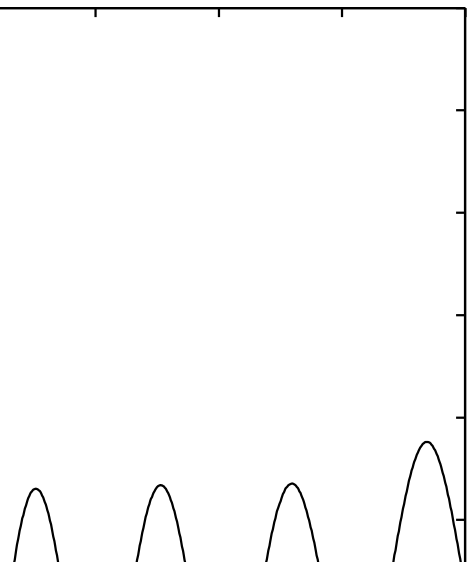

limit on the number of atoms that can be split using a static potential. Next, we introduce the use of an anti-symmetric potential to "cancel" the nonlinearity, thus dramatically increasing the number of atoms that can be split without increasing the splitting time. Then, we discussed a second method to increase the number of atoms that can be split by changing the anti-symmetric potential more slowly so that the atoms remain adiabatic. We demonstrated that while the adiabatic method is somewhat slower than the first, it is considerably more robust to fluctuations in the nonlinearity of the condensate.

The methodologies discussed here are not limited to the case of a trapped atom interferometer, but can be easily generalized to a beam type interferometer that operates continuously. In the future, we will investigate the beam devices, extend the model beyond the two-mode approximation, and investigate trap geometries that may be used for experimental realization.

Chapter 5

BEC based interferometry with optical control of dynamics

5.1 Introduction

In this chapter, we propose a method for increasing the coherence time of an atom Michelson interferometer by simply recombining the condensate at a slightly different time. To determine the new recombination time, we develop a simple, quantitatively accurate analytical model of the interferometer, and demonstrate the validity of these analytic expressions my making direct comparisons with numerical solutions of the Gross-Pitaevskii equation.

The interferometric cycle of duration T starts by illuminating the motionless BEC cloud ψ_0 with a splitting pulse from a pair of counter- propagating laser beams. This pulse acts like a diffraction grating splitting the cloud into two harmonics ψ_+ and ψ_-. The atoms diffracted into the $+1$ order absorb a photon from a laser beam with the momentum $\hbar k_l$ and re-emit it into the beam with the momentum $-\hbar k_l$ acquiring the net momentum $2\hbar k_l$. The cloud ψ_+ starts moving with the velocity $v_0 = 2\hbar k_l/M$, where k_l is the wavenumber of the laser beams and M is the atomic mass. Similarly, the cloud ψ_- starts moving with the velocity $-v_0$. The two harmonics are allowed to propagate for the time $T/2$ and are illuminated by a reflection optical pulse. The atoms in the harmonics ψ_+ change their velocity by $-2v_0$ and those in the harmonics ψ_- by $2v_0$. The harmonics propagate back for time $T/2$ and are subject to the action of the recombination optical pulse. After the recombination, the atoms in general populate all three harmonics ψ_0 and $\psi_\pm$. The degree of population depends on the relative phase between the harmonics $\psi_\pm$ acquired during the interferometric cycle and can be used to deduce this phase. In particular, the wave function of the zero-momentum harmonics ψ_0 after the recombination is equal to

$$\psi_0 = \frac{1}{\sqrt{2}}(\psi_+ + \psi_-), \tag{5.1}$$

where $\psi_\pm$ are the wave functions of the ± 1 harmonics immediately before the recombination.

Because of the nonlinearity and/or the external potential, the harmonics $\psi_\pm$ do not travel with he velocities $\pm v_0$ during the cycle. First, the cloud "climbing up" the external potential slows down and the one moving "downhill" speeds up. Second, because of the nonlinearity, the speeds of the two clouds after their separation will be slightly larger than v_0 if the nonlinearity is repulsive and slightly less than v_0 if it is attractive. For definiteness, we shall discuss the influence of the repulsive nonlinearity assuming that the external potential is zero. An ideal operation of the interferometer in this case corresponds to all the atoms populating zero-momentum harmonics ψ_0 after the recombination, i.e., to $N_0 = N_{tot}$.

Because of the atom-atom interaction, the clouds $\psi_\pm$ exert a repulsive force on each other during the time they overlap. This force accelerates each cloud so that after the separation pulse the $\psi_\pm$ harmonics propagate with velocities $\pm(v_0 + \delta v)$, where $\delta v > 0$. The reflection pulses impart the momenta $\mp 4\hbar k_l$ to the clouds transforming their roles: $\psi_\pm \to \psi_\mp$. After the reflection, the ± 1 harmonics propagate with the velocities $\pm(v_0 - \delta v)$. Harmonics' deceleration due to mutual repulsion during their overlap decreases the velocity of each harmonics by an additional δv so immediately before the recombination the harmonics' velocities are $\pm(v_0 - 2\delta v)$.

The nonzero value of δv results in two consequences. First, since the clouds' speeds after the reflection pulse are smaller than before the pulse, the ± 1 harmonics at the nominal recombination time still do not overlap each other completely. This effect is typically not very significant. Much more important is the fact that the returning harmonics have momenta that are not equal to $\pm 2\hbar k_l$ and can not therefore be compensated by the recombination pulse. As a result, the wave function of the

zero-momentum harmonics ψ_0 after the recombination can be written as

$$\psi_0 \propto \sqrt{n(x)}\cos(\Delta k x), \tag{5.2}$$

where $\Delta k = 2M\delta v/\hbar$ and $n(x)$ are the density profiles of the harmonics; their possible incomplete overlap has been neglected. The population of the zero-momentum harmonics is obtained by the spatial integration of $|\psi_0|^2$. For $\Delta k R \ll 1$, where R is the characteristic size of the clouds, all the atoms after the recombination are indeed in the zeroth harmonics, i.e. $N_0 = N_{tot}$. In the opposite case $\Delta k R \gg 1$, the cos function oscillates several times across the cloud and $N_0/N_{tot} = 1/2$ resulting in the loss of contrast. It is worth noting that the accumulation of corrections to the wave vectors of the clouds is due to the fact that the reflecting pulses do not reverse the clouds' velocities but rather add a constant velocity $\pm 2v_0$ to them. This explains the fact that the coherence may be lost due to an external quadratic potential even in the linear case when the nonlinearity is negligible.

The above-discussed loss of coherence due to incomplete cancelation of the wave vectors of the harmonics by the recombination pulse can be also visualized in the following way: the wave functions of the $\psi_\pm$ harmonics can be represented as $\psi_\pm = \sqrt{n_\pm(x)}\exp(i\phi_\pm)$, where $\phi_\pm$ is the parabolic phase (the nominal phase $\pm(Mv_0/\hbar)x$ is taken care of by the optical pulses and is not included). In the ideal situation, the parabolic phase for each cloud is centered at the middle of the cloud. Nonzero values of δv (or, equivalently, nonzero values of the corrections to the wave vectors of the clouds) mean that the phase of each cloud leads or lags behind its density envelope. This situation is schematically illustrated in Fig. 5.1 showing the harmonic ψ_+ before the recombination with its phase leading the density envelope. We shall show that the optimum recombination corresponds to the situation when the phase

profiles, not the density envelopes of the clouds are on top of each other immediately before the recombination.

Operation with high values of the contrast can be achieved in several ways. First, the relative magnitudes of the nonlinearity and the external potential are adjusted in such a way that their effects cancel each other for a given cycle time T (this is not always possible). Second, the recombination and/or reflection are conducted with optical pulses having different wavelength as compared to the splitting pulse to compensate for the change in the wave vectors of the moving clouds. Finally, the recombination is carried out not at the nominal recombination time T but at a time such that $\Delta kR = 0$. The paper is devoted to the analysis of the last possibility.

The rest of the chapter is structured as follows: Sec. 5.2 provides general formulation of the problem, Sec. 5.3 introduces analytical model of the interferometric cycle and Sec. 5.4 is devoted to the analysis of the contrast and contains the analytical expressions for the optimized recombination time. These expressions are discussed in different limiting cases in Sec. 5.5.

5.2 Formulation of the problem

The evolution of the condensate in the interferometer in the mean-field limit is described by the Gross-Pitaevskii equation

$$i\hbar\frac{\partial}{\partial t}\Psi(\boldsymbol{r},t) = \left(-\frac{\hbar^2}{2M}\nabla^2 + V_{tot}(\boldsymbol{r},t) + U_0 N|\Psi|^2\right)\Psi(\boldsymbol{r},t), \tag{5.3}$$

where $\Psi(\boldsymbol{r},t)$ is the wave function of the condensate that is normalized to one, N is the total number of atoms, $U_0 = 4\pi\hbar^2 a_s/M$ characterizes the strength of interatomic interactions, a_s is the s-wave scattering length and M is the atomic mass. The potential $V_{tot} = V_{3D}(\boldsymbol{r},t) + V_{opt}(t)\cos(2k_l x)$ is the sum of a confining

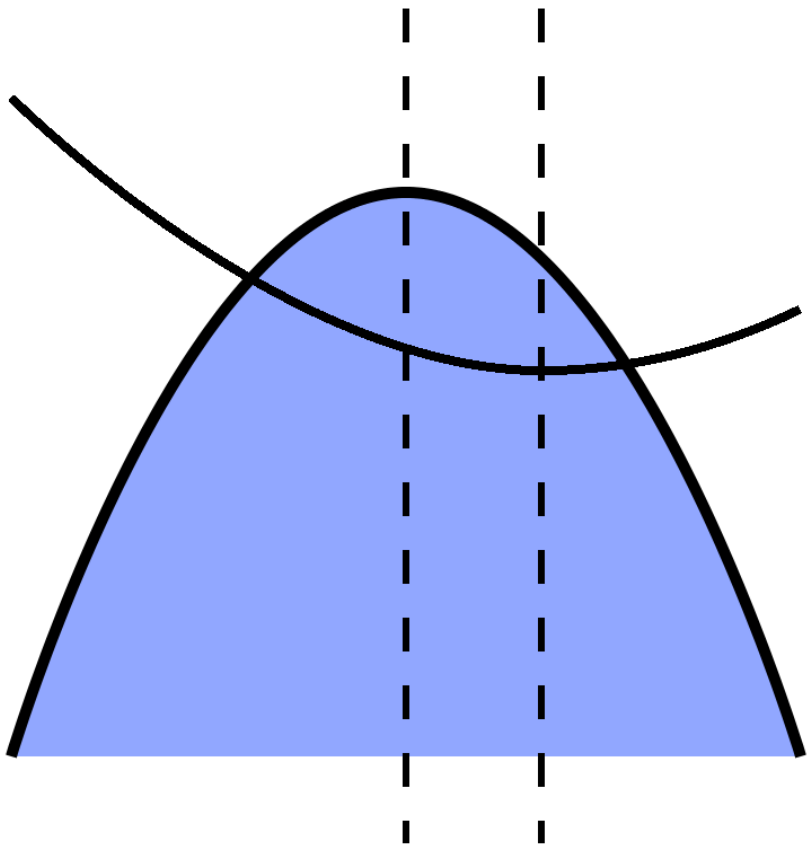

Figure 5.1: The density and phase of the ψ_+ harmonic before the recombination.

potential V_{3D} and an optical potential that is created by two counter-propagating laser beams of wavelength $\lambda = 2\pi/k_l$, which are detuned from the atomic resonance to avoid spontaneous emission. The optical potential is used to split, recombine and reverse direction of propagation of the BEC clouds.

The confining potential is of the form

$$V_{3D}(\boldsymbol{r}, t) = V(x, t) + M\omega_\perp^2 r_\perp^2/2, \tag{5.4}$$

where $V(x, t)$ is slowly-spatially-varying potential due to the environment and $M\omega_\perp^2 r_\perp^2/2$ is the guiding potential providing confinement of the condensate along the two spatial dimensions $\boldsymbol{r}_\perp = (y, z)$. In the following we shall assume that the condensate is tightly confined in the two transverse dimensions and is in the lowest transverse mode of the guide

$$\psi_\perp(r_\perp) = \frac{1}{\sqrt{\pi} a_\perp} \exp(-r_\perp^2/2a_\perp^2), \tag{5.5}$$

where $a_\perp = (\hbar/M\omega_\perp)^{1/2}$ is the transverse oscillator length. Factorizing the wave function of the condensate as $\Psi(\boldsymbol{r}, t) = \psi(x, t)\psi_\perp(r_\perp)$, Eq. (5.3) can be reduced to the one-dimensional equation for the function $\psi(x, t)$. Introducing dimensionless coordinate $x \to 2k_l x$ and time $\tau = t/t_0$, where $t_0 = M/(4\hbar k_l^2)$, this one-dimensional Gross-Pitaevskii equation can be written as

$$i\frac{\partial}{\partial\tau}\psi(x, \tau) = \left[-\frac{1}{2}\frac{\partial^2}{\partial x^2} + v(x, \tau) + \Omega(\tau)\cos(x) + p|\psi|^2\right]\psi(x, \tau), \tag{5.6}$$

where $v = (V/\hbar)t_0$, $\Omega = (V_{opt}/\hbar)t_0$ and $p = a_s N/a_\perp^2 k_l$.

The optical potential $\Omega(\tau)\cos x$ acts as a diffraction grating for the condensate wave function ψ. This grating diffracts the condensate into several harmonics separated by multiples of the grating wavevector. If the width of the Fourier spectrum

of the condensate is much smaller than the length of the grating wavevector (one in our dimensional units), the wave function $\psi(x,t)$ in Fourier space consists of a series of narrow peaks. It is therefore convenient to represent $\psi(x,t)$ as

$$\psi(x,t) = \sum_n \psi_n(x,t)\exp(inx), \tag{5.7}$$

where harmonics' envelopes $\psi_n(x)$ are slowly-varying functions of coordinate as compared with the exponentials. The dynamics of these harmonics are governed by the set of coupled equations

$$\begin{aligned} i\left(\frac{\partial}{\partial\tau} + in\frac{\partial}{\partial x}\right)\psi_n = \frac{1}{2}\left(-\frac{\partial^2}{\partial x^2} + n^2\right)\psi_n + v(x,\tau)\psi_n \\ + \frac{\Omega(\tau)}{2}(\psi_{n+1} + \psi_{n-1}) + p\sum_{l,m}\psi_l^*\psi_m\psi_{n-m+l}. \end{aligned} \tag{5.8}$$

The optical potential $\Omega(\tau)$ in Eq. (5.6) is used to split the initial zero-momentum BEC cloud at the beginning of the interferometric cycle into the two harmonics with the momenta ± 1, reverse their direction of propagation in the middle of the cycle and recombine them at the end. Dynamics of the BEC due to the optical potential was fully taken into account in solving the Gross-Pitaevskii equation numerically. In the analytical model, their action was described in terms of simple transformation matrices. For self-consistency of the presentation, a brief derivation of parameters of optical pulses used in the numerical solution of the Gross-Pitaevskii equation is given in the Appendix. The material of the Appendix has been previously discussed in Refs. [43, 65, 34]. The next section is devoted to the development of analytical model describing evolution of the BEC between the optical pulses.

5.3 Parabolic model

Between the optical pulses the condensate consists of two harmonics with $n = \pm 1$ whose evolution is described by the set of coupled equations

$$i\left(\frac{\partial}{\partial\tau} \pm \frac{\partial}{\partial x}\right)\psi_\pm = -\frac{1}{2}\frac{\partial^2}{\partial x^2}\psi_\pm + v(x)\psi_\pm + p\left(|\psi_\pm|^2 + 2|\psi_\mp|^2\right)\psi_\pm. \tag{5.9}$$

Introducing the density and phase of each harmonic by the relations

$$\psi_\pm = \sqrt{n_\pm}\exp(i\phi_\pm)$$

and using the Thomas-Fermi approximation (neglecting the second derivatives of the density) transforms the set of equations (5.9) to the form

$$\begin{aligned}
\left(\frac{\partial}{\partial\tau} \pm \frac{\partial}{\partial x}\right)n_\pm &= -\frac{\partial}{\partial x}\left(n_\pm\frac{\partial\phi_\pm}{\partial x}\right), \\
\left(\frac{\partial}{\partial\tau} \pm \frac{\partial}{\partial x}\right)\phi_\pm &= -\frac{1}{2}\left(\frac{\partial\phi_\pm}{\partial x}\right)^2 - v - p(n_\pm + 2n_\mp).
\end{aligned} \tag{5.10}$$

We will describe the external potential v by the first two terms of the Taylor expansion

$$v(x) = \alpha x + \frac{1}{2}\beta x^2 \tag{5.11}$$

and analyze the set of Eq. (5.10) in the framework of a parabolic approximation where expressions for both the density and the pase do not contain terms higher than the second order in coordinate:

$$\begin{aligned}
n_\pm &= \frac{3}{8R}\left[1 - \frac{(x - x_\pm)^2}{R^2}\right], \\
\phi_\pm &= \varphi_\pm + \kappa_\pm(x - x_\pm) + \frac{g}{2}(x - x_\pm)^2.
\end{aligned} \tag{5.12}$$

R, $x_\pm$, $\kappa_\pm$, $\varphi_\pm$ and g are functions of time τ only. The coefficient 3/8 in the expression for $n_\pm$ follows from the normalization condition (each harmonics is normalized to 1/2). Note that for each cloud its density and phase in Eq. (5.12) are defined only in the region where the density is nonnegative. Functions $x_\pm(\tau)$ are positions of the centers of mass of the two moving clouds, $\kappa_\pm$ are corrections to their nominal wavevectors (± 1) that are due to the external potential and the nonlinearity and $\varphi_\pm$ are the accumulated coordinate-independent phases. Finally, R is the half-size of each of the clouds and the parameter g multiplying the quadratic part of the phase is analogous to the inverse of the radius of curvature of the wavefront of a propagating light beam in optics.

Using Eq. (5.12) and the first of Eq. (5.10), one gets

$$\begin{aligned} R' &= g_\pm R, \\ x'_\pm &= \pm 1 + \kappa_\pm, \end{aligned} \tag{5.13}$$

where the prime means differentiation with respect to time. Treatment of the second Eq. (5.12) is slightly complicated by the fact that the regions of existence of n_+ and n_- do not coincide. Since the functional forms of n and ϕ are fixed, the density profile $n_\mp$ should be projected onto $n_\pm$. To do this, one can choose a set of suitable basis functions defined at the interval $|\xi_\pm| \leq 1$, where $\xi_\pm = (x - x_\pm)/R$, that can be used to represent the density $n_\pm$ and the phase $\phi_\pm$. The density $n_\mp$ should then be expressed in terms of the same basis set retaining only the functions that describe $n_\pm$ and $\phi_\pm$. Using Legendre polynomials $P_n(\xi_\pm)$ as the basis yields

$$\frac{16R}{3} n_\mp(\xi_\pm) \to d_0 \mp d_1 \xi_\pm - d_2 \xi_\pm^2, \tag{5.14}$$

where

$$
\begin{aligned}
d_0 &= \left(2 - \frac{7}{2}|q|^2 + 2|q|^3 - \frac{1}{8}|q|^5\right)\theta(|q| < 2), \\
d_1 &= q\left(4 - 3|q| + \frac{1}{4}|q|^3\right)\theta(|q| < 2), \\
d_2 &= \left(2 - \frac{15}{2}|q|^2 + 5|q|^3 - \frac{3}{8}|q|^5\right)\theta(|q| < 2)
\end{aligned} \tag{5.15}
$$

and $q = (x_+ - x_-)/R$. The θ-function in Eq. (5.15) is equal to one if its argument is a logical true and zero if its is a logical false.

Using Eq. (5.14) in the second of Eq. (5.10) yields equations of motion for g, $\kappa_\pm$ and $\varphi_\pm$. Combining these with Eq. (5.13), we get the final set of equations

$$
\begin{aligned}
R' &= gR, \\
g' &= -g^2 - \beta + \frac{3p}{4R^3}(1 + d_2), \\
\kappa'_\pm &= -\alpha - \beta x_\pm \pm \frac{3p}{8R^2}d_1, \\
x'_\pm &= \pm 1 + \kappa_\pm, \\
\varphi'_\pm &= \frac{\kappa_\pm^2}{2} - \alpha x_\pm - \frac{1}{2}\beta x_\pm^2 - \frac{3p}{8R}(1 + d_0),
\end{aligned} \tag{5.16}
$$

where prime means differentiation with respect to time. Equations (5.16) have simple physical interpretation. The rates of change of the coordinates of the two clouds $\psi_\pm$ are given by the relations $x'_\pm = \pm 1 + \kappa_\pm$, i.e., the clouds move with velocities $\pm 1 + \kappa_\pm$. The major contributions to the velocities ± 1 are due to the momenta imparted to the clouds by the optical pulses. The corrections $\kappa_\pm$ are due to the external potential (parameters α and β) and the nonlinearity. The cloud "climbing up" the external potential slows down and the one moving "downhill" speeds up. If the nonlinearity is repulsive ($p > 0$), the speeds of the two clouds after their separation will be slightly larger than one and if it is attractive, slightly

less than one. The functions d_0, d_1 and d_2 given by Eq. (5.15) describe mutual interaction of the two clouds. They depend on the relative displacement of the clouds $q = (x_+ - x_-)/R$ and are nonzero only when $|q| < 2$, i.e., when the clouds overlap. The other terms containing the nonlinearity parameter p describe self interaction for each of the clouds and are always nonzero.

5.3.1 Evolution of $\kappa_\pm$ and $x_\pm$

During the interferometric cycle the two BEC clouds $\psi_\pm$ may be partially overlapping of non-overlapping. In the subsequent analysis, it will be assumed that the size of each cloud does not change significantly at the time intervals $\tau \propto R$ that it takes for the clouds to pass each other. The conditions of applicability of this assumption are given by Eq. (5.29). Additionally, it will be assumed that $\beta T^2 \ll 1$, where T is the duration of the interferometric cycle.

Time evolution of $\kappa_\pm$ and $x_\pm$ is governed by the set of two coupled equations (cf. (5.16))

$$\begin{aligned} \kappa'_\pm &= -\alpha - \beta x_\pm \pm \frac{3p}{8R^2} d_1, \\ x'_\pm &= \pm 1 + \kappa_\pm, \end{aligned} \tag{5.17}$$

Solution of Eqs. (5.17) can be written as

$$\kappa_\pm(\tau) = \kappa_{\pm,0} - \alpha\tau - x_{\pm,0}\beta\tau \mp \frac{1}{2}\beta\tau^2 \pm \frac{3p}{16R}\int_{q_0}^{q_0+2\tau/R_0} dq d_1(q), \tag{5.18}$$

$$\begin{aligned} x_\pm(\tau) &= x_{\pm,0} + (\pm 1 + \kappa_{\pm,0})\tau - \frac{1}{2}\alpha\tau^2 - \frac{1}{2}x_{\pm,0}\beta\tau^2 \mp \frac{1}{6}\beta\tau^3 \\ &\pm \frac{3p}{32}\int_{q_0}^{q_0+2\tau/R_0} dq \int_{q_0}^{q} dq' d_1(q'), \end{aligned} \tag{5.19}$$

where $\kappa_{\pm,0}$, $x_{\pm,0}$ and R_0 are initial values of $\kappa_\pm$, $x_\pm$ and R. In deriving Eq. (5.18) and (5.19), the dynamics of the relative separation between the clouds in evaluating function d_1 was approximated by the relation

$$q(\tau) = q_0 + \frac{2\tau}{R_0}, \tag{5.20}$$

i.e., the terms with $\kappa_\pm$ were neglected as compared to one in evaluating $q(\tau)$.

The interferometric cycle of duration T starts by applying the splitting optical pulses to the motionless cloud ψ_0, letting harmonics $\psi_\pm$ propagate for the time $T/2$, reverse their directions of propagation by applying the reflection pulses, letting the harmonics $\psi_\pm$ evolve for the time $T/2$ and apply the recombination optical pulses.

Immediately after the splitting pulses at $\tau = 0$, the center of mass of each harmonic is $x_{\pm,0} = 0$, $q_0 = 0$ and $\kappa_{\pm,0} = 0$. The reflection pulse reverses directions of propagation of the two harmonics by adding momenta ∓ 2 to the momenta $\pm 1 + \kappa_\pm$ of $\psi_\pm$. After the reflection pulse the harmonic ψ_+ becomes ψ_- and vice versa. As a result, immediately after the reflection pulse, $x_{\pm,0} = x_\mp(T/2)$ and $\kappa_{\pm,0} = \kappa_\mp(T/2)$.

At the nominal recombination time $\tau = T$, the corrections to the velocities $\kappa_\pm$ and the center of mass coordinates $x_\pm$ are given by the relations

$$\kappa_\pm(T) = -\alpha T \pm \frac{1}{4}\beta T^2 \mp p\left[\frac{1}{R_0}D_1(T/R_0) + \frac{1}{R_T}D_1(T/R_T)\right], \tag{5.21}$$

$$\begin{aligned} x_\pm(T) &= -\frac{1}{2}\alpha T^2 \pm \frac{1}{8}\beta T^3 \\ &\mp \frac{p}{2}\left[\int_{T/R_T}^{T/R_0} dq D_1(q) + \frac{T}{R_0}D_1(T/R_0) + \frac{T}{R_T}D_1(T/R_T)\right], \end{aligned} \tag{5.22}$$

where

$$D_1(x) = \begin{cases} \frac{3}{16}x^2\left(2 - x + \frac{1}{20}x^3\right) & , \quad x < 2 \\ D_1(2) = 3/10 & , \quad x > 2, \end{cases} \tag{5.23}$$

R_0 is the size of the harmonics at the separation stage and R_T is the size during recombination.

5.3.2 Evolution of g and R

Evolution of g and R is governed by the set of two coupled equations (see Eq. (5.16))

$$\begin{aligned} R' &= gR, \\ g' &= -g^2 - \beta + \frac{3p}{4R^3}(1 + d_2). \end{aligned} \tag{5.24}$$

The explicit expressions for g and R at time intervals τ such that R does not change significantly, i.e., $|\Delta R| \ll R$, are of the form

$$g(\tau) = g_0 - \beta\tau + \frac{3p}{8R_0^2}\int_{q_0}^{q_0+2\tau/R_0} dq[1 + d_2(q)], \tag{5.25}$$

$$R(\tau) = R_0 + R_0\left[g_0\tau - \frac{\beta}{2}\tau^2 + \frac{3p}{8R_0^2}\int_0^\tau d\tau' \int_{q_0}^{q_0+2\tau'/R_0} dq[1 + d_2(q)]\right], \tag{5.26}$$

where $g_0 = g(0)$, $q_0 = q(0)$ and $R_0 = R(0)$ are initial values of g, q and R. In deriving Eqs. (5.25) and (5.26), the terms of the order $\kappa_\pm$ in the equations for $x_\pm$ have been neglected as compared to one. The dynamics of the relative separation between the clouds in the framework of this approximation is given by the expression

$$q(\tau) = q_0 + \frac{2\tau}{R_0} \tag{5.27}$$

Equations (5.25) and (5.26) are valid provided

$$g_0\tau,\ \beta\tau^2,\ \frac{p\tau^2}{R_0^3} \ll 1 \tag{5.28}$$

In the analysis of Sec.5.3.1 and in the rest of the paper it is assumed that the size of each cloud does not change significantly during the time $\tau = R$ that it takes for the clouds to pass each other. The conditions of applicability of this approximation are

$$g_0 R_0,\ \beta R_0^2,\ \frac{p}{R_0} \ll 1 \tag{5.29}$$

Using Eq. (5.25), we get the following expression for the value of g at the recombination time in the limit when R does not change significantly during the interferometric cycle:

$$g(T) = g_0 - \beta T + \frac{3pT}{4R^3} + \frac{p}{R^2} D_2(T/R), \tag{5.30}$$

where

$$D_2(x) = \begin{cases} \frac{3}{4}x\left(2 - \frac{5}{2}x^2 + \frac{5}{4}x^3 - \frac{1}{16}x^5\right) & , \quad x < 2, \\ D_2(2) = 0 & , \quad x > 2 \end{cases} \tag{5.31}$$

The limit $|\Delta R| \ll R$ can correspond to both $\tau < R$ when the clouds stay overlapped during all the cycle and to $\tau \gg R$ when they do not overlap most of the cycle. The second limit of interest to be considered in this section $\tau \gg R$ explicitly deals with the situation when the clouds do not overlap most of the time. In this limit, the contribution coming from the function d_2 in Eq. (5.24) (interaction between the clouds) can be neglected as compared to their self action. The function

g in this limit is given by the relation

$$g(\tau) = \frac{1}{r}\frac{d}{d\tau}r = \frac{\text{sign } g_0}{r}\left[g_0^2 - \frac{3p}{2R_0^3}\left(\frac{1}{r} - 1\right) - \beta(r^2 - 1)\right]^{1/2}, \tag{5.32}$$

where $r = R(\tau)/R_0$. Note that Eq. (5.32) is valid for any values of $R(\tau)$. The general expression for $R(\tau)$ can be obtained in terms of elliptic integrals but is too cumbersome to be of practical use. In the limit where the relative change in the size of each harmonic is small($|r - 1| \ll 1$), one gets

$$\begin{aligned} R(\tau) &= R_0 + R_0\left[g_0\tau + \left(\frac{3p}{4R_0^3} - \beta\right)\frac{\tau^2}{2}\right], \\ g(\tau) &= g_0 + \left(\frac{3p}{4R_0^3} - \beta\right)\tau. \end{aligned} \tag{5.33}$$

These expressions coincide with Eqs. (5.25) and (5.26) when $\tau \gg R$ and describe the situation when the clouds do not overlap most of the time but their sizes do not changes significantly during all their evolution time.

In the opposite limit $R(\tau) \gg R_0$,

$$g(\tau) = \text{sign } g_0 \frac{R_0}{R(\tau)}\left[g_0^2 + \frac{3p}{2R_0^3} - \beta\frac{R^2(\tau)}{R_0^2}\right]^{1/2} \tag{5.34}$$

5.3.3 Evolution of $\varphi_\pm$

In an interferometric experiment, the quantity of interest is not the absolute phase of each harmonic $\varphi_\pm$, but rather the relative phase $\Delta\varphi = \varphi_+ - \varphi_-$. The time evolution of $\Delta\varphi$ is governed by the equation

$$\Delta\varphi' = \frac{1}{2}(\kappa_+^2 - \kappa_-^2) - \alpha(x_+ - x_-) - \frac{1}{2}\beta(x_+^2 - x_-^2) \tag{5.35}$$

Using results of Section 5.3.1 and neglecting terms containing products and quadratic or higher combinations of α, β and p yields

$$\Delta\varphi(T) = -\frac{\alpha}{2}T^2 \tag{5.36}$$

5.4 The interference signal

The wavefunction of the zero-momentum harmonics after the recombination is given by the expression:

$$\psi_0(x) = \frac{1}{\sqrt{2}}\left[\psi_+(x) + \psi_-(x)\right] \propto \frac{1}{\sqrt{2}}\left[\sqrt{n(x-x_+)}\exp(i\theta_0/2 + i\Delta k x/2)\right.$$
$$\left. + \sqrt{n(x+x_+)}\exp(-i\theta_0/2 - i\Delta k x/2)\right]. \tag{5.37}$$

Here $\psi_\pm$ are the wavefunctions of the ± 1 harmonics before the recombination,

$$n(x) = \frac{3}{8R}\left(1 - \frac{x^2}{R^2}\right), \tag{5.38}$$

$$\theta_0 = (\varphi_+ - \varphi_-) - (\kappa_+ x_+ - \kappa_- x_-) + \frac{g}{2}(x_+^2 - x_-^2) \tag{5.39}$$

and

$$\Delta k = \Delta\kappa - g\Delta x, \tag{5.40}$$

where $\Delta\kappa = \kappa_+ - \kappa_-$ and $\Delta x = x_+ - x_-$. All quantities in Eq. (5.39) are evaluated at the recombination time.

If the density envelopes of the ± 1 harmonics sufficiently overlap at the recombination stage, Eq. (5.37) can be simplified to

$$\psi_0(x) = \sqrt{n(x)}\cos(\theta_0/2 + \Delta k x/2) \tag{5.41}$$

Population of the zero-momentum harmonics N_0 is given by the spatial integration of $|\psi_0|^2$ yielding

$$\frac{N_0}{N_{tot}} = \frac{1}{2}\left(1 + V\cos\theta_0\right), \tag{5.42}$$

where the contrast of the interference fringes V is given by the expression

$$V = \frac{3}{(\Delta kR)^3}[\sin(\Delta kR) - \Delta kR\cos(\Delta kR)]. \tag{5.43}$$

For $\Delta kR \ll 1$, the population of the zero-momentum state is given by the relation

$$N_0/N_{tot} = \cos^2(\theta_0/2).$$

In this limiting case the population depends on the relative accumulated coordinate-independent phase θ_0 between the two BEC clouds and exhibits interference fringes as a function of this phase.

In the opposite case $\Delta kR \gg 1$, the cos function in Eq. (5.41) oscillates several times across the cloud and

$$N_0/N_{tot} = 1/2$$

independently of the value of the relative phase shift.

Equations (5.22) and (5.21) show that both the nonlinearity of the condensate p and the quadratic contribution to the external potential β can result in nonzero values of Δk given by Eq. (5.40) and thus be responsible for the loss of interferometric contrast as illustrated by Fig. 5.2. This figure shows the contrast V defined by the relation $N_0/N_{tot} = (1+V)/2$, where N_0/N_{tot} is the relative population of the zero-momentum harmonics at the end of the interferometric cycle, as a function of the ratio of the cycle time to the initial size of the harmonic T/R_0. The solid line corresponds to the numerical solution of the Gross-Pitaevskii equation (5.6).

The dashed line is given by Eq. (5.43), where ΔkR is calculated with the help of analytical expressions (5.40), (5.21), (5.22) and (5.30).

Since the linear slope of the potential is zero ($\alpha = 0$), $\theta_0 = 0$. Equation (5.43) then predicts that for $\Delta kR = 0$, $V = 1$. As is seen in Fig. 5.2, the contrast indeed equals one for short cycles (small T). Larger values of T correspond to larger interaction times between the two clouds and an increase in ΔkR due to this interaction. As the interaction time increases, the contract V given by Eq. (5.43) goes down from one to small negative value resulting in the values of N_0/N_{tot} slightly below 1/2. At times larger than about $T/R_0 = 1.5$ the two harmonics completely pass each other and stop overlapping during a part of the cycle. The interaction time between the harmonics (the time when they overlap) is now smaller than the cycle time and does not depend on it. The contrast and the population of the zero-momentum harmonic reach their limiting values. Figure 5.3 shows the dependence of the population of the zeroth-order harmonic after the recombination N_0/N_{tot} on the relative accumulated phase shift $\theta_0 = -\alpha T^2/2$. The solid line corresponds to the numerical solution of the Gross-Pitaevskii equation (5.6). The dashed line is Eq. (5.42) with ΔkR given by Eqs. (5.21), (5.22) and (5.30). As is seen in Fig. 5.2, the cycle time $T/R_0 = 4$ corresponds to small negative values of the contrast ($V \approx -0.2$ as given by the Gross-Pitaevskii equation and $V \approx -0.1$ as given by the analytic model). Low values of the contrast result in the washout of the interference fringes shown in Fig. 5.3. It also should be noted that since the contrast V is negative, the symmetric recombination with $\theta_0 = 0$ corresponds not to the maximum, but the minimum population N_0 of the zero-momentum harmonic.

Figures 5.2 and 5.3 demonstrate that recombination with nonzero value of the linear wavevector Δk (see Eq. (5.40)) washes out the interference fringes. Since Δk is a function of time, this effect can be compensated for by conducting the

Figure 5.2: The contrast V versus the cycle time T/R_0 for $R_0 = 500$, $p = 5$, $\alpha = 0$, $g_0 = 0$ and $\beta = 0$.

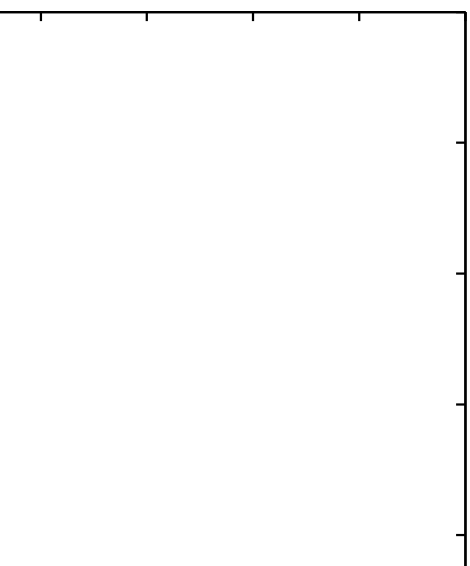

Figure 5.3: Relative population of the zeroth-momentum harmonic N_0/N_{tot} versus the relative accumulated phase $\theta_0 = -\alpha T^2/2$ for $T = 2000$. Other parameters (except nonzero values of α) are as in Fig.5.2.

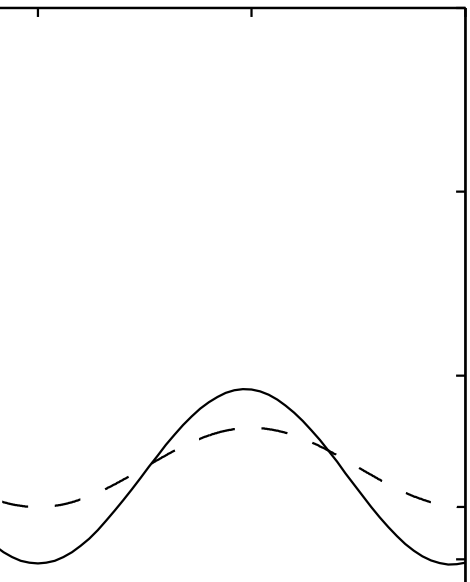

recombination not at the nominal time T but at at a slightly different time $T + \Delta T$ when $\Delta kR = 0$ (in general, ΔT may be both positive and negative). Figure 5.4 shows the contrast $V = 2N_0/N_{tot} - 1$, where N_0/N_{tot} is relative population of the zero-momentum harmonic, as a function of the time ΔT. Negative (positive) values of ΔT correspond to the recombination taking place slightly before (after) the nominal recombination time T. The parameters for Fig. 5.4 are $T = 2000$, $R_0 = 500$ and $p = 5$ with all other parameters being zero. The solid line is the solution of the Gross-Pitaevskii equation and the dashed line is obtained with the help of Eqs. (5.42), (5.21), (5.22) and (5.32). Recombination at the nominal time $\Delta T = 0$ corresponds to a small value of the contrast and a washout of the fringes as is shown in Fig. 5.3. Figure 5.4 indicates that if the recombination takes place at $\Delta T/R_0 \approx -0.2$, the contrast of the fringes becomes much larger. This is confirmed by Fig. 5.5, which shows N_0/N_{tot} versus the relative accumulated phase shift $\theta_0 = -\alpha[(T + \Delta T)^2 - T^2/2]$ for $\Delta/R = -0.2$ and all other parameters the same as in Fig. 5.3. The solid line is the solution of the Gross-Pitaevskii equation and the dashed line is the result of the numerical solution of Eqs. (5.16).

The simple estimate using the condition $(\Delta kR)(T + \Delta T) = 0$ yields

$$\frac{\Delta T}{R_T} = -\frac{(\Delta kR)_T}{R(\Delta kR)'_T}. \tag{5.44}$$

The ratio $\Delta T/R$ gives the relative displacement of the two clouds at the recombination time $T + \Delta T$ since the clouds pass across each other in time R (each cloud has the size $2R$ and the relative speed is 2).

The population of the zero-momentum harmonics depends not only on the magnitude of ΔkR, but on the degree of overlap of the two density envelopes at the recombination time (see (5.37)). Estimate (5.44) takes into account only changes in

Figure 5.4: The contrast $V = 2N_0/N_{tot} - 1$ as a function of $\Delta T/R_0$.

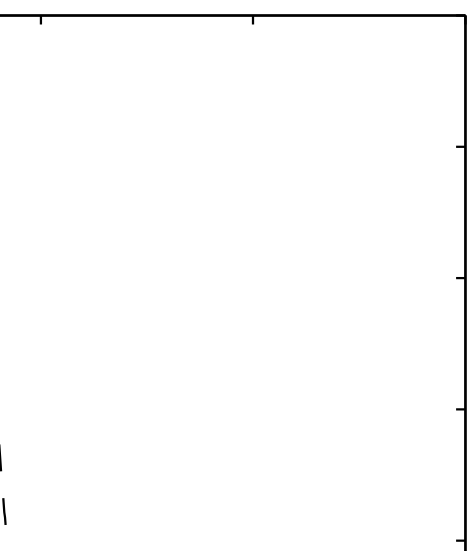

Figure 5.5: Relative population of the zero-order harmonic N_0/N_{tot} versus the relative accumulated phase shift $\theta_0 = -\alpha T^2$ for $T/R_0 = -0.2$. All other parameters are the same as for Fig. 5.3

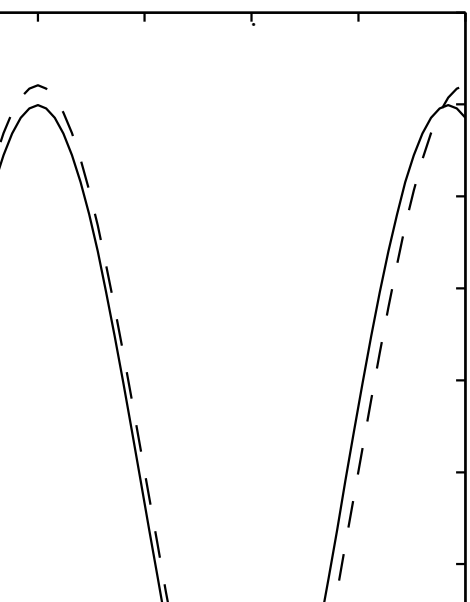

ΔkR but not in the overlap in evaluating ΔT. The last can be taken into account in the framework of Eq. (5.37) at the expense of making formulas more cumbersome and turn out to be not very significant. As we shall see, Eq. (5.44) is in a very good qualitative and quantitative agrement with the results of numerical solution of the Gross-Pitaevskii equation (5.6). Finally it should be mentioned that nonzero values of $\Delta T/R$ mean incomplete overlap and thus the contrast less than one even at the optimized time. The larger is $|\Delta T|/R$, the smaller the contrast. The estimate (5.44) implicitly implies that $|\Delta T|/R \leq 1$ because correction to the recombination time is meaningful only if the clouds overlap at the time $T + \Delta T$. If, for some set of parameters, estimate (5.44) yields $|\Delta T|/R > 1$, the coherence can not be recovered for this set of parameters.

Using the explicit expressions for for (ΔkR) and its time derivative obtained with the help of Eqs. (5.40) and (5.16) results in the relation

$$\frac{\Delta T}{R} = \frac{\Delta\kappa - g\Delta x}{2gR - 3p\Delta x/4R^2}. \tag{5.45}$$

In Equation (5.45), $\Delta\kappa(T)$ and $\Delta x(T)$ are evaluated using Eq. (5.21) and (5.22). The function $g(T)$ should be evaluated using several different expressions depending on the parameters of the problem. For $|\Delta R| \ll R$, $g(T)$ is given by Eq. (5.30). In this case $R_0 = R_T = R$. If $T \gg R_0$, $g(T)$ is given by Eq. (5.32). Since we are assuming that $|\Delta R| \gg R$ at times it takes the clouds to pass through each other, Eqs. (5.30) and (5.32) cover all possible situations. If $|\Delta R|$ is not small as compared to R, the size of the clouds R_T at the end of the cycle should be evaluated by numerical integration of Eq. (5.32).

Equation (5.45) is relatively complex because it covers both the case when the size of the clouds does not change significantly during the cycle and the opposite

limit when the final size is much larger than the initial one. All the relevant physics can be understood by discussing the case $|\Delta R| \ll R$ when Eq. (5.45) acquires especially simple form

$$\frac{\Delta T}{R} = \frac{\Delta\kappa}{2gR} = -\frac{1}{4}\frac{8D_1(\zeta) - (\beta R^3/p)\zeta^2}{3\zeta/4 + D_2(\zeta) + g_0R^2/p - (\beta R^3/p)\zeta}, \tag{5.46}$$

where $\zeta = T/R$.

The contrast at the optimized recombination time can be evaluated by accounting for an incomplete overlap of the clouds using Eq. 5.37 and is given by the approximate expression

$$V \approx 1 - \frac{3}{2}\left(\frac{\Delta T}{R}\right)^2\left[\ln\frac{R}{|\Delta T|} + 2\ln 2 - \frac{1}{2}\right], \tag{5.47}$$

The contrast at the nominal recombination time is given by Eq. (5.43) with

$$\Delta kR = \beta RT^2/2 - 4pD_1(T/R) \tag{5.48}$$

Equations (5.46), (5.47) and (5.48) are the main analytical results of the paper. In Section 5.5, they will be analyzed in several illustrative cases.

5.5 Discussion

5.5.1 Influence of the nonlinearity p for $g_0 = \beta = 0$

For $\beta = g_0 = 0$, Eq. (5.46) becomes

$$\frac{\Delta T}{R} = \frac{-2D_1(T/R)}{D_2(T/R) + 3T/4R} \tag{5.49}$$

Equation (5.49) shows that the correction to the recombination time depends only on the single parameter T/R and does not depend on the nonlinearity of the condensate p (the applicability of the parabolic approximation requires $pR \gg 1$). This is due to the fact that both the $\Delta\kappa$ and the gR terms are proportional to the nonlinearity parameter p. At small values of T/R, $D_1(T/R) \approx (3/8)(T/R)^2$, $D_2(T/R) \approx (3/2)(T/R)$ (cf. Eqs. (5.23) and (5.31)) so

$$\frac{\Delta T}{R} = -\frac{3}{10}\frac{T}{R}, \tag{5.50}$$

i.e., $\Delta T/R$ grows linearly with T/R. The correction to the recombination time $\Delta T/R$ reaches maximum for $T/R \approx 2$ when the duration of the cycle is such that the two clouds at their maximum separation stop overlapping. At longer cycle times $T/R > 2$, both D_1 and D_2 become constants and $\Delta T/R$ starts decreasing inversely proportional to T:

$$\frac{\Delta T}{R} = -\frac{4}{5}\left(\frac{T}{R}\right)^{-1}. \tag{5.51}$$

This behavior has simple physical explanation. The difference between the corrections to the propagation velocities of the clouds $\Delta\kappa$ is due to the nonlinear interaction between the clouds and is accumulated only when the clouds overlap (see the definition of D_1 Eq. (5.23)). For short cycle times $T/R < 2$, when the clouds overlap during all the cycle, the nonlinear effects are accumulated during all times and $\Delta\kappa \propto T^2$. The parabolic phase described by the coefficient $g(T)$ grows linearly with time T, so the correction to the recombination time T is a growing function of the cycle time T. For $T > R$, when the clouds fully separate during the cycle, $\Delta\kappa$ is at its maximum possible value and stops growing further. The quadratic phase profile of each cloud, on the other hand, keeps growing as a function of time, i.e., g becomes larger, thus resulting in the decrease of ΔT.

The dependence of the shift in the recombination time $\Delta T/R_0$ on the cycle time T/R_0 is shown in Fig. 5.6 for $R_0 = 500$ and $p = 5$. The maximum cycle times shown in Fig. 5.6 correspond to the maximum separation of the clouds equal to about ten their diameters. The dots are the results obtained by direct numerical solution of the Gross-Pitaevskii equation (5.6) and the solid line is given by Eq. (5.49). The optimized contrast of the interference fringes V at the recombination time $T+\Delta T$ for the parameters of Fig. 5.7 is shown in Fig. 5.7. The dots correspond to the numerical solution of the Gross-Pitaveskii equation and the solid line is given by Eq. (5.47). For comparison, the dashed line shows the contrast at the nominal recombination time T given by Eqs. (5.43) and (5.48). The lowest values of the optimized contrast $V \approx 0.5$ correspond to intermediate cycle times $T/R_0 \approx 2$ when the maximum separation between the two clouds is equal to their size. Both increasing and decreasing the cycle time T improves the contrast.

Figs. 5.6 and (5.7) show that the operation of the atom Michelson interferometer with the optimization of the recombination time is possible both in the limit $T/2R_0 \leq 1$ when the clouds overlap during all the cycle and in the opposite limit $T/2R_0 \gg 1$ when the clouds are separated most of the time.

5.5.2 Nonzero initial parabolic phase $g_0 \neq 0$

Performing an interferometric cycle with nonzero initial values of the parabolic phase g_0 considerably improves the coherence as compared to the case $g_0 = 0$ provided the sign of g_0 is the same as that of the nonlinearity p. The nonzero initial parabolic phase can be acquired by relaxing the confinement frequency ω of the initial trap and letting the condensate evolve for some time before the start of the interferometric cycle. Dynamics of the BEC in time-dependent parabolic traps in Thomas-Fermi limit has been extensively analyzed (see, e.g. [66, 67, 68]). In the case of 1D

Figure 5.6: The shift in the recombination time $\Delta T/R_0$ as a function of the nominal recombination time T/R_0 for $R_0 = 500$ and $p = 5$. The dots are the results of the numerical solution of the GPE and the solid line is the analytical model.

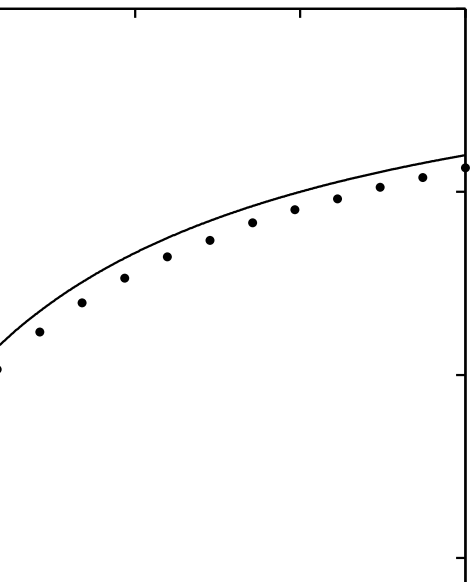

Figure 5.7: Optimized contrast of the interference fringes V for the parameters of Fig. 5.6. The dots are the results of the numerical solution of the GPE and the solid line is the analytical model. The dashed line is the contrast at the nominal recombination time.

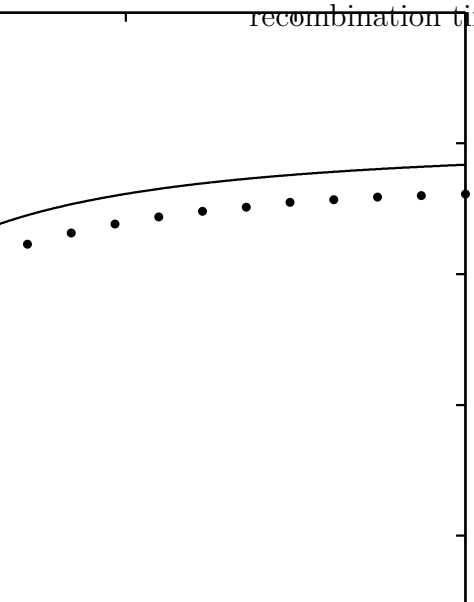

expansion corresponding to our situation, the evolution of $g(\tau)$ and $r = R(\tau)/R(0)$ is described by the set of equations

$$\frac{d^2}{d\tau^2} r = -\omega^2(\tau) r + \frac{\omega^2(0)}{r^2},$$
$$g = \frac{d}{d\tau} \ln r, \tag{5.52}$$

where $\omega(\tau)$ is the trap frequency. The exact value of g depends on the detailed time dependence of $\omega(\tau)$. Changing $\omega(\tau)$ adiabatically slowly leaves the phase of the condensate flat, i.e. $g = 0$. Since we are interested in the maximum possible value of g, we shall consider the limit when the trap frequency is relaxed very fast so that $\omega(\tau) = 0$ for $\tau > 0$. In this limit, g is given by the relation (the condensate's initial phase in the trap is zero):

$$g(r) = \left(\frac{3p}{R_{tr}^3}\right)^{1/2} \left(\frac{r-1}{r^3}\right)^{1/2}, \tag{5.53}$$

where R_{tr} is the initial radius of the condensate in the trap. An extra factor of two in Eq. (5.53) as compared to Eq. (5.32) is due to the fact that the initial condensate is normalized to one whereas the two propagating clouds are normalized to 1/2.

For the given value of R_{tp}, g is maximum for $r = 3/2$. The final size of the condensate after the expansion is the initial size R_0 of the propagating clouds in the interferometric cycle, i.e., $R_0/R_{tr} = 3/2$. The maximum possible value of g_0 is thus given by the relation

$$g_{0,max} = \left(\frac{3p}{2R_0^3}\right)^{1/2}. \tag{5.54}$$

In the following we will use the value $g_0 = s g_{0,max}$ where the coefficient $0 \leq s \leq 1$ accounts for relaxing the trap with finite speed.

The correction to the recombination time $\Delta T/R$ given by the equation (5.46)

with $\beta = 0$ takes the form

$$\frac{\Delta T}{R} = \frac{-2D_1(T/R)}{(3/4)(T/R) + D_2(T/R) + s(3R/2p)^{1/2}} \tag{5.55}$$

If the parameter (R/p) is large, which is typically the case, the corrections to the recombination time are small and the contrast is high. This is illustrated by Fig. 5.8 which shows the shift in the recombination time $\Delta T/R$ as a function of the cycle time T/R using Eq. (5.55). The solid line corresponds to $s = 0$ when the condensate does not have initial parabolic phase. The dashed curve gives $\Delta T/R$ for $s = 0.2$, when the condensate has been allowed to acquire initial parabolic phase. The dots are the results of a numerical solution of the GPE for $s = 0.2$. Figure 5.8 demonstrates that the shift in the recombination time is considerably smaller when the condensate is allowed to expand before the beginning of the cycle. Since the two harmonics have larger overlap at the optimal recombination time, the contrast in the interference fringes is larger when $g_0 \neq 0$.

5.5.3 Nonzero parabolic external potential $\beta \neq 0$

Nonzero values of the parabolic external potential $\beta \neq 0$ can be due to environment or technical imperfections of an experimental apparatus. Equation (5.46) with $\beta \neq 0$ and $g_0 = 0$ yields

$$\frac{\Delta T}{R} = -\frac{1}{4}\frac{8D_1(\zeta) - (\beta R^3/p)\zeta^2}{3\zeta/4 + D_2(\zeta) - (\beta R^3/p)\zeta}, \tag{5.56}$$

where $\zeta = T/R$. The influence of the parabolic potential on the operation of the atom Michelson interferometer is characterized by the parameter $b = \beta R^3/p$. Note that since the term with β in the numerator of Eq. (5.56) is proportional to the square of the cycle time and the denominator grows linearly with time, even small values of b for long enough cycles will always result in a complete loss of coherence.

Figure 5.8: The shift in the recombination time $\Delta T/R$ as a function of the cycle time T/R given by Eq. (5.55) for $s = 0$ (solid) and $s = 0.2$ (dashed curve). The dots are the numerical soloution of the GPE with $s = 0.2$. For all three curves $R/p = 100$.

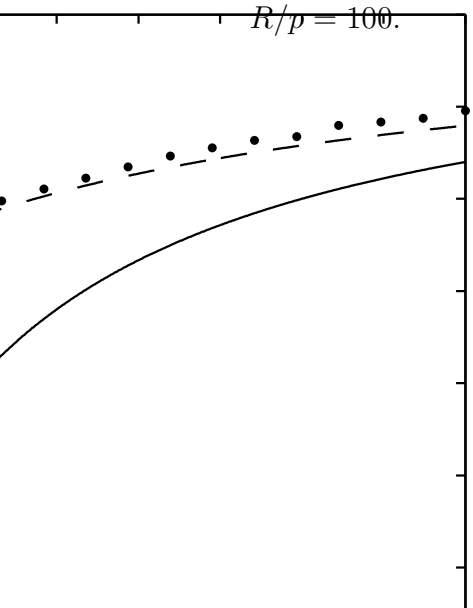

In the limit of short cycle times $\zeta \ll 1$, Eq. (5.55) takes the form

$$\frac{\Delta T}{R} = -\frac{\zeta}{4}\frac{3-b}{5/2-b}. \tag{5.57}$$

Equation (5.57) is similar to Eq. (5.50) but the sign of ΔT can be both negative and positive depending on the value of b. The second difference is in that the coefficient multiplying ζ may become so large for positive values of $b \approx 5/2$, that coherence will be lost even for short cycle times. Negative values of β are preferable because they ensure the operation of the interferometer at least for short times $T/R \leq 1$. If the value of β is controlled at the level $b \ll 1$, the operation of the interferometer is possible for $\Delta T/R < 1$ and any sign of β.

In the limit $\zeta > 2$, Eq. (5.56) becomes

$$\frac{\Delta T}{R} = -\frac{12/5 - b\zeta^2}{(3-4b)\zeta}. \tag{5.58}$$

If $|b| \ll 1$, the optimized contrast will be high in the range

$$2 \leq \frac{T}{R} \ll \frac{1}{|b|}. \tag{5.59}$$

If $|b| \geq 1$, the coherence in general will be lost for $T/R > 2$.

5.5.4 Recombination at a different wavelength

The contrast of the interference fringes can be improved by conducting the recombination with optical pulses having different wavelength as compared to the splitting pulse to compensate for the change in the wave vectors of the moving clouds. The relative change in the wavelength of the recombining pulse $\Delta\lambda/\lambda$ as compared to

the separation pulse is given by the expression (cf. Eq. (5.21))

$$\frac{\Delta\lambda}{\lambda} = -\Delta\kappa = -\frac{\beta}{2}T^2 + \frac{4p}{R}D_1(T/R). \tag{5.60}$$

As has been discussed in the introduction, the repulsive nonlinearity results in the speeds v of the moving harmonics $\psi_\pm$ being smaller than the speed v_0 imparted by the separation pulse. The recombination then should be performed with beams of larger wavelength. Similarly, for $\beta < 0$ (a potential hump) $\Delta\lambda > 0$ and for $\beta > 0$ (a potential trough) $\Delta\lambda < 0$. The optimized contrast is determined by the relation

$$V \approx 1 - \frac{3}{2}\left(\frac{\Delta x}{2R}\right)^2 \left[\ln\frac{2R}{|\Delta x|} + 2\ln 2 - \frac{1}{2}\right], \tag{5.61}$$

where Δx is the separation between the centers of the harmonics $\psi_\pm$ at the recombination time given by Eq. (5.22). In a typical situation, $|\Delta x|/R \ll 1$ and the optimized contrast is close to one.

Chapter 6

Theoretical analysis of single and double reflection atom interferometers in a confining magnetic trap

6.1 Introduction

A promising method for building an atom interferometer has been demonstrated by several groups [33, 34, 43]. This method uses a standing light wave to manipulate a Bose-Einstein condensate (BEC) that is confined in a waveguide with a weak trapping potential along the guide.

The trajectories of the BEC clouds during the interferometric cycle are shown in Fig. 6.1 (a). The cycle of duration T starts at $t = 0$ by illuminating the motionless BEC with the wave function ψ_0 with a splitting pulse from the two counterpropagating laser beams. This pulse acts like a diffraction grating splitting the initial BEC cloud into two harmonics ψ_+ and ψ_-. The atoms diffracted into the $+1$ order absorb a photon from a laser beam with the momentum $\hbar k_l$ and re-emit it into the beam with the momentum $-\hbar k_l$ acquiring the net momentum of $2\hbar k_l$. The harmonic ψ_+ starts moving with the velocity $v_0 = 2\hbar k_l/M$, where k_l is the wavenumber of the laser beams and M is the atomic mass. Similarly, the harmonic ψ_- starts moving with the velocity $-v_0$. The two harmonics are allowed to propagate until the time $t = T/2$. At this time the harmonics are illuminated by a reflection optical pulse. The atoms in the harmonic ψ_+ change their velocity by $-2v_0$ and those in the harmonic ψ_- by $2v_0$. The harmonics propagate until the time $t = T$ and are subject to the action of the recombination optical pulse. After the recombination, the atoms in general populate all three harmonics ψ_0 and $\psi_\pm$. The relative population of the harmonics depend on the phase difference between the harmonics $\psi_\pm$ acquired during the interferometric cycle. By counting the number of atoms in each harmonic the phase difference can be determined. This type of an interferometer will be referred to as a single reflection interferometer.

The first experiments using this type of interferometer were done by Wang et

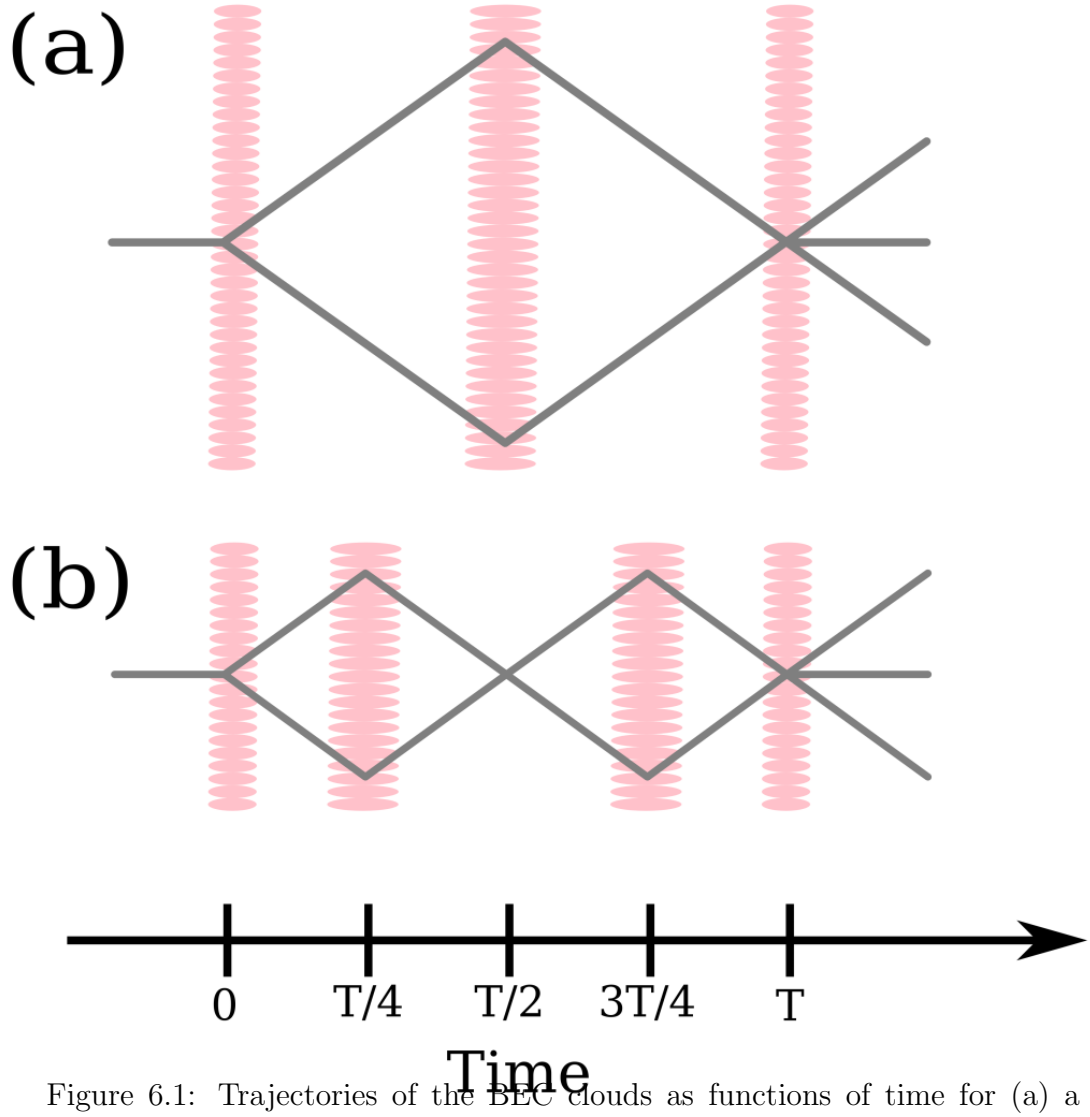

Figure 6.1: Trajectories of the BEC clouds as functions of time for (a) a single reflection interferometer and (b) a double reflection interferometer. Vertical wavy bands show timing of the optical pulses.

al. [33]. Good contrast of the interference fringes was observed for cycle times not exceeding about 10 ms. This fact was theoretically explained by Olshanii et al. [44]. The authors of Ref. [44] attributed the loss of contrast to a distortion of the phase across each harmonic that was caused by both the atom-atom interactions and the residual potential along the waveguide.

A simple way to understand the reason for the loss of contrast is to consider the effect of the two forces acting on the harmonics $\psi_{\pm}$ during the interferometric cycle. The first force is due to a repulsive nonlinearity between the two BEC clouds, as shown in Fig. 6.2 (a). This force exists only when the two harmonics overlap. The second force is exerted by the trapping potential along the waveguide and pushes the harmonics toward the center of the trap as shown in Fig. 6.2 (b). As a result, the velocities of the harmonics are not equal to their initial values $\pm v_0$ during the interferometric cycle.

Consider, for example, the ψ_+ harmonic. Just before the reflection pulse its velocity is $v_0 + \delta v$. Since the reflection pulse changes the speed of each harmonic by $2v_0$, just after the reflection pulse the velocity of the ψ_+ harmonic becomes $-v_0 + \delta v$. Because of this fact, when the harmonic moves back to the center of the trap, its velocity before the recombination is not equal to $-v_0$. The change in the speeds of the harmonics during the first and the second halves of the interferometric cycle has two consequences. First, harmonics do not completely overlap at the nominal recombination time. Second, the recombination optical pulse is unable to exactly cancel the harmonics' velocities causing the recombined wave functions to have coordinate-dependent phases across the clouds. Both mechanisms result in a washout of interference fringes and loss of contrast.

A modification of the single-pass interferometer interferometer shown in Fig. 6.1 (b), was built by Garcia et al. [34]. The interferometric cycle begins by illuminating

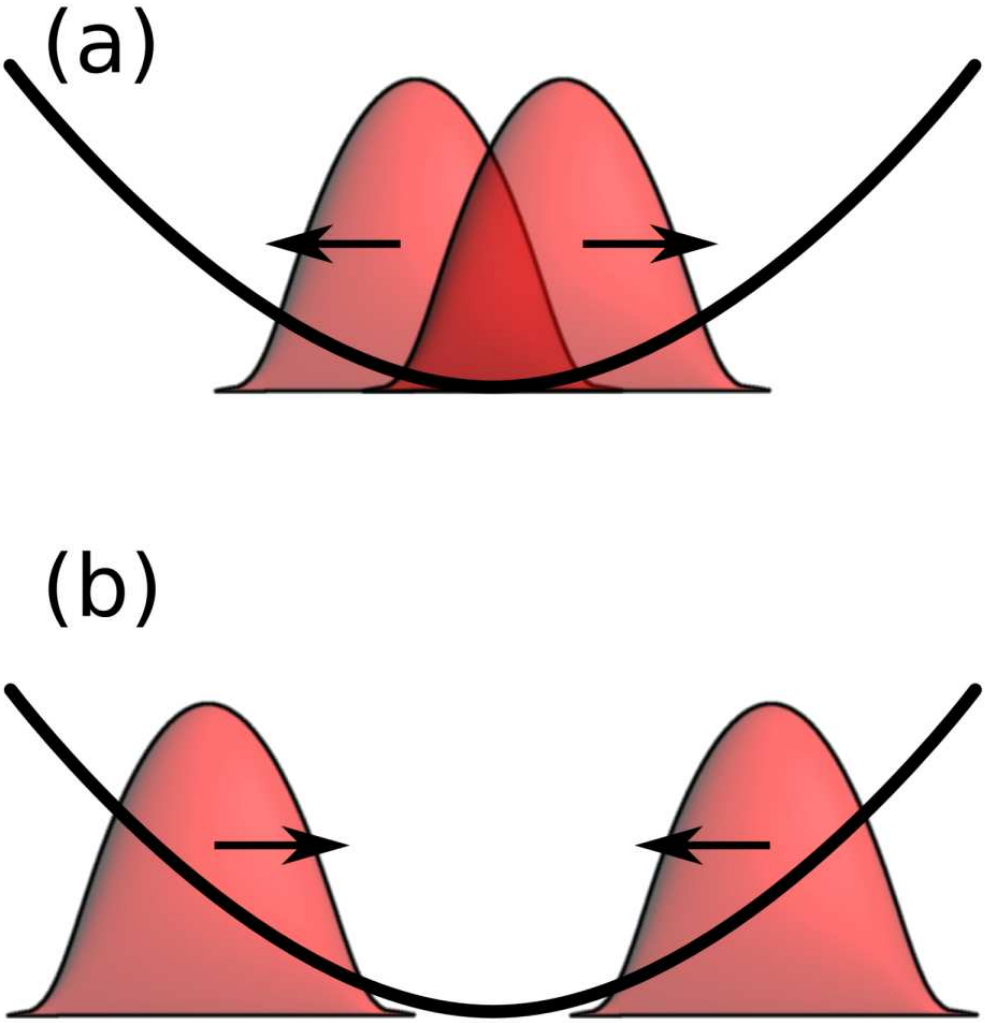

Figure 6.2: The two different forces acting on the two harmonics during the interferometric cycle. (a) When the two harmonics overlap, the atom-atom interactions cause a repulsive force between the harmonics and (b) the external potential exerts a force pushing the two harmonics towards the center of the trap.

the BEC with a splitting pulse. The two harmonics freely propagate until the time $t = T/4$ when they are illuminated by a reflection pulse. They continue to freely propagate until the time $t = 3T/4$ when a second reflection pulse is applied. The harmonics freely propagate until the time $t = T$ when they overlap and are subject to the action of the recombination pulse. This type of an interferometer will be referred to as a double reflection interferometer. The coherence time demonstrated in Ref. [34] exceeded 44 ms. More recently, the coherence time of this interferometer has been extended to over 80 ms [69]. The advantage of a double reflection interferometer over a the single reflection one is in that the shift in the velocity of the harmonics is considerably reduced allowing for larger cycle times. Recently this type of interferometer was used to measure the ac Stark shift [70].

Along with the experimental realization of the single and double reflection interferometer, the authors of Ref. [69] developed a theoretical model to describe its operation. The model presented in this chapter differs from that of Ref. [69] by accounting for the effects of atom-atom interactions, the change in the BEC size during the cycle time, and the incomplete overlap of the two harmonics at the recombination time. These effects do not significantly change the results of analysis of Ref. [69] for the single reflection interferometer. However, our results for the double reflection interferometer are of a different functional form than those found in Ref. [69].

In the rest of this chapter, we use a simple analytic model to calculate the momentum and the degree of overlap of the two harmonics at the end of the cycle for both the single and double reflection interferometers. Both of these depend on the time that the two harmonics spend overlapping, the total cycle time and the frequency of the trap. Next, we find the regions of a large and a small interference fringe contrast for both the single and double reflection interferometers. We

demonstrate that, with a double reflection interferometer, the coherence time can be increased by shifting the recombination time. Finally, we compare the model with recent experimental realizations of these interferometers.

6.2 Analytical model

The dynamics of a BEC in a waveguide will be analyzed in the framework of the Gross-Pitaevskii equation (GPE)

$$i\frac{\partial}{\partial\tau}\psi(x,\tau) = \left[-\frac{1}{2}\frac{\partial^2}{\partial x^2} + v(x) + \Omega(\tau)\cos x + p|\psi|^2\right]\psi(x,\tau), \tag{6.1}$$

which has been obtained by projecting the three-dimensional GPE onto the strongly confining transverse mode of the waveguide (for more details see [52]). In Eq. (6.1), ψ is the wave function of the BEC normalized to one, the dimensionless coordinate x is measured in units of $x_0 = 1/2k_l$ and the dimensionless time τ is measured in units of $t_0 = M/4\hbar k_l^2$, where k_l is the wave vector of the lasers and M is the atomic mass.

The weakly confining potential along the guide is harmonic

$$v(x) = \frac{1}{2}\omega^2 x^2, \tag{6.2}$$

and $\Omega(\tau)\cos x$ is the potential associated with the laser beams. The strength of interatomic interaction is given by the parameter

$$p = a_s N/a_\perp^2 k_l, \tag{6.3}$$

where a_s is the s-wave scattering length, N is the total number of atoms in the

BEC, $a_\perp = \sqrt{\hbar/M\omega_\perp}$ is the transverse harmonic oscillator length, and $\omega_\perp$ is the transverse frequency of the guide.

The optical potential $\Omega(\tau)\cos x$ acts as a diffraction grating for the BEC wave function ψ. This grating diffracts the BEC into several harmonics separated by multiples of the grating wave vector:

$$\psi = \sum_n \psi_n e^{inx}, \tag{6.4}$$

where ψ_n are the slowly-varying amplitudes of the harmonics' wave functions.

The dynamics of the BEC due to the optical potential has been discussed in Refs. [43, 34, 52]. Since the optical pulses used to manipulate the BEC are intense and short their action can be described by simple mixing matrices operating on the harmonics ψ_n in Eq. (6.4). The splitting pulse transforms the initial zero-momentum harmonic ψ_0 into the two harmonics with $n = \pm 1$: $\psi_0 \to (\psi_{+1} + \psi_{-1})/\sqrt{2}$. The reflection pulse transforms the $n = \pm 1$ harmonic into the $n = \mp 1$ harmonic: $\psi_{\pm 1} \to \psi_{\mp 1}$. Finally, after the recombination pulse, the BEC consists of three harmonics with $n = -1, 0, +1$. The population in the zero momentum harmonic ψ_0 depends on the relative phase shift of the ± 1 harmonics immediately before the recombination.

Between the splitting and the recombination optical pulses, the BEC consists of two harmonics with $n = \pm 1$. In the Thomas-Fermi approximation, the evolution of these harmonics is governed by the set of equations

$$\begin{aligned}
\left(\frac{\partial}{\partial\tau} \pm \frac{\partial}{\partial x}\right) n_\pm &= -\frac{\partial}{\partial x}\left(n_\pm \frac{\partial\phi_\pm}{\partial x}\right), \\
\left(\frac{\partial}{\partial\tau} \pm \frac{\partial}{\partial x}\right) \phi_\pm &= -\frac{1}{2}\left(\frac{\partial\phi_\pm}{\partial x}\right)^2 - v - p(n_\pm + 2n_\mp),
\end{aligned} \tag{6.5}$$

where $n_\pm$ and $\phi_\pm$ are densities and phases of the harmonics introduced by the

relations

$$\psi_{\pm 1} = \sqrt{n_\pm}\exp(i\phi_\pm). \tag{6.6}$$

Equations (6.5) are valid when $pR \gg 1$, where p is the dimensionless nonlinearity parameter and R is the characteristic size of the harmonics.

The set of partial differential equations Eqs. (6.5) can be transformed into a set of ordinary differential equations by parametrizing the density and phase of the harmonics as

$$\begin{aligned} n_\pm &= \frac{3}{8R}\left[1 - \frac{(x-x_\pm)^2}{R^2}\right], \\ \phi_\pm &= \varphi_\pm + \kappa_\pm(x-x_\pm) + \frac{g}{2}(x-x_\pm)^2 + \frac{1}{6}s_\pm(x-x_\pm)^3. \end{aligned} \tag{6.7}$$

Functions R, $x_\pm$, $\varphi_\pm$, $\kappa_\pm$, g, and $s_\pm$ depend only on time. The radius of each of the harmonics is R. The position of each harmonics's center of mass is given by the coordinate $x_\pm$. The coordinate-independent part of the phase of each harmonic is $\varphi_\pm$. The correction to the wave vector of each harmonic is $\kappa_\pm$ and the curvature of the phase is given by the parameter g. Finally, the parameter $s_\pm$ determines the size of the cubic contribution to the phase.

Using Eqs. (6.7) in Eqs. (6.5) results in a set of ordinary differential equations for the parameters R, $x_\pm$, $\varphi_\pm$, $\kappa_\pm$, g. These equations are

$$\begin{aligned} R' &= gR, \\ x'_\pm &= \pm 1 + \kappa_\pm, \\ \kappa'_\pm &= -\omega^2 x_\pm \pm \frac{\omega^2 R_0^3}{4R^2}d_1(q), \\ g' &= -g^2 - \omega^2 + \frac{\omega^2 R_0^3}{2R^3}[1 + d_2(q)], \\ s'_\pm &= \frac{6}{2}\frac{\omega^2 R_0^3}{2R^4}d_3(q), \end{aligned}$$

$$\varphi'_{\pm} = \frac{1}{2}\kappa_{\pm}^2 - \frac{1}{2}\omega^2 x_{\pm}^2 + \frac{\omega^2 R_0^3}{4R}[1 + d_0(q)]. \tag{6.8}$$

Here

$$\begin{aligned}
d_0 &= \left(2 - \frac{7}{2}|q|^2 + 2|q|^3 - \frac{1}{8}|q|^5\right)\theta(|q| < 2), \\
d_1 &= q\left(4 + \frac{15}{2}|q| - \frac{35}{2}|q|^2 + \frac{65}{8}|q|^3 - \frac{7}{16}|q|^5\right)\theta(|q| < 2), \\
d_2 &= \left(2 - \frac{15}{2}|q|^2 + 5|q|^3 - \frac{3}{8}|q|^5\right)\theta(|q| < 2), \\
d_3 &= q\left(-\frac{35}{2}|q| + \frac{175}{6}|q|^2 - \frac{105}{8}|q|^3 + \frac{35}{48}|q|^5\right)\theta(|q| < 2),
\end{aligned} \tag{6.9}$$

and $q = (x_+ - x_-)/R$ is the relative displacement of the two harmonics. The θ function in Eq. (6.9) is equal to one if its argument is a logical true and zero if it is a logical false. The nonlinearity parameter p was eliminated from Eqs. (6.8) with the help of the relation

$$p = \frac{2}{3}\omega^2 R_0^3, \tag{6.10}$$

where R_0 is the initial size of the BEC cloud (equal to the size of the both harmonics immediately after the splitting pulse). Equation (6.10) assumes that the BEC is created in the confining potential Eq. (6.2).

The procedure of deriving Eqs. (6.8) parallels that given in [52]. Equations (6.8) and (6.9) differ from those found in Ref. [52] by accounting for an additional cubic term.

Since the BEC is in the lowest stationary state of the trap before the splitting pulse, the initial conditions for Eqs. (6.8) are $R(\tau = 0) = R_0$, and $x_{\pm}(\tau = 0) = \kappa_{\pm}(\tau = 0) = g(\tau = 0) = \varphi_{\pm}(\tau = 0) = 0$. The reflection pulses are accounted for by the boundary conditions at the time of the reflections: $x_{\pm} \to x_{\mp}$ and $\kappa_{\pm} \to \kappa_{\mp}$.

After the recombination pulse the BEC consists of three harmonics ψ_0 and $\psi_{\pm}$.

The population of the zero-momentum harmonic is given by the expression

$$N_0 = \frac{1}{2}\left[1 + V\cos\Delta\varphi\right], \tag{6.11}$$

where $\Delta\varphi = \varphi_+ - \varphi_-$ is the relative phase difference between the harmonics.

The fringe contrast V is given by the relation

$$V = \frac{3}{2}\int_0^{1-|\Delta x|/2R} dy \left[\left(1 - y^2 + \frac{(\Delta x)^2}{4R^2}\right)^2 - \frac{(\Delta x)^2}{R^2}\right]^{1/2} \cos(\Delta k R y + \frac{1}{6}\Delta s R^3 y^3). \tag{6.12}$$

Here

$$\Delta k = \Delta\kappa - g\Delta x + \frac{1}{8}\Delta s(\Delta x)^2, \tag{6.13}$$

$\Delta x = x_+ - x_-$, $\Delta\kappa = \kappa_+ - \kappa_-$ and $\Delta s = s_+ - s_-$.

When the fringe contrast is high ($1 - V \ll 1$), Eq. (6.12) can be simplified to

$$\begin{aligned} V &\approx 1 - \frac{3}{2}\left(\frac{\Delta x}{2R}\right)^2 \left[\ln\left|\frac{2R}{\Delta x}\right| + 2\ln 2 - \frac{1}{2}\right] \\ &- \frac{1}{10}\left(\Delta k R + \frac{1}{14}\Delta s R^3\right)^2 - \frac{1}{6615}(\Delta s R^3)^2 \\ &= 1 - A - B - C, \end{aligned} \tag{6.14}$$

where $0 \le A, B, C \ll 1$.

The expression for the fringe contrast V given by Eq. (6.14) contains three terms A, B, and C. All these terms are positive and decrease the fringe contrast additively. In the following analysis their influence will be considered separately. The boundary between the regions of high and low fringe contrast will be defined by the conditions $A \sim 1/2$, or $B \sim 1/2$, or $C \sim 1/2$. Despite the fact that Eq. (6.14) was obtained in the limit $A, B, C \ll 1$, these conditions turn out to be good qualitative and quantitative approximations.

The term

$$A = \frac{3}{2}\left(\frac{\Delta x}{2R}\right)^2 \left[\ln\left|\frac{2R}{\Delta x}\right| + 2\ln 2 - \frac{1}{2}\right] \tag{6.15}$$

describes the decrease in the fringe contrast due to the incomplete overlap of the two harmonics at the recombination time. The region of low contrast due to the incomplete overlap is given by the condition

$$|\Delta x|/R < 1 \tag{6.16}$$

(the harmonics overlap by less than half of their their full widths).

The term

$$B = \frac{1}{10}\left(\Delta k R + \frac{1}{14}\Delta s R^3\right)^2 \tag{6.17}$$

describes the loss of fringe contrast due to the phase difference between the center and the periphery of the cloud ψ_0. The region of low fringe contrast is given by the relation

$$\left|\Delta k R + \frac{1}{14}\Delta s R^3\right| < \sqrt{5} \sim 2. \tag{6.18}$$

The phase difference in Eq. (6.17) is due to a combination of both the quadratic and the cubic terms in the expression for the phase (6.7). These terms have been grouped together in Eq. (6.17) because it is sometimes possible to set $B = 0$ by shifting the recombination time, as will be shown in Sec. 6.4. However, even when $B = 0$, there are higher order phase distortions that can cause a loss of fringe contrast due to the presence of the cubic term in the phase Eq. (6.7). The effect of this cubic term on the fringe contrast is given by the parameter

$$C = \frac{1}{6615}(\Delta s R^3)^2. \tag{6.19}$$

This term results in a small fringe contrast when

$$|\Delta s|\, R^3 < \sqrt{6615/2} \sim 60. \tag{6.20}$$

Each of the three above-discussed contributions to the Eq. (6.14) can be expressed in terms of three dimensionless parameters having a simple physical meaning. The first parameter is the dimensionless trapping frequency

$$\omega = \omega_{\parallel} t_0, \tag{6.21}$$

The second parameter is the product of the interferometric cycle time and the trapping frequency

$$\omega T = \omega_{\parallel} T_D \tag{6.22}$$

where ω and T_D are the dimensional trap frequency and the cycle time, respectively.

The third parameter is the product of the dimensionless initial size of the BEC R and the trapping frequency ω. This parameter can be written in terms of dimensional quantities as

$$\omega R = \frac{\omega_{\parallel} R_D}{v_0}, \tag{6.23}$$

where R_D is the dimensional radius of the BEC and $v_0 = 2\hbar k_l / M$ is the speed of the harmonics just after the splitting pulses. This parameter is the time it takes the two harmonics to separate measured in units of the inverse trapping frequency.

6.3 Single reflection interferometer

Solutions of Eqs. (6.8) for the case of a single reflection interferometer shown in Fig. 6.1 (a) have been previously discussed in [52] without the cubic phase term.

Inclusion of this term (Δs) is somewhat cumbersome but straightforward and results in the following expressions for R, Δx, $\Delta\kappa$, g and Δs at the end of the interferometric cycle of duration T:

$$\begin{aligned} R &= R_0[1-\frac{1}{4}(\omega T)^2], \\ \Delta x &= \frac{1}{4\omega}(\omega T)^3, \\ \Delta\kappa &= \frac{1}{2}(\omega T)^2 - 2(\omega R_0)^2 D_1(\omega T/\omega R_0), \\ g &= -\omega[\omega T - 2\omega R_0 D_2(\omega T/\omega R_0)], \\ \Delta s &= 2\omega^2 D_3(\omega T/\omega R_0). \end{aligned} \tag{6.24}$$

Here

$$D_1(x) = \begin{cases} \frac{1}{4}x^2(2+\frac{5}{2}x-\frac{35}{8}x^2+\frac{13}{8}x^3-\frac{1}{16}x^5) & , \quad x<2 \\ 1/2 & , \quad x>2 \end{cases}, \tag{6.25}$$

$$D_2(x) = \begin{cases} \frac{1}{4}x\left(2-\frac{5}{2}x^2+\frac{5}{4}x^3-\frac{1}{16}x^5\right) & , \quad x<2, \\ 0 & , \quad x>2. \end{cases}, \tag{6.26}$$

and

$$D_3(x) = \begin{cases} \frac{3}{2}x^3\left(\frac{35}{6}-\frac{175}{24}x+\frac{21}{8}x^2-\frac{5}{48}x^4\right) & , \quad x<2, \\ 1 & , \quad x>2. \end{cases} \tag{6.27}$$

In deriving the above expressions, only the lowest order contributions in terms of ωT and ωR were retained. The loss of the fringe contrast takes place when both these parameters are still small. The first of Eq. (6.24) then shows that the relative change in the size of the BEC during the cycle is small and will be neglected in the subsequent analysis.

The loss of the contrast due to the term A Eq. (6.15) happens for $A > 1/2$.

Using Eqs. (6.16) and (6.24), we can translate this inequality into the relation

$$\frac{1}{4}\frac{(\omega T)^3}{\omega R} > 1. \tag{6.28}$$

Similarly, the loss of the contrast due to the term B Eq. (6.17) with the help of Eqs. (6.18) and (6.24) can be expressed as

$$\left\{\frac{1}{2}(\omega T)^2 - 2(\omega R)^2\left[D_1(\omega T/\omega R) - \frac{1}{14}D_3(\omega T/\omega R)\right]\right\}\frac{\omega R}{\omega} > 5, \tag{6.29}$$

where D_1 and D_3 are given by Eqs. (6.25) and (6.27) respectively.

Finally, the loss of the fringe contrast due to the term C corresponds to the region of parameters where

$$\frac{(\omega R)^3}{\omega}D_3(\omega T/\omega R) > 30. \tag{6.30}$$

Figure 6.3 is a two-dimensional plot showing the regions of operation of the interferometer. The dimensionless trap frequency is $\omega = 3.5 \times 10^{-5}$, which roughly corresponds to the value used in recent experiments [69]. The white region corresponds to large fringe contrast. In the grey region (lower right corner) $A > 1/2$ and the fringe contrast is small because of the lack of overlap of the harmonics $\psi_\pm$. The region with the vertical stripes corresponds to $B > 1/2$ and the contrast is small because of the phase difference across the cloud. The region filled with the horizontal stripes corresponds to $C > 1/2$ and the contrast is lost because of large value of the cubic phase across the harmonic. These regions were found by numerically inverting Eqs. (6.28), (6.29), and (6.30). Note that when two shaded regions overlap, the contrast is lost due to two different mechanisms.

Figure 6.3 shows that when $\omega R < 5 \times 10^{-3}$, the contrast is lost because the two

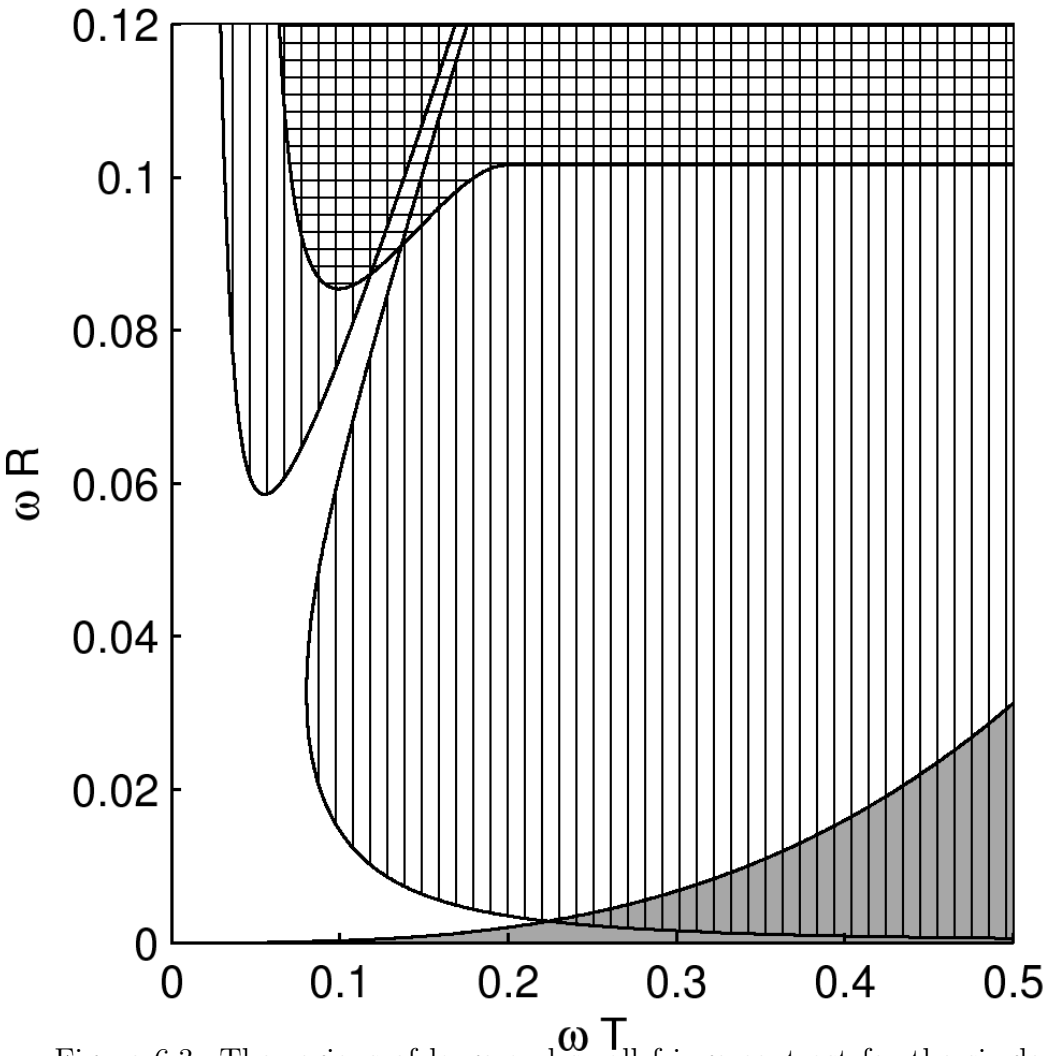

Figure 6.3: The regions of large and small fringe contrast for the single reflection interferometer. The white region corresponds to high contrast. In the grey region $A > 1/2$, the region filled with vertical stripes is where $B > 1/2$. The region filled with horizontal stripes is where $C > 1/2$.

harmonics $\psi_{\pm}$ do not overlap at the recombination time. In the region $5 \times 10^{-3} < \omega R < 6 \times 10^{-2}$, the contrast is lost because the trap causes a difference in the phase across the atomic cloud. When $\omega R > 6 \times 10^{-3}$ and $\omega T < \sqrt{2}\omega R$, the force that the two harmonics exert on each other is the cause of the difference in phase across the harmonics. For the cycle time $\omega T = \sqrt{2}\omega R$, there is no phase difference across the harmonics, but for $\omega T > 0.12$ the cubic phase across the recombined harmonic causes a loss of fringe contrast. For $\omega R > 0.06$ and $\omega T > \sqrt{2}\omega R$ the trap causes the loss of fringe contrast.

The boundary between the regions where $A < 1/2$ and $A > 1/2$ is given by the relation

$$\omega R = \frac{1}{4}(\omega T)^3. \tag{6.31}$$

For a given value of ωT, Eq. (6.31) sets the lower limit on the parameter ωR for which the fringe contrast is large.

The boundary between the regions where $B < 1/2$ and $B > 1/2$ obtained with the help of Eq. (6.18) in the limit $\omega R \ll 1$, is given by the relation

$$\omega R = \frac{4\omega}{(\omega T)^2}. \tag{6.32}$$

For a given ωT, Eq. (6.32) is the upper limit on the parameter ωR for which the fringe contrast is large.

The largest cycle times with high fringe contrast correspond to the point on Fig. 6.3 where the grey and vertical striped regions meet. Eqs. (6.31) and (6.32) show that the maximum cycle time is given by

$$\omega T_{max} = (16\omega)^{1/5} \tag{6.33}$$

and this occurs when the size of the BEC is given by the relation

$$\omega R_{opt} = \frac{1}{4}(16\omega)^{3/5}. \tag{6.34}$$

The optimal value of the parameter ωR_{opt} is always smaller than ωT_{max}, which justifies the approximation used in deriving Eq. (6.32).

In the previous chapter (Chapter 5), we demonstrated that it is sometimes possible to increase the contrast of the interference fringes by shifting the recombination time. However, in the geometry of a single-reflection interferometer when the BEC is created in the confining potential given by Eq. (6.2), it is not possible to significantly increase the fringe contrast by shifting the recombination time for $\omega T/\omega R > 2$, i.e., for the cycle times such that the two clouds completely separate. As a result, the regions depicted in Fig. 6.3 cannot be significantly changed by shifting the recombination time.

6.4 Double reflection interferometer

For the geometry of the double reflection interferometer shown in Fig.6.1 (b), expressions for R and g were found by perturbatively solving Eqs. (6.8) to third order in ωT and first order in ωR yielding

$$\begin{aligned} g &= \omega\left[-\frac{1}{2}(\omega T) + \frac{1}{24}(\omega T)^3 + \frac{1}{4}(\omega R) D_2\left(\frac{\Delta x}{R}\right)\right], \\ R &= R_0\left[1 - \frac{1}{4}(\omega T)^2\right]. \end{aligned} \tag{6.35}$$

The equation for R shows that, as for the single reflection interferometer, the relative change in the size of the BEC during the cycle is small. This change will be neglected in the subsequent analysis.

Solutions of Eqs. (6.8) results in the expressions for Δx and $\Delta\kappa$ at the end of the interferometric cycle that are given by

$$\begin{aligned}\Delta x &= \frac{2}{\omega}\left[2\sin\frac{\omega T}{4} - 2\sin\frac{3\omega T}{4} + (1+I_s)\sin\omega T\right], \\ \Delta\kappa &= 4\cos\frac{\omega T}{4} - 4\cos\frac{3\omega T}{4} + 2(1+I_s)\cos\omega T - 2 + 2I_r. \end{aligned} \tag{6.36}$$

Here

$$I_s = \frac{1}{4}(\omega R)^2 \tag{6.37}$$

is the change in $\Delta\kappa$ caused by the repulsive force that the two harmonics exert on each other during the separation and

$$I_r = \frac{1}{2}(\omega R)^2\left[D_1(|\Delta x|/R) - \frac{1}{2}\right] \approx -\frac{1}{4}(\omega R)^2\left[1 - \left(\frac{\Delta x}{R}\right)^2\right] \tag{6.38}$$

is the change in $\Delta\kappa$ caused by the force that the two harmonics exert on each other during the recombination, with D_1 given by Eq. (6.25). Expanding Eq. (6.36) into into a Taylor series and keeping up to the sixth order in ωT results in the relations

$$\begin{aligned}\Delta x &= \frac{2}{\omega}\left[\frac{1}{4}(\omega R)^2(\omega T) - \frac{1}{32}(\omega T)^3 + \frac{9}{2048}(\omega T)^5\right], \\ \Delta\kappa &= \frac{1}{2}(\omega R)^2\left[\left(\frac{\Delta x}{R}\right)^2 - \frac{1}{2}(\omega T)^2\right] + \frac{1}{32}(\omega T)^4 - \frac{11}{6144}(\omega T)^6. \end{aligned} \tag{6.39}$$

The first term in Eq. (6.38) is canceled by Eq. (6.37) and the incomplete overlap at the recombination time has a larger effect than the change in the harmonics' size R.

Finally, Δs is given by the expression

$$\Delta s = -\omega^2\left[1 + \left(\frac{R_0}{R}\right)^3 (D_3(|\Delta x|/R) - 1)\right], \tag{6.40}$$

where D_3 is given by Eq. (6.27). Here, the change in the size of the harmonics R has a larger effect on Δs than the incomplete overlap at the recombination time. In the limit where the change in R is small and using Eq. (6.35), reduces Eq. (6.40) to

$$\Delta s = -\omega^2 \frac{3}{4}(\omega T)^2. \tag{6.41}$$

The loss of contrast due to the term A Eq. (6.15) occurs when $A > 1/2$. Using Eq. (6.16) and (6.39), we can translate this inequality into the relation

$$\frac{1}{16}\frac{(\omega T)^3}{\omega R} > 1. \tag{6.42}$$

Similarly, the loss of contrast due to B Eq. (6.17) is given by Eq. (6.18) and Eq. (6.13), which is the sum of three terms. The first term is

$$\Delta\kappa = \frac{1}{32}(\omega T)^4 + \frac{1}{6144}(\omega T)^6 - \frac{3}{8}(\omega R)^2(\omega T)^2. \tag{6.43}$$

The second term is the product of the distance between the two harmonics and the quadratic contribution to the phase at the recombination time and may be expressed as

$$g\Delta x = \frac{1}{32}(\omega T)^4 - \frac{9}{2048}(\omega T)^6 - \frac{1}{4}(\omega R)^2(\omega T)^2. \tag{6.44}$$

The third term is the cubic contribution given by

$$\Delta s R^3 = \frac{3}{4\omega}(\omega T)^2(\omega R)^3. \tag{6.45}$$

Adding Eq. (6.43), (6.44), and (6.45), the inequality $B > 1/2$ can be translated into the relation

$$\left|\frac{1}{192}(\omega T)^6 - \frac{1}{14}(\omega R)^2(\omega T)^2\right| \frac{\omega R}{\omega} > 2. \tag{6.46}$$

The region were the loss of contrast is caused by C can be found using Eqs. (6.45) and (6.20) and results in the relation

$$\frac{1}{\omega}(\omega T)^2(\omega R)^3 > 80. \tag{6.47}$$

Figure 6.4 is a two dimensional plot showing the regions of operation of a double reflection interferometer. The dimensionless trap frequency is $\omega = 3.5 \times 10^{-5}$ as in Fig. 6.3. The white region corresponds to large contrast. In the grey region (lower right corner) $A > 1/2$ and the contrast is small due to incomplete overlap at the recombination time. The region filled with vertical stripes corresponds to $B > 1/2$ and the contrast is small due to the phase difference across the recombined BEC. The region filled with horizontal stripes corresponds to $C > 1/2$ and the cubic phase causes the loss of contrast.

For $\omega R < 0.04$, the contrast is lost because the two harmonics $\psi_\pm$ do not overlap at the recombination time. In the region $0.04 < \omega R$ the contrast is lost because the trap causes a phase difference across the recombined harmonic. Along the curve $\omega R = \sqrt{7/96}(\omega T)^2$ the phase difference across the recombined harmonic vanishes and $B = 0$. However, when $\omega T > 0.8$, the cubic phase causes the loss of contrast and $C > 1/2$.

When the contrast is lost because of the incomplete overlap of the clouds at the nominal recombination time (term A, grey region in Fig 6.4), the contrast can be increased by recombining when the two clouds overlap. Using Eqs. (6.8) and (6.42), it can be shown that the two harmonics completely overlap at the time $\tau = T + \Delta T$, where

$$\frac{\Delta T}{R} = \frac{1}{16}\frac{(\omega T)^3}{\omega R}. \tag{6.48}$$

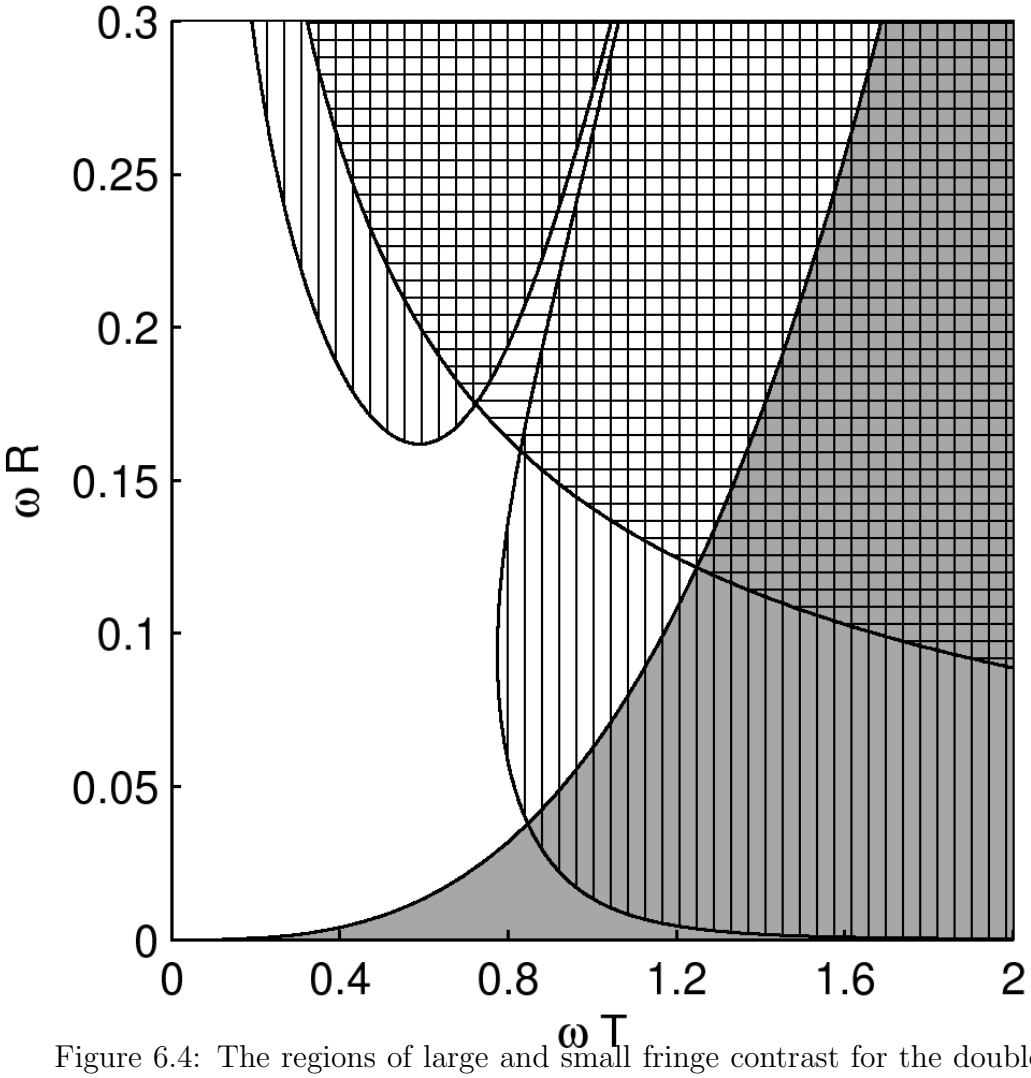

Figure 6.4: The regions of large and small fringe contrast for the double reflection interferometer. The white region corresponds to large contrast. In the grey region $A > 1/2$. The region filled with vertical stripes is where $B > 1/2$. The region filled with horizontal stripes is where $C > 1/2$.

At this shifted time, the contrast still may be lost due to the term B if

$$\left|\frac{1}{32}(\omega T)^4 - \frac{1}{28}(\omega R)^2(\omega T)^2\right| \frac{\omega R}{\omega} > 1$$

and due to C if Eq. (6.47) is fulfilled. This method for increasing the contrast is only useful when $\omega R < (\omega^3/2)^{1/7}$.

Figure 6.5 is a two-dimensional plot showing the regions of operation when the recombination pulse is applied at the time when the two clouds overlap. The dimensionless trap frequency is 3.5×10^{-5}. The white region corresponds to large values of the fringe contrast. The region filled with vertical stripes corresponds to $B > 1/2$ and the region filled with horizontal stripes to $C > 1/2$. Recombination at a shifted time improves the fringe contrast for $\omega R < 0.01$.

When the contrast is lost because of the term B (vertical stripes in Fig. 6.4), the contrast also can be increased by shifting the recombination time. This is because the quantity that determines the contrast in Eq. (6.18) is the sum of the three terms given by Eqs. (6.43), (6.44), and (6.45). A small change in the recombination time results in a change in Eq. (6.44), but does not change either Eq. (6.43) or Eq. (6.45). Using Eqs. (6.8) one can show that recombining at the time $\tau = T + \Delta T$, where

$$\frac{\Delta T}{R} = \frac{1}{192}\frac{(\omega T)^5}{\omega R} - \frac{1}{14}(\omega T)(\omega R), \tag{6.49}$$

results in $B = 0$ at the shifted recombination time. With the help of Eqs. (6.8), (6.46) and (6.49), the inequality $A > 1/2$ at the shifted recombination time translates into the relation

$$\frac{\Delta\kappa}{gR} = \frac{1}{16}\frac{(\omega T)^3}{\omega R_0} > 1, \tag{6.50}$$

The region where $C > 1/2$ is still given by Eq. (6.47). Figure 6.6 is a two-dimensional

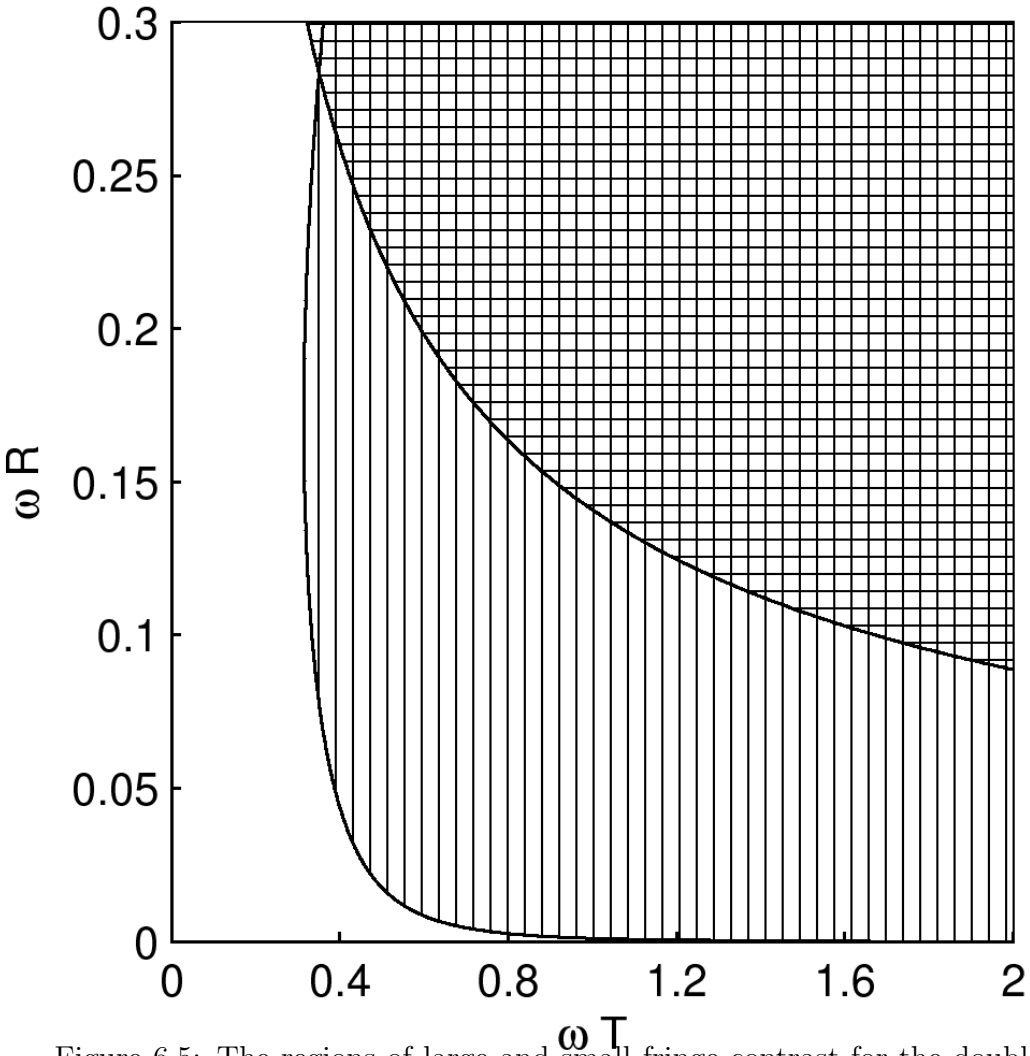

Figure 6.5: The regions of large and small fringe contrast for the double reflection interferometer. The recombination takes place at the time, when the harmonics fully overlap and $A = 0$. The white region corresponds to large contrast. The region filled with vertical stripes is where $B > 1/2$ and the region filled with horizontal stripes is where $C > 1/2$.

plot showing the different regions of operation when the recombination takes place at the shifted time given by Eq. (6.49). The dimensionless trap frequency is taken to be $\omega = 3.5 \times 10^{-5}$. The white region corresponds to large values of the fringe contrast. In the grey region the loss of contrast is caused by the term A and in the region filled with horizontal stripes by the term C. When $\omega R < 0.13$, the incomplete overlap causes the loss of fringe contrast and when $\omega R > 0.13$ the cubic phase causes the loss of contrast.

The lower limit on the values of ωR for which the fringe contrast is large with the help of Eq. (6.50) can be written as

$$\omega R \approx \frac{1}{16}(\omega T)^3. \tag{6.51}$$

and the upper limit on ωR using Eq. (6.47) can be expressed as

$$\omega R = \frac{(30\omega)^{1/3}}{(\omega T)^{2/3}}. \tag{6.52}$$

The longest cycle time before the loss of the fringe contrast is given by the relation

$$\omega T_{max} \approx 3\omega^{1/11}, \tag{6.53}$$

and occurs when the size of the BEC is

$$\omega R_{opt} \approx \frac{27}{16}\omega^{3/11}. \tag{6.54}$$

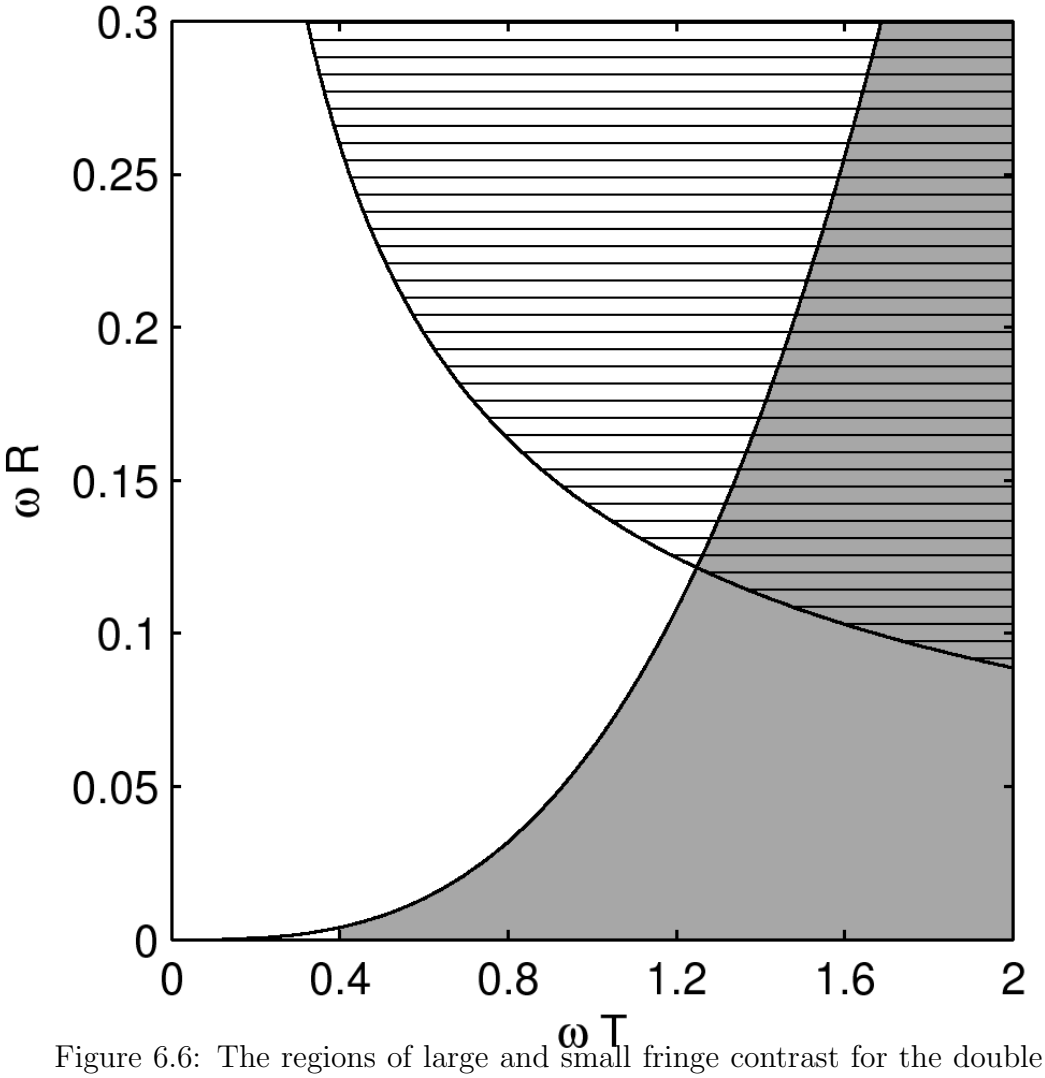

Figure 6.6: The regions of large and small fringe contrast for the double reflection interferometer, when the recombination takes place at the optimal time, when $B = 0$. The white region corresponds to large values of the contrast. In the grey region $A > 1/2$ and in the region filled with horizontal stripes $C > 1/2$.

6.5 Comparison with experiment

There have been several experimental realizations of waveguide interferometers that use optical pulses to control the dynamics of the BEC [33, 35, 34, 69, 70].

The JILA group [33] built a single reflection interferometer and used a trap with frequencies $(\omega_x, \omega_y, \omega_z) = 2\pi \times (100, 100, 5)$ Hz and a ^{87}Rb BEC with about 10^4 atoms. These parameters correspond to the nonlinearity parameter $p = 5.7$, the dimensionless BEC radius $R = 675$, the dimensionless trap frequency of $\omega = 1.7 \times 10^{-4}$ and $\omega R = 0.11$. In Ref. [33] the contrast at about 10 ms was found to be $V = 0.2$. This agrees with our model if, instead of using Eqs. (6.24) and Eq. (6.14), we use Eq. (6.24) and numerically integrate Eq. (6.12).

In the experiment at the University of Virginia [69] the trap has frequencies $(\omega_x, \omega_y, \omega_z) = 2\pi \times (3.3, 6, 1.2)$ Hz, and the BEC had about 3×10^4 ^{87}Rb atoms. These parameters correspond to the dimensionless nonlinearity parameter $p \approx 0.75$, the dimensionless BEC radius of $R = 940$, the dimensionless trap frequency of $\omega = 3.65 \times 10^{-5}$ and $\omega R = 0.035$.

The University of Virginia group experimentally investigated the operation of both a single and double reflection interferometer. When analyzing the single reflection interferometer, they found 50% contrast for the cycle time of about 12 ms. This time corresponds to $\omega T = 0.9$ (cf. Eq.(6.22)). The loss of contrast at this time agrees with Fig. 6.3 and the results of Sec. 6.3.

The double reflection interferometer had 50% contrast for a cycle time of 80 ms, translating to $\omega T = 0.6$ in our variables. The loss of contrast at this time agrees with Fig. 6.4 and the results of Sec. 6.4. The experiment used a BEC radius R such that the contrast was lost due to both the incomplete overlap (term A) and the phase across the cloud (term B) at about the same cycle time ωT. This may

explains why the University of Virginia experiment had no phase distortion across the recombined BEC. An increase of decrease in the radius R would have caused a decrease in the coherence time of the interferometer. However, our model predicts that by both increasing the radius and shifting the recombination time it would be possible to increase the coherence time.

6.6 Conclusions

In this chapter, we analyzed the operation of both single and double reflection interferometers. We introduced a simple analytic model to determine the regions in parameter space where the fringe contrast is large and small. For the case of a double reflection interferometer, we showed that the coherence time can be increased by changing the recombination time. Finally, we compared our results to recent experimental realizations of these interferometers.

Our analysis focused on the case where the BEC was in the ground state of the trap at the beginning of the interferometric cycle. Analysis of the single reflection interferometer when this restriction is relaxed can be found in [52]. In the case of a double reflection interferometer, the two largest terms (of order $(\omega T)^4$) in Eqs. (6.43) and (6.44) are only equal when the BEC is initially in the ground state. As a result, the region of high contrast discussed in Sec. 6.4 becomes smaller when the BEC is not initially in the ground state.

The analysis of this chapter did not include effects beyond the mean field approximation such as phase diffusion and finite temperature phase fluctuations.

The phase fluctuations of a BEC in a trap have been extensively studied in Ref. [71, 72, 73, 74]. It has been shown that the phase diffusion time has the functional form $T_D \sim (\bar{a}_{HO}/a_s)^{2/5} N^{1/10}/\bar{\omega}$ [72], where $\bar{\omega} = (\omega_x \omega_y \omega_z)^{1/3}$ is the geometric

average of the trap frequencies and $\bar{a}_{HO} = \sqrt{\hbar/M\bar{\omega}}$ is the average oscillator length. For the case of the University of Virginia experiment [69], the phase diffusion time is $T_D \sim 3$ sec, which is much longer than the upper limit calculated in Sec. 6.5.

When the aspect ratio of the trap $\omega_\parallel/\omega_\perp$ becomes sufficiently large, the BEC becomes one-dimensional and phase fluctuations can cause decoherence [75, 76, 77, 78]. The phase fluctuations along the BEC depend on the aspect ratio and temperature of the BEC and become important when the temperature of the BEC is larger than $T = 15(\hbar\omega_\parallel)^2 N/32\mu$ [75], where μ is the chemical potential of the BEC. For the recent experiments [33, 34], the phase fluctuations across the BEC are sufficiently small that they can be neglected.

Chapter 7

The BEC transistor

7.1 Introduction

One of the most important components of a microelectronic circuit is a transistor. In this paper we present a BEC-based device which will be subsequently called a BEC transistor or an atom transistor. It enables one to control a large number of atoms with a smaller number of atoms and demonstrates switching and both differential and absolute gain thus showing behavior similar to that of an electronic transistor. The device is not optimized for performance but is arguably the simplest possible geometry showing behavior reminiscent of a transistor. This makes its experimental realization relatively easy with existing atom chip techniques.

The BEC transistor uses a Bose Einstein condensate in a triple well potential, as shown schematically in Fig 7.1. In fact, Fig. 7.1 refers to two subtly different possible experimental realization of the device. In the trapped configuration, the BEC is confined in all three dimensions in the potential wells. The wells are allowed to interact for time interval T. This is done either spatially bringing them together and separating apart after time T of changing the shapes of the potential wells so that the interaction is suppressed after time T. In the waveguide configuration, the potential wells of Fig. 7.1 represent three guides that converge, run parallel to each other for distance L and then diverge. The interaction time $T = L/v$ in this geometry is determined by the speed of flow v of the BEC in the guides. In the following for definiteness we will use the terminology appropriate for the trapped configuration.

The BEC transistor is similar to an electronic field effect transistor. The left well behaves like the source, the middle as the gate, and the right well is equivalent to the drain. If there are no atoms in the middle well, practically no atoms tunnel from the left into the right well, as shown in Fig. 7.1a. A small number of atoms placed

into the middle well switches the device resulting into the strong flux of atoms from the left well (the source) through the middle and into the right well as shown in Fig. 7.1b. Increasing number of atoms in the middle well increases the number of atoms that tunnel into the right well. Parameters of the triple well structure are chosen so that the number of atoms having tunneled into the right well at the end of the interaction period is much larger that the number of atoms in the middle well. In the subsequent sections we will show that the BEC transistor exhibits both absolute and differential gain.

The physics of operation of the BEC transistor is based on atom-atom interactions and appropriate design of the potentials. The chemical potential of the left well is chosen to be nearly equal to the ground state energy level of the empty right well (in Fig. 7.1 we make them equal). The ground state energy of the empty middle well is chosen to be considerably lower than that in both the left and the right wells. Placing atoms in a well raises the value of chemical potential due to atom-atom interactions. Parameters of the potential wells are chosen so that the chemical potential in the middle well is considerably more sensitive to the change in the number of atoms in the well than is the case for the left and right wells.

When the middle and right wells are initially unpopulated, tunneling of atoms from the left to the middle well is blocked because of the energy mismatch as shown in Fig. 7.1c. If some amount of atoms is placed into the middle well, the atom-atom interactions will increase the energy of the atoms in the middle well. When the chemical potential in the middle well becomes nearly equal to that in the left and right wells, the device switches and atoms become able to tunnel from the left through the middle into the right well as shown in Fig. 7.1d.

Using atom-atom interactions to block tunneling in a double-well structure is often referred to as self trapping. This effect was first described in Ref. [61]. If a

condensate is placed in one of the two weakly-coupled spatially separated potential wells with matched energy levels, it can oscillate between the wells by linear quantum tunneling. However, due to atom-atom interactions, the tunneling is blocked when the number of atoms in the condensate exceeds some critical value. This suppression is due to the fact that interactions increase chemical potential of the atoms in the occupied wells and introduce nonlinear energy mismatch. Self trapping has been analyzed for a large number of systems including asymmetric double well potentials [79] and symmetric three well systems [80]. It has also been observed experimentally for atoms in a one dimensional optical lattice [81].

The quantum state of two trapped Bose-Einstein condensates in a double well potential has been analyzed in Ref. [82]. It has been shown that when the two wells are separated and the interaction between the atoms is repulsive, the lowest energy state is fragmented, which means that the coherence between the atoms in each well is lost. The dependence of this fragmentation on the splitting rate and physical parameters of the potential has been analyzed in Refs. [83] and [84]. The visibility of interference fringes after splitting of a condensate with both attractive and repulsive interactions was analyzed in Ref. [85], who showed a decrease in quantum noise in the case of attractive interactions. The quantum dynamics of atoms in a symmetric double well potential, where the atoms are in an initially fragmented state was also analyzed in [86].

Bose Einstein condensates in triple well structures have been analyzed and the stationary solutions in the mean field approximation were found in Ref. [87]. Three well systems show chaotic solutions [88] and the dynamics of atoms in a three well potential is sensitive to the initial conditions of the system [80]. This means that one can control the dynamics of the system not only by varying the physical parameters of the potential, but also by changing the initial conditions.

The rest of the chapter is organized as follows. Section 7.2 contains derivation of the general equations of motion for a BEC in an n-well potential with arbitrary shapes of the wells and discussion of the limits of validity of the model. In Sec. 7.3 we specialize our discussion to the case of a three well structure. Sec. 7.3.1 is devoted to the analysis of the equations of motion in the mean field limit and in Sec. 7.3.2 we will compare the results of the mean field to a second quantization calculation. Section 7.4 contains estimates of the physical parameters for the device and discusses the possibility of its experimental realization.

7.2 Equations of motion

The Hamiltonian for a system of interacting bosons in an external potential $V(x)$ is of the form

$$H = \int dx \hat{\Psi}^\dagger \left[-\frac{\hbar^2}{2m}\nabla^2 + V(x) \right] \hat{\Psi} + \frac{U_0}{2} \int dx \hat{\Psi}^\dagger \hat{\Psi}^\dagger \hat{\Psi} \hat{\Psi}. \tag{7.1}$$

Here $\hat{\Psi}$ is the field operator and $U_0 = 4\pi a_s \hbar^2/m$, where m is the atomic mass and a_s is the s-wave scattering length. For notational simplicity we are considering one-dimensional case. Extension to two or three dimensions is straightforward.

In the standard basis of eigenfunctions ψ_i of the linear part of the Hamiltonian

$$\left[-\frac{\hbar^2}{2m}\nabla^2 + V(x) \right] \psi_i = \hbar \Omega_i \psi_i, \tag{7.2}$$

the field operator is represented as

$$\hat{\Psi} = \sum_i \psi_i a_i, \tag{7.3}$$

where a_i is the destruction operator for the mode ψ_i. These operators satisfy the

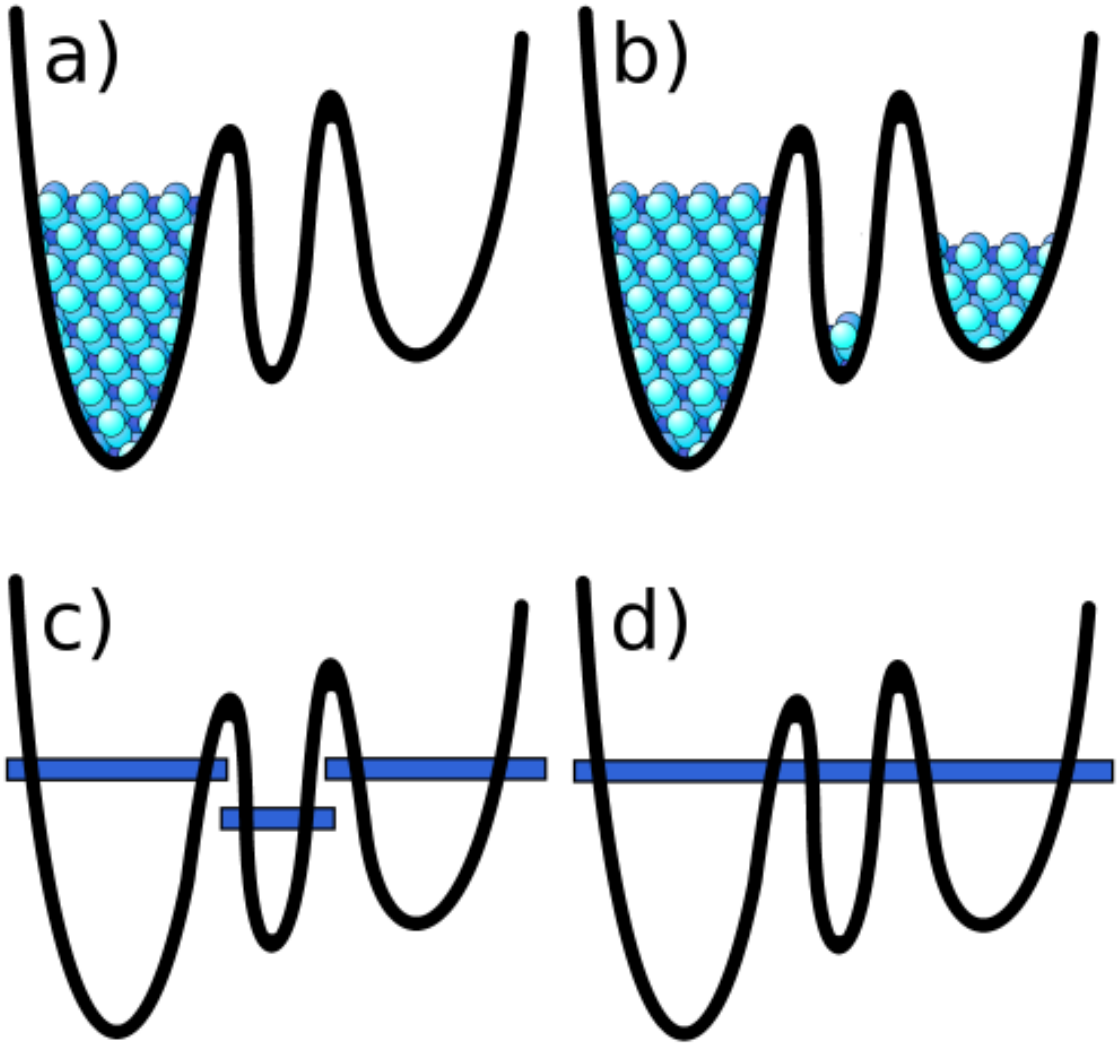

Figure 7.1: (Color online) The geometry of a BEC transistor. When the number of atoms in the middle well is small, tunneling from the left into the right well is negligible (a). This is due to the fact that the chemical potential of the middle well does not match that of the two other wells (c). Placing atoms in the middle well increases the chemical potential due to interatomic interactions (d) and enables tunneling then atoms tunnel from the left into the right well. This happpens because atom-atom interactions increase the energy of the middle guide (b).

canonical commutation relations

$$[a_i, a_j^\dagger] = \delta_{ij},$$
$$[a_i, a_j] = 0. \tag{7.4}$$

The potential $V(x)$ consists of n weakly coupled potential wells. The eigenmodes ψ_i are "nonlocal" and extend over several potential wells. As discussed above, we are interested in calculating the number of atoms in each well as a function of time. A more convenient basis in this case corresponds to a set of modes ϕ_i localized in each potential well with the corresponding destruction operators b_i so that

$$\hat{\Psi} = \sum_i \phi_i b_i. \tag{7.5}$$

The operators b are linear superpositions of the operators a,

$$b_i = \sum_j u_{ji} a_j, \tag{7.6}$$

where u is the transformation matrix determined by the condition of localization of the modes ϕ_i.

Requiring that the destruction operators b_i satisfy the canonical commutation relations identical to those of Eq. (7.4)

$$[b_i, b_j^\dagger] = \delta_{ij},$$
$$[b_i, b_j] = 0, \tag{7.7}$$

implies the unitarity of the transformation matrix u: $\sum_m u_{mi} u_{mj}^* = \delta_{ij}$. For bound states all modes ψ_i can be chosen real and the transformation matrix u can be chosen

real and orthogonal.

The transformation from the "nonlocal" basis ψ_i to the "local" basis ϕ_i is given by the relations

$$\phi_i = \sum_j u^*_{ji} \psi_j. \tag{7.8}$$

The operators b_i are associated with the local modes of the n-well structure. For the purposes of the subsequent analysis we will need to know only the lowest local mode in each potential well. It means that there are n local modes ϕ_i and the coefficients u_{ij} should be chosen so that the function ϕ_i be localized in the i-th potential well.

To quantify the degree of localization, we set points $x_0, x_1, ..., x_n$ somewhere between the wells where amplitudes of the modes ψ_k are exponentially small. This procedure is shown schematically in Fig. 7.2. The degree of localization of the mode ϕ_k in the k-th well is characterized by the localization parameter

$$f_k = \int_{x_{k-1}}^{x_k} dx |\phi_k|^2. \tag{7.9}$$

The localization parameter f_k can be rewritten in terms of the transformation matrix u as

$$f_k = \sum_{m,l} u_{mk} u^*_{lk} J_k(l,m), \tag{7.10}$$

where the matrix $J_k(l,m)$ is given by the expression

$$J_k(l,m) = \int_{x_{k-1}}^{x_k} dx \psi^*_m \psi_l. \tag{7.11}$$

To localize the modes ϕ_k, we maximize the function

$$f = \sum_k f_k = \sum_{kml} u_{mk} u^*_{lk} J_k(l,m) \tag{7.12}$$

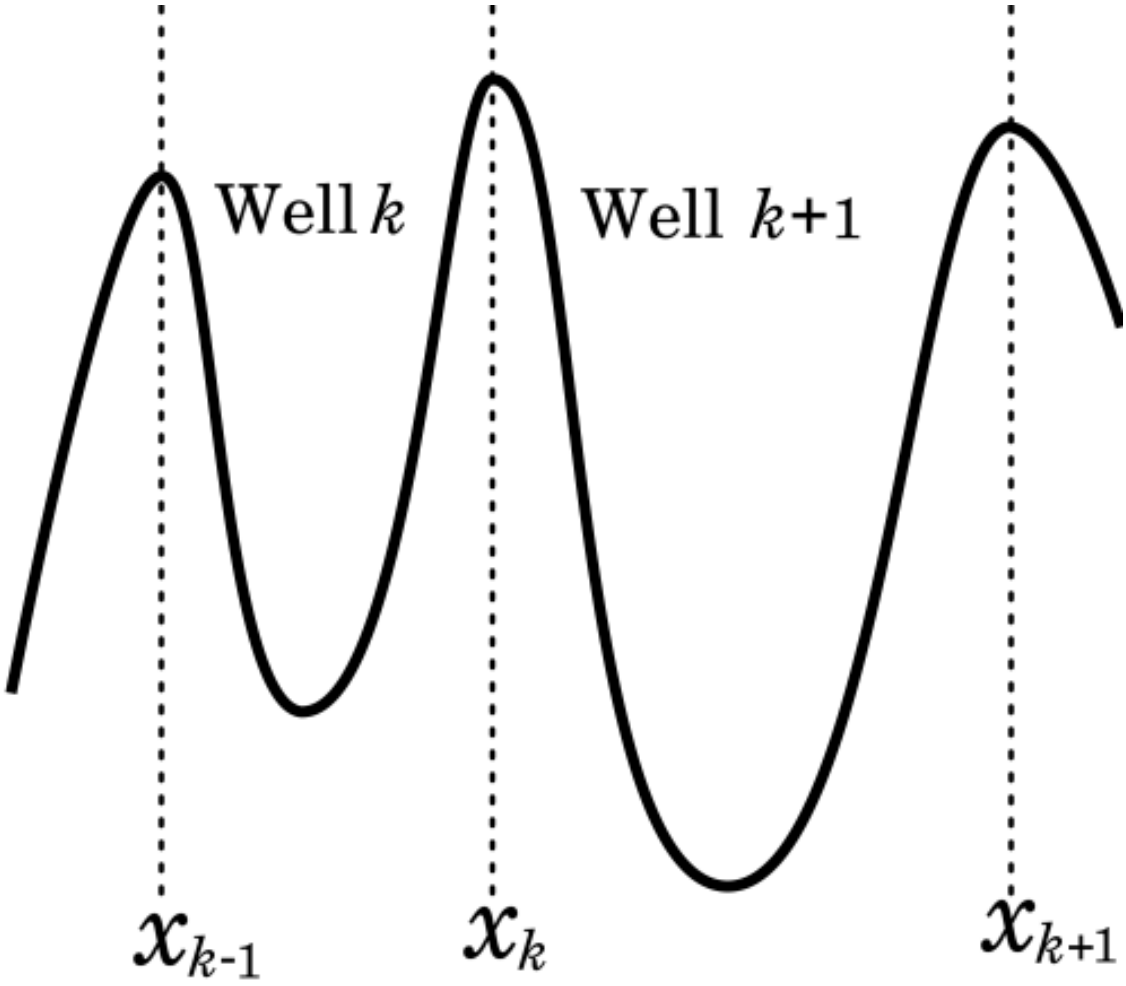

Figure 7.2: A schematic of a multi-well non-symmetric potential structure with two adjacent wells shown. The points x_{k-1}, x_k and x_{k+1} are chosen between the wells where the eigenmodes ψ_k are exponentially small.

subject to constraints

$$\sum_k u_{mk} u_{lk}^* = \delta_{ml}. \tag{7.13}$$

The maximization results in the set of n^2 equations

$$\sum_m \left[J_j(i,m) - \lambda_{im} \right] u_{mj} = 0, \tag{7.14}$$

where $1 \leq i, j \leq n$ and where $\lambda_{im} = \lambda_{mi}^*$ are Lagrangian multipliers.

The set of equations (7.14) can be written in a more transparent form as a set of n matrix equations ($j = 1, 2, \ldots n$)

$$\left(\hat{J}_j - \hat{\lambda} \right) |u_j\rangle = 0, \tag{7.15}$$

where $\hat{J}_j$ and $\hat{\lambda}$ are Hermitian matrices with the elements $J_j(i,m)$ and λ_{im}, respectively, and where $|u_j\rangle$ is the column vector of u with the elements u_{mj} ($m = 1, 2, \ldots n$). The equation of constraints, Eq. (7.13), becomes

$$\langle u_i | u_j \rangle = \delta_{ij}. \tag{7.16}$$

In the limit of negligibly small coupling between the wells, the column vectors $|u_k\rangle$ of the transformation matrix u are exact eigenvectors of the operators $\hat{J}_j$ because the latter in this limit reduce to $\hat{J}_j = |u_j\rangle\langle u_j|$. The matrix of Lagrange multipliers in this limit becomes the identity matrix. This observation suggests that for nonzero coupling between the wells the vectors $|u_k\rangle$ can be found perturbatively starting from the eigenvectors $|w_k\rangle$ of $\hat{J}_k$ with eigenvalues close to one:

$$\hat{J}_k |w_k\rangle = \mu_k |w_k\rangle = (1 - \epsilon a_k) |w_k\rangle, \tag{7.17}$$

where $\epsilon \ll 1$ characterizes relative coupling strength between the wells. The eigenvectors $|w_k\rangle$ form a nonorthogonal basis set with $\langle w_i|w_j\rangle = O(\epsilon)$ for $i \neq j$.

Solution of Eq. (7.17) in the $|u_k\rangle$ basis to the first order in ϵ yields

$$|w_k\rangle = |u_k\rangle + \sum_{j\neq k} |u_j\rangle\langle u_j|\hat{J}_k|u_k\rangle, \tag{7.18}$$

where we have used the fact that $\hat{J}_k - |u_k\rangle\langle u_k| = O(\epsilon)$. Inversion of Eq. (7.18) yields

$$|u_i\rangle = |w_i\rangle - \sum_{j\neq i} |w_j\rangle\langle u_j|\hat{J}_i|u_i\rangle, \tag{7.19}$$

Using the orthogonality conditions for $|u_i\rangle$ up to the first order in ϵ and the condition $\langle u_i|\hat{J}_j|u_j\rangle = \langle u_i|\hat{J}_i|u_j\rangle$ that follows from Eq. (7.15), results in the relation

$$\langle u_i|\hat{J}_j|u_j\rangle = \frac{1}{2}\langle w_i|w_j\rangle \tag{7.20}$$

yielding the final expression for the vectors $|u_i\rangle$ in terms of $|w_i\rangle$:

$$|u_i\rangle = |w_i\rangle - \frac{1}{2}\sum_{j\neq i} |w_j\rangle\langle w_j|w_i\rangle. \tag{7.21}$$

To calculate the local modes, one thus finds eigenvectors $|w_i\rangle$ of $\hat{J}_i$ with eigenvalues close to one for $i = 1, 2, \cdots n$. The columns of the transformation matrix are then given by Eq. (7.21). The local modes are found using Eq. (7.8). An example of such calculation is shown in Fig. 7.3.

Overall signs of the local modes ϕ_i in Eq. (7.8) are arbitrary being determined by sign choices for the global modes ψ_i. These signs can be changed if needed because if ϕ_i is a local eigenmode, so is $-\phi_i$. Changing the sign of ϕ_i amounts to changing the sign of the i-th row of the transformation matrix u which leaves it

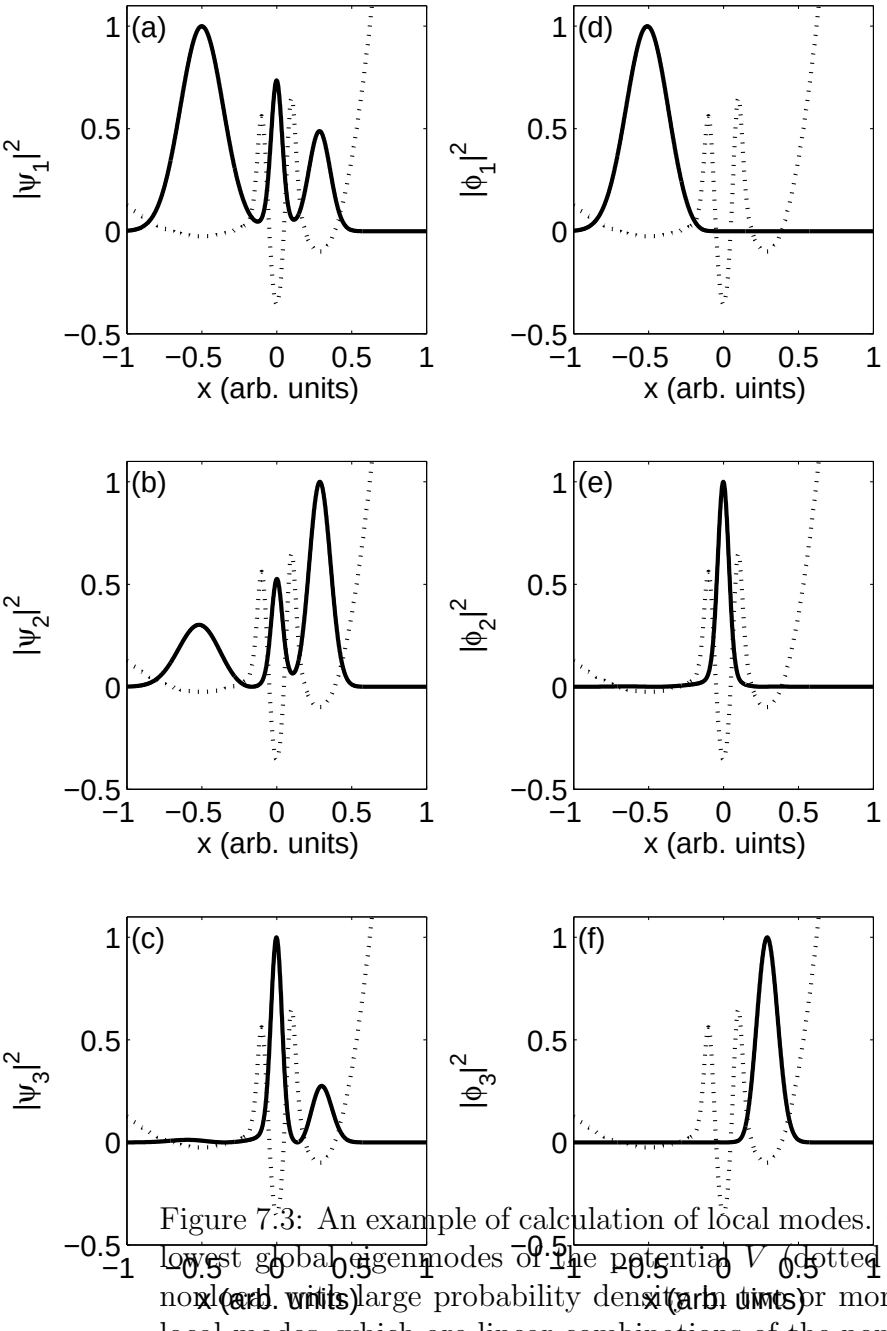

Figure 7.3: An example of calculation of local modes. Graphs (a)-(c) show the three lowest global eigenmodes of the potential V (dotted line). These eigenmodes are nonlocal, with large probability density in two or more wells. Graphs (d)-(f) show local modes, which are linear combinations of the nonlocal eigenmodes.

unitary. To be able to unambiguously specify the value of the relative phase shift between condensates in different potential wells, the overall signs of the local modes ϕ_i will be fixed by requiring that each eigenmode ϕ_i be positive in the region of its localization between x_i and x_{i+1}.

In terms of the destruction operators b_i of the local modes the Hamiltonian Eq. (7.1) can be written as

$$H = \sum_{ijk} \hbar \Omega_k u_{ki} u_{kj}^* b_i^\dagger b_j + \frac{U_0}{2} \sum_i \kappa_i \left(b_i^\dagger\right)^2 b_i^2, \tag{7.22}$$

where Ω_i is the eigenfrequency of the i-th mode ψ_i given by Eq. (7.2), u_{ij} is the transformation matrix and κ_i is the overlap integral

$$\kappa_i = \int dx |\phi_i|^4. \tag{7.23}$$

The equations of motion for the operators b_i in the Heisenberg picture are given by

$$i\hbar \frac{d}{dt} b_i = \sum_{jk} \hbar \Omega_k u_{ki} u_{kj}^* b_j + U_0 \kappa_i b_i^\dagger b_i^2. \tag{7.24}$$

The diagonal terms

$$\Lambda_i = \sum_k \Omega_k |u_{ki}|^2 \tag{7.25}$$

in Eq. (7.22) have the meaning of eigenfrequencies of the local eigenmodes in the absence of coupling between the wells and the nondiagonal terms

$$\Delta_{ij} = \sum_k \Omega_k u_{ki} u_{kj}^* \tag{7.26}$$

are coupling frequencies between the i-th and j-th wells. Since for bound states u can be chosen real, the matrix of the coupling frequencies is real and symmetric: $\Delta_{ij} =$

Δ_{ji}. The coupling strength is exponentially dependent on the distance between the wells and usually only the nearest-neighbor coupling should be taken into account.

7.3 Three-well structure

In the following we shall specialize our analysis to the case of a potential consisting of three potential wells. These will be referred to as the left, middle and right well, respectively. The left well serves as a source of atoms. The number of atoms N_l in this well is kept nearly constant and is considerably larger than the number of atoms initially placed and subsequently tunneling into the middle or the right wells. The dynamics in the left well is therefore unaffected by that in the other two wells. This dynamics is factored out and the destruction operator for the left well b_l is replaced by a c-number: $b_l =\longrightarrow \sqrt{N_l}$. This approximation is valid when as long as the depletion of the left well is small $N_l \gg \langle b_m^\dagger b_m \rangle + \langle b_r^\dagger b_r \rangle$.

The Hamiltonian Eq. (7.22) reduces to

$$\begin{aligned} H &= \hbar(\Lambda_m - \mu) b_m^\dagger b_m + \hbar(\Lambda_r - \mu) b_r^\dagger b_r \\ &+ \hbar(\Delta_{lm}\sqrt{N_l} b_m + \Delta_{mr} b_m^\dagger b_r + h.c.) \\ &+ \frac{U_0}{2}\kappa_m \left(b_m^\dagger\right)^2 b_m^2 + \frac{U_0}{2}\kappa_r \left(b_r^\dagger\right)^2 b_r^2 \end{aligned} \tag{7.27}$$

where Λ_i, Δ_i and κ_i are given by Eqs. (7.25), (7.26) and (7.23), respectively, $h.c.$ means Hermitian conjugate and $\mu = \hbar\Lambda_l + \kappa_l U_0 N_l$.

As discussed at the end of Sec. 7.2, the overall sign of the local modes ϕ_i has been fixed by requiring that they be positive in the region of their localization. With this choice, the coupling frequencies Δ_{ij} between different wells (see Eq. (7.26)) are negative. This is easily ascertained using the simplest example of a symmetric two-

well structure where the two local modes are proportional to a sum and a difference of the two global modes. Normalizing the Hamiltonian Eq. (7.27) to the positive energy $-\hbar\Delta_{mr} = \hbar|\Delta_{mr}|$ brings it to its final dimensionless form

$$\begin{aligned} \frac{H}{\hbar|\Delta_{mr}|} &= \omega_m b_m^\dagger b_m + \omega_r b_r^\dagger b_r - (D b_m + b_m^\dagger b_r + h.c.) \\ &+ \frac{Z_m}{2}\left(b_m^\dagger\right)^2 b_m^2 + \frac{Z_r}{2}\left(b_r^\dagger\right)^2 b_r^2, \end{aligned} \tag{7.28}$$

where $Z_i = -U_0\kappa_i/\hbar\Delta_{mr}$, $\omega_i = (\mu - \Lambda_i)/\Delta_{mr}$ and $D = \Delta_{lm}\sqrt{N_l}/\Delta_{mr}$.

The Heisenberg equations of motion for the destruction operators b_l and b_r (7.24) in the dimensionless variables take the form

$$\begin{aligned} i\frac{d}{d\tau}b_m &= (\omega_m + Z_m b_m^\dagger b_m)b_m - D - b_r \\ i\frac{d}{d\tau}b_r &= (\omega_r + Z_r b_r^\dagger b_r)b_r - b_m, \end{aligned} \tag{7.29}$$

where the dimensionless time τ is given by the relation $\tau = |\Delta_{mr}|t$.

7.3.1 Mean-field

In this section we shall present results of analysis of Eq. (7.29) in the mean-field limit corresponding to relatively large atomic populations in all wells, when the operators b_m and b_r can be treated as complex numbers.

Figure 7.4 demonstrates control of atomic population in the right well by population in the middle well with the absolute gain that is considerably larger than one. Parameters for Fig. 7.4 are $\omega_m = -1.3$, $\omega_r = 0.5$, $Z_m D^2 = 1$ and $Z_r D^2 = 0$. The right well is initially empty, $b_r(0) = 0$. Parameters of the wells are chosen so that if no atoms are initially placed in the middle well ($b_m(0) = 0$), the tunneling from the

source (the left well) to the middle well is strongly suppressed and the population in the right well remains at a low level. This situation is illustrated by a dotted line in Fig. 7.4.

Placing some number of atoms in the middle well results in a much larger tunneling rate from the left to the right well through the middle well as shown by a solid line corresponding to the initial condition $b_m(0) = D$. The increase in the tunneling rate can be observed for a range of values of the relative phase of the condensates in the left and middle wells. The dashed curve obtained for the initial condition $b_m(0) = D\exp(i\pi/2)$, i.e., corresponding to the $\pi/2$ relative phase shift between the condensates in the left and middle wells, exhibits qualitatively similar behavior. Note that the output number of atoms in the right well ($\tau = 20$) is about $50 - 60$ times larger than the input number of atoms in the middle well. In other words, the output number of atoms in the right is controlled by that in the middle well with the absolute gain $G = N_{r,out}/N_{l,in} \approx 50 - 60$.

Populations in the middle and right wells as functions of the interaction time are shown if Fig. 7.5 for $b_m(0) = D$. All other parameters are the same as in previous graphs. The solid curve is the population of the right well and the dashed curve is the population of the middle well. Figure 7.5 demonstrates that the population of the middle well stays about an order of magnitude below that for the right well. The middle well serves a gate controlling the rate of atomic flow from the source to the right well. The atoms tunneling from the source to the right well pass through the middle well without being accumulated there.

The output number of atoms in the right well as a function of the input number of atoms in the middle well is shown in Fig. 7.6. Parameters for this figure are the same as for Fig. 7.4, i.e., $\omega_m = -1.3$, $\omega_r = 0.5$, $Z_m D^2 = 1$ and $Z_r D^2 = 0$. The solid curve corresponds to the zero initial phase shift between the condensates in the left and

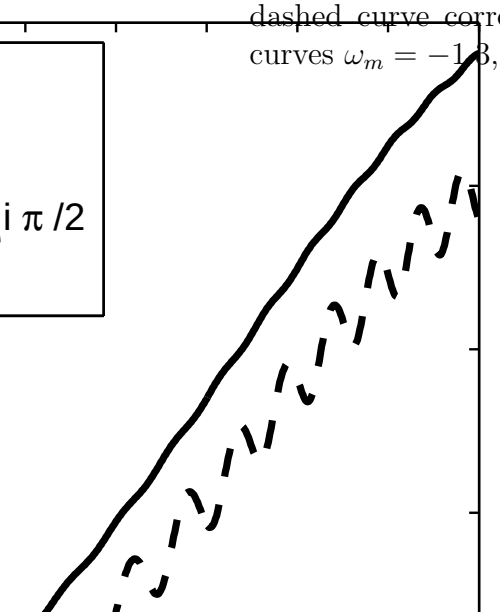

Figure 7.4: The number of atoms in the right well as a function of interaction time for different initial number of atoms in the middle well. The dotted curve corresponds to initially empty middle well, $b_m(0) = 0$, and the solid curve to $b_m(0) = D$. The dashed curve corresponds to the initial condition $b_m(0) = D\exp(i\pi/2)$. For all curves $\omega_m = -1.3$, $\omega_r = 0.5$, $Z_m D^2 = 1$ and $Z_r D^2 = 0$.

Figure 7.5: The number of atoms in the middle (dashed) and right (solid curve) well as a function of interaction time for $\omega_m = -1.3$, $\omega_r = 0.5$, $Z_m D^2 = 1$, $Z_r D^2 = 0$ and $b_m = D$

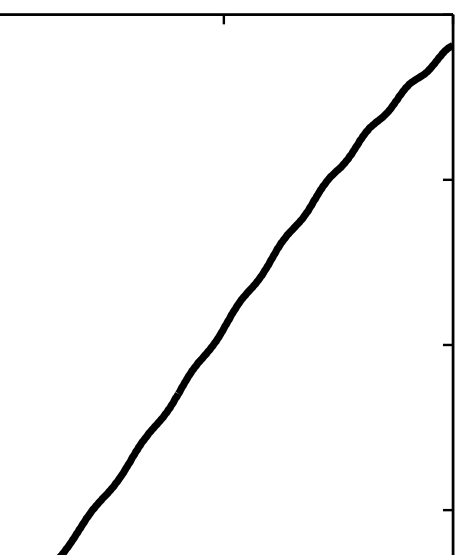

middle wells and the dotted curve to the $\pi/2$ shift. This figure demonstrates rapid switching from small to large tunneling rates in the region around $|b_{m,in}|^2 D^2 \approx 0.5$ with subsequent saturation at the level $G = N_{r,out}/N_{m,in} \approx 50-60$. In the switching region, a small change in the population of the atoms in the middle well results in a large difference in the population in the right well.

Figure 7.7 shows output population in the right well ($\tau = 20$) as a function of the modal frequency ω_m of the middle guide for different values of the input number of atoms in the middle well. This figure demonstrates switching for different values of the number of atoms initially in the middle well. The dotted line corresponds to initially empty middle well. For this curve, the maximum tunneling rate corresponds to the region around $\omega_m = -0.5$. If the frequency of the middle well is lowered beyond this value, the number of atoms that tunnel into the right well becomes small. The solid curve corresponds to the initial condition $b_m(0) = D$. This curve is qualitatively similar to that for an initially empty middle well, but the maximum has moved to a lower value of $\omega_m = -1.3$. The dashed curve corresponds to the initial condition $b_m(0) = D\exp(i\pi/2)$. This curve still has a maximum around $\omega_m = -1.3$. For this value of ω_m, the number of atoms that tunnel into the right well when the initial atoms have either zero or $\pi/2$ phase shift is about the same. For the initially empty middle well, the population in the right well remains small.

As opposed to an electronic transistor, the amplification and switching in the three-well structure is a coherent effect and depends on the relative phase between the condensates in the left and middle wells. To investigate sensitivity of the previously obtained results to the value of the relative phase angle, we kept the input number of atoms in the middle well fixed at $|A_m(0)/D|^2 = 1.2$ and changed the relative phase angle. The results are given by Fig. 7.8 showing the output number of atoms in the right well ($\tau = 20$) as a function of the phase angle. All other

Figure 7.6: The output number of atoms in the right well ($\tau = 20$) as a function of the number of atoms initially placed in the middle well.

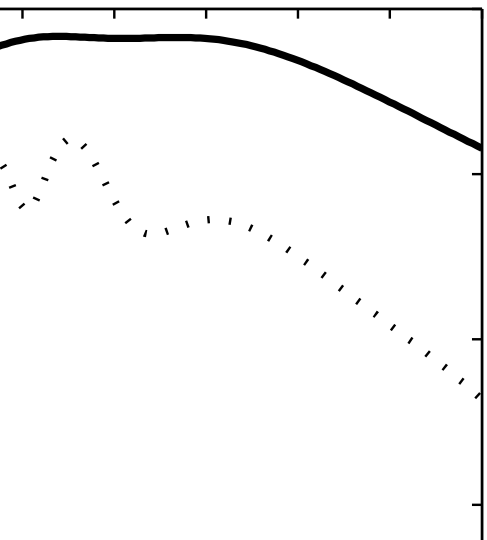

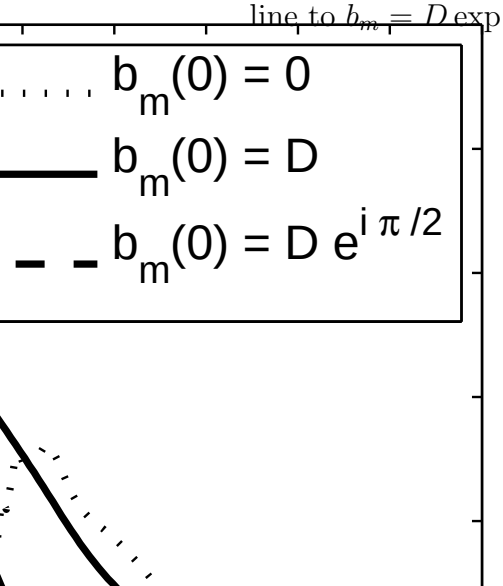

Figure 7.7: The output number of atoms in the right well ($\tau = 20$) as a function of the dimensionless frequency of the middle well ω_m. The dotted line corresponds to the initially empty middle well, $b_m(0) = 0$, the solid line to $b_m = D$, and the dashed line to $b_m = D\exp(i\pi/2)$.

parameters are the same as in previous figures. Figure 7.8 demonstrates that in the amplification regime the number of atoms that tunnel into the right well is nearly independent of the initial phase angle, as long as this angle is roughly in the range between $-\pi/2$ and $\pi/2$.

7.3.2 Second-quantization results

This section presents results of analysis of the three-well structure in the framework of the second-quantization formalism. This allows us to estimate the region of applicability of the mean-field approach of section 7.3.1, evaluate intrinsic quantum-mechanical uncertainty due to finite number of atoms and extend previous results to the limit of small number of atoms.

In the dimensionless variables, the state vector of the system $|\psi(t)\rangle$ evolves according to the equation

$$i\frac{d}{d\tau}|\psi\rangle = H|\psi\rangle, \tag{7.30}$$

where H is the second-quantized Hamiltonian given by Eq. (7.28). The state vector can be represented in terms of the joint number states $|n_m, n_r\rangle$ as

$$|\psi\rangle = \sum_{i,j} c_{i,j}|n_i, n_j\rangle, \tag{7.31}$$

with the decomposition coefficients given by $c_{m,r} = \langle n_m, n_r|\psi\rangle$. Equation (7.30) is transformed to the set of ordinary differential equations that describe the evolution of the decomposition coefficients

$$i\frac{d}{d\tau}c_{i,j} = \sum_{i,j,k,l} \langle n_i, n_j|H|n_k, n_l\rangle c_{k,l}. \tag{7.32}$$

In simulations, the set of Eqs. (7.32) has been truncated by keeping only the

Figure 7.8: The output number of atoms in the right well as a function of the relative phase of the atoms placed in the middle well.

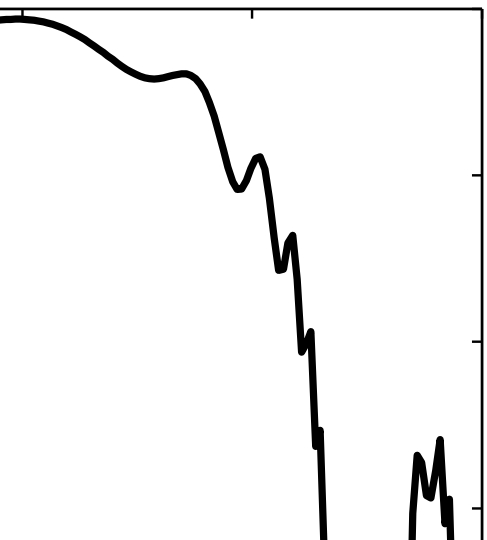

values of n_m and n_r such that $n_r + n_m \leq N_{max}$. The value of N_{max} was chosen so that N_{max} was several times larger than the sum $\langle n_r \rangle + \langle n_m \rangle$.

Initial conditions for the system of equations Eq. (7.32) corresponded to zero initial number of atoms in the right well with the atoms in the middle well being in a coherent state:

$$|\psi(0)\rangle = e^{-|\alpha|^2} \sum_{n=0}^{N_{max}} \frac{\alpha^n}{\sqrt{n!}} |n, 0\rangle. \tag{7.33}$$

Here the complex parameter α is given by $\alpha = \sqrt{\langle N_m \rangle(0)} e^{i\varphi}$, where $\langle N_m \rangle(0)$ is the average number of atoms initially placed in the middle well and φ is the phase difference between the atoms in the middle and left wells.

The transition to the mean-field limit corresponds to increasing the input number of atoms in the middle well $\langle N_m \rangle(0)$ while keeping the ratio $\omega_m / Z_m \langle N_m \rangle(0)$ constant. Equations (7.28) show that the results of action of the destruction operators on the state vector scales as D provided the parameters $Z_m D^2$ and $Z_r D^2$ are kept constant. Thus, the transition to the mean-field limit can be implemented by setting the initial number of atoms in the middle well proportional to D^2 and increasing the value of coupling D between the left and middle wells while keeping the parameters $Z_m D^2$ and $Z_r D^2$ constant.

The average number of atoms in the right well $\langle N_r \rangle$ as a function of the interaction time is shown in Fig. 7.9 for three different values of D^2. The parameters for this figure are $\omega_r = 1$, $\omega_m = -0.5$, $Z_m D^2 = 1/4$, $Z_r D^2 = 0$ and $|\alpha|^2 = \langle N_m \rangle(0) = D^2$. The phase angle of the coherent state is zero. The solid line is the mean-field limit. The dotted, dash-dotted and dashed lines correspond to $D^2 = 1$, $D^2 = 4$ and $D^2 = 8$, respectively. Figure 7.9 demonstrates good convergence of the second-quantization results to the mean field limit as D^2 is increased. The $D^2 = 1$ curve deviates from the mean-field limit for large value of τ, but all other curves lie progressively closer

Figure 7.9: The average number of atoms in the right well as a function of the interaction time for three different values of the coupling between the left and the middle wells. Atoms in the middle well are initially in a coherent state with $\langle N_m \rangle(0) = D^2$ and zero phase. The solid line is the result of the mean-field calculation, the dotted line is the result of the second-quantization calculation with $D^2 = 1$, the dashed line corresponds to $D^2 = 4$, and the dash-dotted one to $D^2 = 8$.

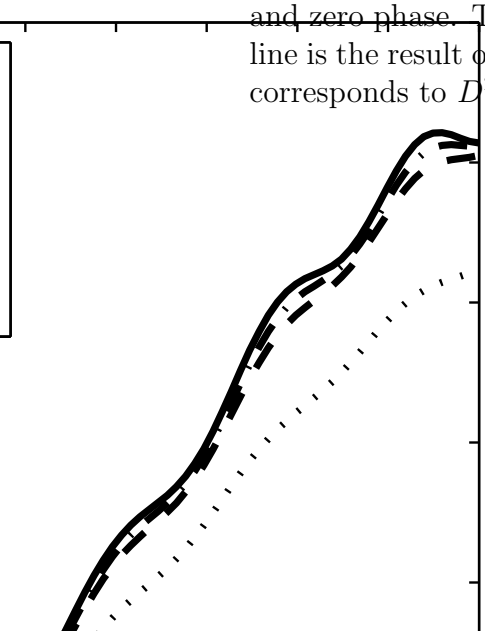

to the mean-field curve as the parameter D increases.

The output ($\tau = 10$) probability distribution $P(N_r)$ of finding N_r atoms in the right well versus N_r is shown if Fig. 7.10. The dash-dotted line corresponds to $D^2 = 1$, the dashed line to $D^2 = 4$ and the sold line to $D^2 = 8$. Since the number of output atoms scales as D^2, the horizontal axes is scaled as N_r/D^2 to keep position of the maximum and the width of the curves more of less the same for different values of D^2. As a result, the vertical axes shows not $P(N_r)$, but the product $P(N_r)D^2$ to keep the height of the curves approximately the same for different values of D^2. The total "area under the curve" (strictly speaking it is a sum, not an integral) for all curves is equal to one. The dash-dotted curve corresponding to $D^2 = 1$ shows bimodal distribution with a relatively large probability of finding atoms near zero N_r in addition to the main peak near $N_r/D^2 \approx 31$, the latter being very close to the mean-field result. The difference between the mean-field and second-quantization results, previously seen in Fig. 7.9 for $D^2 = 1$, is due to the part of the probability distribution near zero that pulls down the average. As the coupling D to the source is increased, only the single-humped part of the probability $P(N_r)$ centered at the mean-field result remains. The output relative standard deviation $\Delta N_r/\langle N_r \rangle$ is equal to 0.35, 0.08 and 0.04 for $D^2 = 1, 4$ and 8, respectively.

Comparison of the mean-field and second-quantization results carried out for the same parameters as above but the relative phase angle between the condensates equal to $\phi = \pi/2$ yielded conclusions very similar to those summarized by Figs. 7.9 and 7.10.

Figures 7.11 and 7.12 parallel analysis of Figs. 7.9 and 7.10 for the case when the middle well is initially empty, $|\alpha|^2 = \langle N_m \rangle(0) = 0$. These figures are aimed at verifying that the rapid switching from low to high-amplification regime predicted by the theory in the mean-field limit can be also realized with only few controlling

Figure 7.10: The probability $P(N_r)$ of finding N_r atoms in the right well ($\tau = 10$). Atoms in the middle well are initially in a coherent state with $\alpha = D$. The dash-dotted line corresponds to $D^2 = 1$, the dashed line to $D^2 = 4$ and the solid line to $D^2 = 8$.

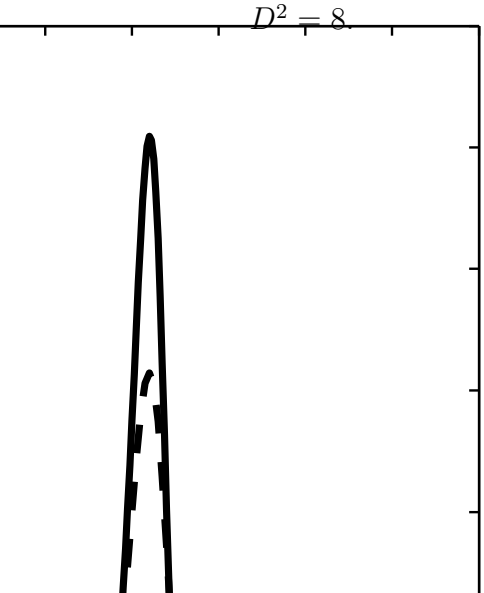

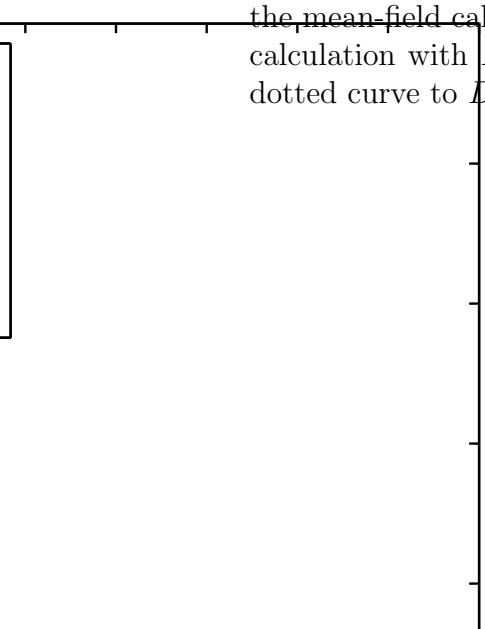

Figure 7.11: The average number of atoms in the right well as a function of the interaction time for three different values of the coupling between the left and the middle wells. The middle well is initially empty. The solid curve is the result of the mean-field calculation, the dotted curve is the result of the second-quantization calculation with $D^2 = 1$, the dashed curve corresponds to $D^2 = 4$, and the dash-dotted curve to $D^2 = 8$.

atoms.

Figure 7.11 demonstrates convergence of the second-quantization results to the mean-field limit for $\langle N_m \rangle(0) = 0$ as D^2 is increased. This convergence is similar to that shown in Fig. 7.9 except in this case the second-quantization approach gives values somewhat larger than the mean-field limit. The reason is explained by Fig. 7.12, which shows the probability $P(N_r)$ of finding N_r atoms in the right well at $\tau = 10$. The probability $P(N_r)$ has a pronounced spike at low values of N_r. Another noticeable feature of Fig. 7.12 is a wide, nearly flat pedestal extending from small values of N_r to a maximum value that is about twice larger than the average (cf. Fig. 7.11). The maximum value slightly decreases as D increases. This explains why the second-quantization results are larger than the mean-field results. The one-humped shape of $P(N_r)$ in Fig. 7.10 means that the uncertainty in the output number of atoms in the high-amplification regime is small for even a few controlling atoms in the middle well. Figures 7.11 and 7.12 show that the low-amplification region is characterized by both low average number of output atoms and by large uncertainty corresponding to the average. Indeed, the output relative standard deviation $\Delta N_r / \langle N_r \rangle$ for the results of Fig. 7.12 is equal to 1.3, 1.0 and 0.9 for $D^2 = 1, 4$ and 8, respectively. These results are in contrast to those for the large-amplification regime of Fig. 7.10, where the standard deviation rapidly goes down as the parameter D^2 increases.

7.4 Discussion

The analysis of Sec. 7.3 demonstrates that a Bose Einstein condensate in a three well potential shows transistor-like behavior with the middle well acting as a gate controlling the flux of atoms from the source to the drain. In this section we present

Figure 7.12: The probability $P(N_r)$ of finding N_r atoms in the right well ($\tau = 10$). The middle well is initially empty. The dash-dotted line corresponds to $D^2 = 1$, the dashed line to $D^2 = 4$ and the solid line to $D^2 = 8$.

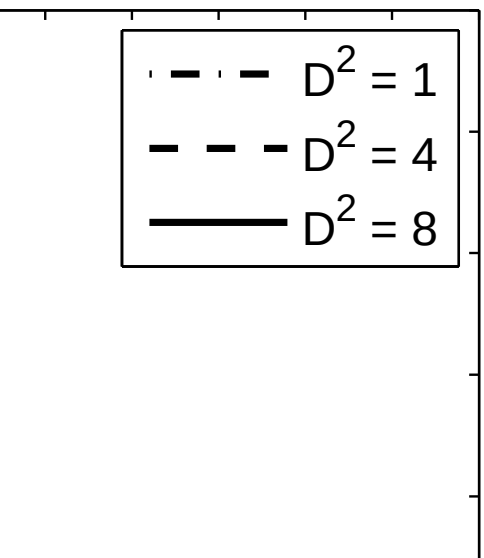

estimates of the characteristic tunneling time for a trapped atom transistor and discuss possible gain in the total number of atoms. The analysis will be extended to the case of a waveguide device, where estimates will be presented for the tunneling time, the length of the device and the gain in the output flux of atoms. Finally, we summarize the results obtained.

7.4.1 Trapped atom transistor

The parameter D in Eq. (7.29) characterizes the strength of coupling of the source (left well) to the gate (medium well). It is reasonable to expect that the operational parameters of the BEC transistor are such that the contributions of the nonlinear and linear terms in Eq. (7.29) are of the same order of magnitude, i.e. $Z_m D^2 \approx 1$.

The growth curve, shown if Fig. 7.6 shows the final population of the right well as a function of the initial population of the middle well, where the atoms are held in the traps for a dimensionless time $\tau = 20$. This figure demonstrates that a change in the population of the middle well from $N_m = 0.4D^2$ to $N_m = 0.8D^2$ results in a change in the final population of the right well from $N_r \approx 10D^2$ to $N_r \approx 60D^2$. The maximum number of atoms that tunnel into the right occurs when the number of atoms initially in the middle well is $N_m \approx D^2$. We will refer to this number as the saturation number. For example, if we take $D^2 = 10$, a change from 4 to 8 atoms in the middle well results in a change from 100 to 600 atoms in the right well.

Assume that the potential energy of the middle well is a cigar shaped potential of the form

$$V(r_\perp, z) = \frac{1}{2} m \left(\omega_\perp^2 r_\perp^2 + \omega_z^2 z^2 \right), \tag{7.34}$$

where $r_\perp$ is the coordinate in the radial direction, and z is the coordinate in the axial direction. For this potential, the overlap integral given by the Eq. (7.23) can

be evaluated as

$$\kappa_m = \frac{1}{(2\pi)^{3/2}} \frac{1}{a_\perp^2 a_z}, \tag{7.35}$$

where $a_\perp = \sqrt{\hbar/m\omega_\perp}$ and $a_z = \sqrt{\hbar/m\omega_z}$ are the harmonic oscillator lengths. The nonlinearity parameter Z_m in Eq. (7.28) is given by the expression

$$Z_m = \frac{U_0 \kappa_m}{\hbar |\Delta_{mr}|},, \tag{7.36}$$

where $U_0 = 4\pi a_s \hbar^2/m$. Using Eq. (7.35) in Eq. (7.36) allows one to express the tunneling frequency between the middle and the right wells as

$$|\Delta_{mr}| = a_s \frac{N_m}{a_z} \omega_\perp, \tag{7.37}$$

where we have also used $Z_m N_m \approx 1$ to eliminate Z_m in favor of N_m.

If the middle well is a spherical trap with $\omega_z = \omega_\perp = 2\pi \times 10^3 Hz$ and the saturation number is $D^2 = 10$ the tunneling frequency between the middle and right well is

$$\Delta_{mr} \approx \pi \times 10^2 rad/sec. \tag{7.38}$$

The dimensional time that it takes for atoms to tunnel from the left to the right wells is

$$t \approx 2 \times 10^{-1} sec. \tag{7.39}$$

In other words, for the parameters chosen a trapped atom transistor can distinguish between 4 and 8 atoms in the gate with the characteristic operational time of $10^{-1} sec$. This time can be decreased either by increasing the frequency of the trap or increasing the value of the saturation number.

7.4.2 Waveguide transistor

In a waveguide transistor the potential wells of Fig. 7.1 are the three guides that run parallel to each other for the distance L. The interaction time $T = L/v$ is determined by the speed of flow v of the BEC in the guides. The field operator for this configuration can be expressed as

$$\hat{\Psi}(\mathbf{r}, t) = \exp(ik_p z - i\omega_p t)\hat{\psi}(\mathbf{r}, t), \tag{7.40}$$

where k_p and $\omega_p = \hbar k_p^2/2m$ and the carrier wave number and frequency, respectively, and $\hat{\psi}$ is the field-operator envelope.

The Heisenberg equations of motion for the field operator $\hat{\psi}$ in the co-propagating frame $t' = t$, $z' = z - vt$ is of the form

$$i\hbar\frac{\partial}{\partial t}\hat{\psi} = \left[-\frac{\hbar^2}{2m}\left(\nabla_\perp^2 + \frac{\partial^2}{\partial z^2}\right) + V(\mathbf{r}_\perp) + U_0\hat{\psi}^\dagger\hat{\psi}\right]\hat{\psi}, \tag{7.41}$$

where $v = \hbar k_p/m$ is the velocity of the condensate and the primes have been omitted.

Changes in density as the condensate propagates through the transistor occur at a length scale L_{BEC}. We assume that the kinetic energy associated with the longitudinal direction is small in comparison with the characteristic energy $\hbar\Omega$ associated with the transverse eigenmodes of the transistor

$$\hbar\Omega \gg \frac{\hbar^2}{2mL_{BEC}^2}. \tag{7.42}$$

Next, we require that L_{BEC} does not change appreciably during the time interval L/v that it takes the condensate to propagate through the transistor,

$$\left|\frac{\partial}{\partial t}\ln L_{BEC}\right| \ll \frac{v}{L} \tag{7.43}$$

With Eqs. (7.42) and (7.43) fulfilled, the dispersive term $(\partial^2/\partial z^2)$ in Eq. (7.41) can be neglected and the coordinate z becomes a parameter. Propagation of different "slices" of the condensate (parametrized by the coordinate z) through the transistor can be analyzed independently.

Represent the field operator $\hat{\psi}$ as

$$\hat{\psi} = \sum_i \phi_i(\mathbf{r}_\perp) b_i(z,t), \tag{7.44}$$

where $\phi(\mathbf{r}_\perp)$ is the i-th transverse local mode and $b_i(z,t)$ is the destruction operator that destroys an atom in the i-th local mode at the coordinate z. Note that b_i now has dimension of $m^{-1/2}$.

Using Eq. (7.44) in Eq. (7.41) with the dispersive term dropped, results in the equations of motion in the Heisenberg picture for the operators b_i that are of the same form as Eq. (7.24):

$$i\hbar \frac{d}{dt} b_i(z,t) = \sum_{i,j} \hbar\Omega_k u_{ki} u^*_{kj} b_j + U_0 \kappa_i b_i^\dagger b_i, \tag{7.45}$$

As in the case of a trapped device, the left guide will be treated as a reservoir of atoms corresponding to the replacement $b_l \to \sqrt{n_l}$, where n_l is the density of atoms (number of atoms per unit length). The equations of motion for the atoms in the middle and right guide, in dimensionless form, become

$$\begin{aligned} i\frac{d}{d\tau} b_m(z,t) &= (\omega_m + Z_m b_m^\dagger b_m) b_m - D - b_r \\ i\frac{d}{d\tau} b_r(z,t) &= (\omega_r + Z_r b_r^\dagger b_r) b_r - b_m, \end{aligned} \tag{7.46}$$

where the dimensionless parameters are $Z_i = -U_0\kappa_i/\hbar L\Delta_{mr}$, $\omega_i = (\mu - \Lambda_i)/\Delta_{mr}$, $D = \Delta_{lm}\sqrt{Ln_l}/\Delta_{mr}$, and L is the length of the transistor. The destruction opera-

tors are normalized to $b_i' = b_i/\sqrt{L}$, and the primes have been dropped. Since the equations for each "slice" in z are of the same form as Eq. (7.29), the analysis of Sec. 7.3 is valid for each "slice" separately.

As with the case of a trapped atom transistor, we take $Z_m D^2 = 1$ and use the fact that the largest tunneling rate corresponds to $n_m \approx D^2$. We refer to this as the saturation density, since n_m is the normalized density of atoms and not the total number as it was with a trapped atom device. Next, we assume that the middle waveguide can be described by the potential

$$V(\mathbf{r}_\perp) = \frac{1}{2} m\omega_\perp^2 r_\perp^2, \tag{7.47}$$

where $\omega_\perp$ is the transverse frequency of the guide. The overlap integral associated with this potential is

$$\kappa_m = \frac{1}{2\pi}\frac{1}{a_\perp^2}, \tag{7.48}$$

where $a_\perp$ is the transverse oscillator length and $a_\perp = \sqrt{\hbar/m\omega_\perp}$. Using Eq. (7.36) and (7.48), we evaluate the coupling frequency between the middle and right guides as

$$|\Delta_{mr}| \approx a_s \omega_\perp \frac{n_m}{L}. \tag{7.49}$$

In terms of the velocity of the atoms v and the flux entering the middle guide Φ_m the density can be expressed as $n_m/L = \Phi_m/v$, and Eq. (7.49) takes the form

$$|\Delta_{mr}| \approx a_s \omega_\perp \frac{\Phi_m}{v}. \tag{7.50}$$

Assuming that the guide has a transverse frequency of 10 kHz, the velocity 5 cm/sec and the saturation flux is 10^5 atoms/sec, we can evaluate the coupling frequency

between the right and middle guide as

$$\Delta_{mr} \approx 2\pi \times 10^2 rad/sec. \tag{7.51}$$

The dimensional switching time is

$$t \approx 2 \times 10^{-1} sec, \tag{7.52}$$

and the length of the device is

$$L \approx 1cm. \tag{7.53}$$

This length can be decreased by slowing the velocity of the atoms, increasing the saturation flux or increasing the transverse frequency of the waveguide.

With the above numbers, a change in the input flux of the middle guide from 0.4×10^5 atoms/sec to 0.8×10^5 atoms/sec results in a change of flux in the output of the right guide from 10^6 atoms/sec to about 10^7 atoms/sec.

To summarize, we have presented a theoretical analysis of a Bose Einstein condensate in a nonsymmetric three-well potential which shows transistor-like behavior. We demonstrated the control of atomic population in the right well by the population in the middle well with an absolute and differential gains considerably larger than one. The second-quantization formalism was then used to evaluate the quantum-mechanical uncertainty due to a finite number of atoms and extend the mean-field results to the limit of a small number of atoms.

The BEC transistor can turn out to be useful in precision measurements. The number of atoms that tunnel from the source to the drain is very sensitive to the number of atoms in the gate. This fact can be used to detect and amplify small changes in the number of atoms in the gate. A waveguide based transistor is capable

of operating continuously and can be used to measure time-dependent phenomena. Applications of this device may include measurement of inertial changes and electromagnetic fields. It is possible to envision potentially more interesting applications by combining several such devices so that, e.g., the amplified output of the first transistor serves as control for the second.

Appendix A

Dynamics of the BEC due to the optical pulses

The optical potential is used to split the initial zero-momentum BEC cloud at the beginning of the interferometric cycle into the two harmonics with the momenta ± 1, reverse their direction of propagation in the middle of the cycle and recombine them at the end. The optical pulses are short and sufficiently intense so that the dynamics of the condensate is dominated by the optical potential when the laser beams are on and the diffraction, relative displacements of the clouds and the nonlinearity can be neglected. A good quantitative description of the BEC dynamics can be obtained keeping only the lowest three harmonics with $n = 0, \pm 1$ in Eq. (5.7). The set of Eq. (5.8) with these approximations reduces to

$$i\frac{d}{d\tau}\begin{bmatrix}\psi_{-1}\\ \psi_0\\ \psi_1\end{bmatrix} = \frac{1}{2}\begin{bmatrix}1 & \Omega & 0\\ \Omega & 0 & \Omega\\ 0 & \Omega & 1\end{bmatrix}\begin{bmatrix}\psi_{-1}\\ \psi_0\\ \psi_1\end{bmatrix}. \tag{A.1}$$

Solution of Eq. (A.1) has the form

$$\begin{bmatrix} \psi_{-1}(\tau) \\ \psi_0(\tau) \\ \psi_1(\tau) \end{bmatrix} = \begin{bmatrix} A_{11} & A_{12} & A_{13} \\ A_{12} & A_{22} & A_{12} \\ A_{13} & A_{12} & A_{11} \end{bmatrix} \begin{bmatrix} \psi_{-1}(0) \\ \psi_0(0) \\ \psi_1(0) \end{bmatrix} \tag{A.2}$$

where

$$A_{11} = \frac{1}{2}\left[\cos\frac{s\tau}{4} + e^{-i\tau/4} - \frac{i}{s}\sin\frac{s\tau}{4}\right], \tag{A.3}$$

$$A_{12} = -2i\frac{\Omega}{s}\sin\frac{s\tau}{4}, \tag{A.4}$$

$$A_{13} = \frac{1}{2}\left[\cos\frac{s\tau}{4} - e^{-i\tau/4} - \frac{i}{s}\sin\frac{s\tau}{4}\right], \tag{A.5}$$

$$A_{22} = \cos\frac{s\tau}{4} + \frac{i}{s}\sin\frac{s\tau}{4}, \tag{A.6}$$

and $s = \sqrt{1+8\Omega^2}$. Using Eq. (A.2) it is straightforward to show that the momentum reversal of the moving BEC clouds $\psi_{\pm1} \rightarrow \psi_{\mp1}$ can be achieved with a single pulse of duration $\tau_p = 4\pi$ and magnitude $\Omega_p = (3/8)^{1/2}$. The unitary evolution matrix corresponding to the momentum reversal pulse is of the form

$$U_{\pm1\leftrightarrow\mp1} = \begin{bmatrix} 0 & 0 & 1 \\ 0 & 1 & 0 \\ 1 & 0 & 0 \end{bmatrix}. \tag{A.7}$$

Splitting of the zero-momentum cloud ψ_0 into the two harmonics $\psi_{\pm1}$ and the recombination (the inverse of the splitting) requires a double pulse sequence. The first pulse with $\Omega_p = (1/8)^{1/2}$ and $\tau_p = 2^{1/2}\pi$ is followed by a period of free evolution when the lasers are turned off for a time interval $\tau_{ev} = 2\pi$ and then followed by the second optical pulse with $\Omega_p = (1/8)^{1/2}$ and $\tau_p = 2^{1/2}\pi$. The evolution matrix for

the splitting sequence is given by

$$U_{0\leftrightarrow\pm1} = \begin{bmatrix} -\frac{1}{2}\exp(-i\pi/\sqrt{2}) & \frac{1}{\sqrt{2}} & \frac{1}{2}\exp(-i\pi/\sqrt{2}) \\ \frac{1}{\sqrt{2}} & 0 & \frac{1}{\sqrt{2}} \\ \frac{1}{2}\exp(-i\pi/\sqrt{2}) & \frac{1}{\sqrt{2}} & -\frac{1}{2}\exp(-i\pi/\sqrt{2}) \end{bmatrix}, \tag{A.8}$$

(irrelevant common phase has been omitted).

Direct numerical solution of Eq. (5.6) shows that optical pulses result in some amount of energy transfer into higher harmonics, primarily $\psi_{\pm2}$. For example, a momentum reversal pulse with the parameters given above leaves several percent of energy in the second harmonics. Due to non-ideal operation of the optical pulses, about ten percent of the atomic population can be in undesirable modes at the end of the interferometric pulse. A simple numerical optimization of the optical pulses' amplitudes and durations can decrease population of the the unwanted harmonics. Our analysis shows that the energy transfer into undesirable harmonics is of no critical importance to the operation of the interferometer and thus the optimization will not be discussed here.

Bibliography

[1] E.A. Cornell and C.E. Wieman. Nobel lecture: Bose-Einstein condensation in dilute gas, the first 70 years and some recent experiments. *Rev. Mod. Phys.*, 74:875, 2002.

[2] W. Ketterle. Nobel lecture: When atoms behave as waves: Bose-Einstein condensation and the atom laser. *Rev. Mod. Phys.*, 74:1131, 2002.

[3] J.F. Clauser. Ultra-high sensitivity accelerometers and gyroscopes using neutral atom matter-wave interferometry. *Physica B & C*, 151:262, 1988.

[4] M.O. Scully and J.P. Dowling. Quantum-noise limits to matter-wave interferometry. *Phys. Rev. A*, 48:3186, 1993.

[5] Paul R. Berman, editor. *Atom interferometry.* Academic Press, 1997.

[6] K. Krane. *Modern Physics.* John Wiley & Sons, Inc., New York, 1996.

[7] N. F. Ramsey. Experiments with separated oscillatory fields and hydrogen masers. *Rev. Mod. Phys.*, 62:541, 1990.

[8] F. Riehle, Th. Kisters, A. Witte, and J. Helmcke. Optical ramsey spectroscopy in a rotating frame: Sagnac effect in a matter-wave interferometer. *Phys. Rev. Lett.*, 67:177, 1991.

[9] D.W. Keith, C.R. Ekstrom, Q.A. Trchette, and D.E. Pritchard. An interferometer for atoms. *Phys. Rev. Lett.*, 66:2693, 1991.

[10] S. Gupta, K. Dieckmann, Z. Hadzibabic, and D.E. Pritchard. Contrast interferometry using Bose-Einstein condensates to measure h/m and . *Phys. Rev. Lett.*, 89:140401, 2002.

[11] C. R. Exkstrom, J. Schmiedmayer, M. S. Chapman, T. D. Hammond, and D. E. Pritchard. Measurement of the electric polarizability of sodium with an atom interferometer. *Phys. Rev. A.*, 51:3883, 1995.

[12] A. Miffre, M. Jacquey, M. Buchner, G. Trenec, and J. Vigue. Measurement of the electric polarizability of lithium by atom interferometry. *Phys. Rev. A.*, 73:011603(R), 2006.

[13] M. Kasevich and S. Chu. Atomic interferometry using stimulated raman transitions. *Phys. Rev. Lett.*, 67:181, 1991.

[14] T. L. Gustavson, P. Bouyer, and M. Kasevich. Precision rotation measurements with an atom interferometer gyroscope. *Phys. Rev. Lett.*, 78:2046, 1997.

[15] M.J. Snadden, J.M. McGuirk, P. Bouyer, K.G. Haritos, and M. Kasevich. Measurement of the earth's gravity gradient with an atom interferometer-based gravity gradiometer. *Phys. Rev. Lett.*, 81:971, 1998.

[16] J.M. McGuirk, M.J. Snadden, and M. Kasevich. Large area light-pulse atom interferometry. *Phys. Rev. Lett.*, 85:4498, 2000.

[17] A. Pais. Einstein and the quantum theory. *Rev. Mod. Phys.*, 51:863, 1979.

[18] C. J. Pethick and H. Smith. *Bose-Einstein Condensation in Dilute Gases.* Cambridge Univeristy Press., 2002.

[19] A. Ashkin. Acceleration and trapping of particles by radiation pressure. *Phys. Rev. Lett.*, 24:156, 1970.

[20] J. Dalibard and C. Cohen-Tannoudji. Laser cooling below the Doppler limit by polarization gradients: simple theoretical models. *J. Opt. Soc. Am. B.*, 6:2023, 1989.

[21] C.J. Foot. *Atomic Physics*. Oxford Univ. Press, 2005.

[22] J. Fortagh and C. Zimmermann. Magnetic microtraps for ultracold atoms. *Rev. Mod. Phys.*, 79:235, 2007.

[23] J. Reichel. Microchip traps and Bose-Einstein condensation. *Appl. Phys. B.*, 75:469, 2002.

[24] M. Horikoshi and K. Nakagawa. Atom chip based fast production of Bose-Einstein condensate. *Appl. Phys. B.*, 82:363, 2005.

[25] W. Hansel, P. Hommelhoff, T.W. Hansch, and J. Reichel. Bose-Einstein condensation on a microelectronic chip. *Nature*, 413:498, 2001.

[26] L.M. Andersson L. Feenstra and J. Schmiedmayer. Microtraps and atom chips: Toolboxes for cold atom physics. *General Relativity and Gravitation*, 36:2317, 2004.

[27] E.A. Hinds, C.J. Vale, and M.G. Boshier. Two-wire waveguide and interferometer for cold atoms. *Phys. Rev. Lett.*, 86(8):1462, February 2001.

[28] W. Hansel, P. Hommelhoff W. Hänsel, T. Steinmetz, T.W. Hansch, and J. Reichel. Transporting, splitting and merging of atomic ensembles in a chip trap. *New Journal of Physics*, 7:3, 2005.

[29] M. B. Crookston, P. M. Baker, and M. P. Robinson. A microchip ring trap for cold atoms. *J. Phys. B: At. Mol. Opt. Phys*, 39:3289, 2005.

[30] Chris P. Search and Pierre Meystre. Noise limits in matter-wave interferometry using degenerate quantum gases. *Phys. Rev. A*, 67(6):061601, 2003.

[31] T. Schumm, S. Hofferberth, L.M. Andersson, S. Wildmermuth, S. Groth, I. Bar-Joseph, J. Schmiedmayer, and P. Kruger. Matter-wave interferometry in a double well on a atom chip. *Nature Physics*, 1:57, 2005.

[32] G.-B. Jo, Y. Shin, S. Will, T.A. Pasquini, M. Saba, W. Ketterle, D.E. Pritchard, M. Vengalattore, and M. Prentiss. Long phase coherence time and number squeesing of two Bose-Einstein condensates on an atom chip. *Phys. Rev. Lett.*, 98:030407, 2007.

[33] Y.J. Wang, D.Z. Anderson, V.M. Bright, E.A. Cornell, Q. Diot, T. Kishimoto, M. Prentiss, R.A. Saravanan, S.R. Segal, and Saijun Wu. Atom michelson interferometer on a chip using a Bose-Einstein condensate. *Phys. Rev. Lett.*, 94:090405, 2005.

[34] O. Garcia, B. Deissler, K. J. Hughes, J. M. Reeves, and C. A. Sackett. Bose-Einstein-condensate interferometer with macroscopic arm separation. *Phys. Rev. A*, 74:031601, 2006.

[35] Munekazu Horikoshi and Ken'ichi Nakagawa. Dephasing due to atom-atom interaction in a waveguide interferometer usingin a Bose-Einstein condensate. *Phys. Rev. A.*, page 031602, 2006.

[36] Y. Shin, M. Saba, T.A. Pasquini, W. Ketterle, D.E. Pritchard, and A.E. Leanhardt. Atom interferometery with Bose-Einstein condenates in a double-well potential. *Phys. Rev. Lett.*, 92:050405, 2004.

[37] J.A. Stickney and A. A. Zozulya. Expansion of a Bose-Einstein condensate from a microtrap into a waveguide. *Phys. Rev. A.*, 65:053612, 2002.

[38] Y. Shin, C. Sanner, G.-B. Jo, T. A. Pasquini, M. Saba, W. Ketterle, D. E. Pritchard, M. Vengalattore, and M. Prentiss. Interference of Bose-Einstein condensates split with an atom chip. *Phys. Rev. A*, 72:021604, 2005.

[39] I. Lesanovsky, S. Hofferberth, J. Schmiedmayer, and P. Schmelcher. Manipulation of ultracold atoms in dressed adiabatic radio frequency potentials. *arXiv:physics/0606165*, 2006.

[40] G.-B. Jo, J.-H. Choi, C. A. Christensen, T. A. Pasquini, Y.-R. Lee, W. Ketterle, and D. E. Pritchard. Phase-sensitive recombination of two Bose-Einstein condensates on an atom chip. *Phys. Rev Letts.*, 98(18):180401, 2007.

[41] James A. Stickney and Alex A. Zozulya. Influence of nonadiabaticity and nonlinearity on the operation of cold-atom beam splitters. *Phys. Rev. A*, 68(1):013611, 2003.

[42] James A. Stickney and Alex A. Zozulya. Wave-function recombination instability in cold-atom interferometers. *Phys. Rev. A*, 66(5):053601, 2002.

[43] S. Wu, Y.J. Wang, Q. Diot, and M. Prentiss. Splitting matter waves using an optimized standing wave light-pulse sequence. *Phys. Rev. A.*, 71:043602, 2005.

[44] Maxim Olshanii and Vanja Dunjko. Interferometry in dense nonlinear media and interaction-induced loss of contrast in microfabricated atom interferometers, 2005.

[45] D. Muller, D.Z. Anderson, R.J. Grow, P.D.D. Schwindt, and E.A. Cornell. Guiding neutral atoms around curves with lithographically patterned current-carrying wires. *Phys. Rev. Lett.*, 83:5194, 1999.

[46] N.H. Dekker, C.S. Lee, V. Lorent, J.H. Thywissen, S.P. Smith, M. Drndic, R.M. Westervelt, and M. Prentiss. Guiding neutral atoms on a chip. *Phys. Rev. Lett.*, 84:1124, 2000.

[47] D. Cassettari, B. Hessmo, R. Folman, T. Maier, and J. Schmiedmayer. Beam splitter for guided atoms. *Phys. Rev. Lett.*, 85:5483, 2000.

[48] A. E. Leanhardt, A. P. Chikkatur, D. Kielpinski, Y. Shin, T. L. Gustavson, W. Ketterle, and D. E. Pritchard. Propagation of Bose-Einstein condensates in a magnetic waveguide. *Phys. Rev. Lett.*, 89(4):040401, 2002.

[49] B. T. Seaman, M. Kraemer, D. Z. Anderson, and M. J. Holland. Atomtronics: ultracold atom analogs of electronic devices. *Phys. Rev. A.*, 75:023615, 2007.

[50] A. Ruschhaupt and J.G. Muga. Three-dimensional effects in atom diodes: Atom-optical devices for one-way motion. *Phys. Rev. A.*, 76:013619, 2007.

[51] A. Micheli, A. J. Daley, D. Jaksch, and P. Zoller. Single atom transistor in a 1d optical lattice. *Phys. Rev. Lett.*, 93:140408, 2004.

[52] J.A. Stickney and A. A. Zozulya. Transistorlike behavior of a Bose-Einstein condensate in a triple-well potential. *Phys. Rev. A.*, 75:013608, 2007.

[53] Franco Dalfovo, Stefano Giorgini, Lev P. Pitaevskii, and Sandro Stringari. Theory of Bose-Einstein condensation in trapped gases. *Rev. Mod. Phys.*, 71(3):463–512, Apr 1999.

[54] P. Leboeuf and N. Pavloff. Bose-Einstein beams: Coherent propagation through a guide. *Phys. Rev. A*, 64:033602, 2001.

[55] E. Andersson, T. Calarco, R. Folman, M. Andersson, B. Hessmo, and J. Schmiedmayer. Multimode interferometer for guided matter waves. *Phys. Rev. Lett.*, 88:100401, 2002.

[56] W. Hansel, J. Reichel, P. Hommelhoff, and T. W. Hansch. Trapped-atom interferometer in a magnetic microtrap. *Phys. Rev. A*, 64:063607–1, 2001.

[57] L. D. Landau. *Phys. Z. Sowjetunion*, 2:46, 1932.

[58] C. Zener. *Proc. R. Soc. London Ser.*, A137:696, 1932.

[59] L. D. Landau and E. M. Lifshitz. *Quantum mechanics: Non-relativistic theory.* Pergamon Press, 1977.

[60] I. S. Gradshteyn and I. M. Ryzhik. *Table of Integrals, Series and Products.* Academic Press, 1965.

[61] G. J. Milburn, J. Corney, E. M. Wright, and D. F. Walls. Quantum dynamics of an atomic Bose-Einstein condensate in a double-well potential. *Phys. Rev. A*, 55(6):4318–4324, 1997.

[62] M. Jaaskelainen and P. Meystre. Coherence dynamics of two-mode condensate in asymmetric potentials. *Phys. Rev. A.*, 73:013602, 2006.

[63] Stephen M Jensen. *IEEE J. Quantum Electron*, 18:1580, 1982.

[64] S. Raghavan, A. Smerzi, S. Fantoni, and S. R. Shenoy. Coherent oscillations between two weakly coupled Bose-Einstein condensates: Josephson effects, π oscillations, and macroscopic quantum self-trapping. *Phys. Rev. A*, 59(1):620–633, Jan 1999.

[65] S. Wu, E.J.Su, and M. Prentiss. Time domain de Broglie wave interferometry along a magnetic guide. *Eur. Phys. J. D*, 35:111–118, 2005.

[66] Y. Castin and R. Dum. Bose-Einstein condensates in time dependent traps. *Phys. Rev. Lett.*, 77:5315, 1996.

[67] F. Dalfovo, C. Minniti, S. Stringari, and L. Pitaveskii. Nonlinear dynamics of a Bose condensed gas. *Phys. Letts. A.*, 227:259, 1997.

[68] Y. Kagan, E.L. Surkov, and G.V. Shlyapnikov. Evoloution of a Bose gas in anisotropic time-dependent traps. *Phys. Rev. A.*, 55:R18, 1997.

[69] J. H. T. Burke, B. Deissler, K. J. Hughes, and C. A. Sackett. Confinement effects in a guided-wave interferometer with millimeter-scale separation. *arXiv:0705.1081v1*, 2007.

[70] B. Deissler, K. J. Hughes, J. H. T. Burke, and C. A. Sackett. Measurement of the ac Stack shift with a guided matter-wave interferometer. *arXiv:0709.4675v1*, 2007.

[71] M. Lewenstein and L. You. Quantum phase diffusion of a bose-einstein condensate. *Phys. Rev. Lett.*, 77:3489, 1996.

[72] J. Javanainen and M. Wilkens. Phase and phase diffusion of a split Bose-Einstein condensate. *Phys. Rev. Lett.*, 78:4675, 1997.

[73] A.J. Leggett and F. Sols. Comment on "phase and phase diffusion of a split Bose-Einstein condensate". *Phys. Rev. Lett.*, 81:1344, 1998.

[74] J. Javanainen and M. Wilkens. Javanainen and wilkens reply:. *Phys. Rev. Lett.*, 81:1345, 1998.

[75] D.S. Petrov, G.V. Shlyapnikov, and J.T.M. Walraven. Phase-fluctuating 3d Bose-Einstein condensates in elongated traps. *Phys. Rev. Lett.*, 87:050404, 2001.

[76] S. Dettmer, D. Hellweg, J.J. Arlt, W. Ertmer, K. Sengstock, D.S. Petrov, G.V. Shlyapnikov, H. Kreutzmann, L. Santos, and M. Lewenstein. Observation of phase fluctuations in elongated Bose-Einstein condensates. *Phys. Rev. Lett.*, 87:160406, 2001.

[77] A. A. Burkov, M.D. Lukin, and E. Demler. Decoherence dynamics in low-dimensional cold atom interferometers. *Phys. Rev. Lett.*, 98:200404, 2007.

[78] S. Hofferberth, I. Lesanovsky, B. Fischer, T. Schumm, and J. Schmiedmayer. Non-equilibrium coherence dynamics in one-dimensional bose gas. *arXiv.org:cond-mat/0706.2259v1*, 2007.

[79] A. Smerzi, S. Fantoni, S. Giovanazzi, and S. R. Shenoy. Quantum coherent atomic tunneling between two trapped Bose-Einstein condensates. *Phys. Rev. Lett.*, 79(25):4950–4953, 1997.

[80] Roberto Franzosi and Vittorio Penna. Self-trapping mechanisms in the dynamics of three coupled Bose-Einstein condensates. *Phys. Rev. A*, 65(1):013601, 2001.

[81] Th. Anker, M. Albiez, R. Gati, S. Hunsmann, B. Eiermann, A. Trombettioni, and M.K. Oberthaler. Nonlinear self-trapping of matter waves in periodic potentials. *Phys. Rev. Lett.*, 94:020403, 2005.

[82] M. J. Steel and M. J. Collett. Quantum state of two trapped Bose-Einstein condensates with a josephson coupling. *Phys. Rev. A*, 57(4):2920–2930, 1998.

[83] R. W. Spekkens and J. E. Sipe. Spatial fragmentation of a Bose-Einstein condensate in a double-well potential. *Phys. Rev. A*, 59(5):3868, 1999.

[84] Juha Javanainen and Misha Yu. Ivanov. Splitting a trap containing a Bose-Einstein condensate: Atom number fluctuations. *Phys. Rev. A*, 60(3):2351–2359, 1999.

[85] M. Jaaskelainen, W. Zhang, and P. Meystre. Limits to phase resolution in matter-wave interferometry. *Phys. Rev. A*, 70(6):063612, 2004.

[86] M. Jaaskelainen and P. Meystre. Dynamics of Bose-Einstein condensates in double-well potentials. *Phys. Rev. A*, 71(4):043603, 2005.

[87] K. Nemoto, C.A. Holmes, G.J. Milburn, and W.J. Munro. Quantum dynamics of three coupled atomic Bose-Einstein condensates. *Phys. Rev. A*, 63:013604, 2000.

[88] Roberto Franzosi and Vittorio Penna. Chaotic behavior, collective modes, and self-trapping in the dynamics of three coupled Bose-Einstein condensates. *Phys. Rev. E*, 67(4):046227, 2003.